Multi-dimensional quantum dynamics of light molecules on surfaces

Arezoo Dianat

Technische Universität München
Physik-Department T30
Univ.-Prof. Dr. A. Groß

Multi-dimensional quantum dynamics of light molecules on surfaces

Arezoo Dianat

Vollständiger Abdruck der von der Fakultät für Physik der Technischen Universität München zur Erlangung des akademischen Grades eines

Doktors der Naturwissenschaften (Dr. rer. nat.)

genehmigten Dissertation.

Vorsitzende:	Univ.-Prof. Dr. Katharina Krischer
Prüfer der Dissertation:	1. Univ.-Prof. Dr. Axel Groß
	2. Univ.-Prof. Dr. Wilhelm Brenig, em.

Die Dissertation wurde am 9. August 2004 bei der Technischen Universität München eingereicht und durch die Fakultät für Physik am 11. Oktober 2004 angenommen.

Abstract

Multi-dimensional quantum dynamics of light molecules on surfaces have been studied within the coupled-channel scheme using the concept of local reflection (LORE) and inverse transmission (INTRA) coefficients. The potential energy surfaces (PES) of the molecule-surface interaction are derived from *ab initio* total-energy calculations.

In this work, the dynamics of three different molecule-surface systems have been investigated: The competition between the rotational hindering and an opposite effect due to the extension of the molecular bond length causes a non-monotonous behavior of the rotational alignment and the sticking probability, which are investigated for the H_2/D_2 interaction with the Pd(100) surface. The open structure of Pd(110) leads to a strongly corrugated and anisotropic PES for H_2/Pd(110). This has significant consequences for the interaction dynamics as a function of the angle of incidence and the rotational state. As one of the consequences, rotational heating has been found in desorption which has not been observed before in H_2 desorption from metal surfaces. In addition, we obtain high intensities in the off-specular and rotationally inelastic diffraction peaks. Furthermore, the dissociative adsorption of H_2 on Rh(111) surface has been investigated. The bump in the sticking probability versus kinetic energy at high incident beam energies which is observed by experiment is reproduced by our calculations.

Zusammenfassung

Die multidimensionale Quantendynamik leichter Moleküle wurde auf verschiedenen Metalloberflächen mit Hilfe einer *Coupled-Channel* Methode untersucht. Für das System H_2/D_2 auf Pd(100) ergibt sich, daß die Änderung der Bindungslänge der Moleküle zu einem nicht-monotonen Verhalten der j-Abhängigkeit der Haftwahrscheinlichkeit führt. Auf der stark strukturierten Pd(110) Oberfläche haben wir den Einfluß der Anfangszustände des Wasserstoffmoleküls auf die Dissoziation bestimmt. In diesem System fanden wir eine ungewöhnliche Erhöhung der Rotationsenergie für desorbierende Moleküle. Darüber hinaus erhält man hohe Streuwahrscheinlichkeiten für rotations-unelastisch gestreute Moleküle. Weiterhin berechneten wir die Adsorptionwahrscheinlichkeit von H_2 auf Rh(111) , um den im Experiment beobachteten Verlauf der Haftwahrscheinlichkeit bei hohen Energien des Moleküls zu erklären.

Acknowledgments

The first and foremost person I would like to thank is my supervisor Prof. Dr. Axel Groß. I owe him lots of gratitude for having shown the interesting research subject.

I would also like to thank my colleagues and members of the T30g group, Markus Lischka, Christian Bach, Christian Mosch, Ata Roudgar, Sung Sakong, Thomas Markert, Christian Sendler, Christian Carbogno and Prof. Dr. Willhelm Brenig for many interesting discussions and answering lots of my questions, not only about physics.

I would also like to acknowledge financial support by the Wilhelm und Else Heraus-Stiftung for attending the DFG-Frühjahrstagungen 2003/2004.

I would especially like to thank my parents and my brothers for constant support during my life.

München Arezoo Dianat
August 2004

Contents

Abstract **iii**

Zusammenfassung **v**

Acknowledgments **vii**

1 Introduction **1**

2 Theory **3**
- 2.1 Electronic states and potential energy surface 3
- 2.2 Functional form of PESs 5
  - 2.2.1 Interpolations of PES based on *ab initio* calculations 6
  - 2.2.2 PES adapted to the surface symmetry 7
  - 2.2.3 Analysis of surface topology 10
- 2.3 Dynamics of molecule-surface interaction 12
  - 2.3.1 Coupled-channel equation and symmetry of the surface 14
  - 2.3.2 INTRA-LORE method 16
  - 2.3.3 The structure of computational simulation 21

3 Rotational effects in adsorption of H_2/D_2 on Pd(100) **23**
- 3.1 Introduction 23
- 3.2 Three-dimensional anisotropic potential 25
  - 3.2.1 Rotational effects of H_2 and D_2 on an anisotropic surface 28
  - 3.2.2 Rotational effect with frozen bond length 34
- 3.3 Five-dimensional corrugated potential 36
  - 3.3.1 Rotational effect of H_2 and D_2 on corrugated surface 37

4 Six-dimensional quantum dynamics of H_2 on Pd(110) **41**
- 4.1 Dissociative adsorption of H_2 on Pd(110) 41
  - 4.1.1 Introduction 41
  - 4.1.2 Experimental situation 43
  - 4.1.3 Parameterization of *ab initio* results and QMD 44

4.1.4 Rotational effect on the reaction probabilities 48
4.1.5 Parallel momentum effects 52
4.2 Scattering of H_2 from Pd(110) 56
4.2.1 Introduction 56
4.2.2 Calculational details 57
4.2.3 Angular distribution of scattering intensity 58
4.2.4 Energy dependence of the scattering intensity 60

5 Dissociative adsorption of H_2 on Rh(111) 65
5.1 Introduction 65
5.2 Experimental situation 66
5.3 Parameterization of *ab initio* potentials and QMD calculation 67
5.4 Rotational effects on the azimuthally flat potential 70

6 Conclusions 75

Bibliography 77

List of Publications 83

List of Figures

2.1 The degrees of freedom of diatomic molecule 6
2.2 Illustration of the reaction path in Zr plane 8
2.3 Schematic form of elbow plot 11
2.4 Energetic and geometric corrugation 12
2.5 The symmetry of rectangular, square and hexagonal lattice 14
2.6 Flow-chart of coupled-channel computational simulation 22

3.1 The elbow plot for bridge site of H_2 dissociation on Pd(100) 26
3.2 The reaction path coefficients used in the anisotropic surface 28
3.3 3D calculation of the sticking probability for $m = 0$ and $m = j$. 30
3.4 3D calculation of the sticking probability averaged over m. 31
3.5 Rotational alignment of H_2 and D_2 by 3D calculation 32
3.6 3D calculation of sticking probability with the fixed bond length 33
3.7 between two fixed bond lengths 34
3.8 Rotational alignment with the fixed bond length 35
3.9 5D calculation of sticking probability for different j 37
3.10 Rotational alignment of H_2 and D_2 derived by 5D calculation 38
3.11 Rotational alignment of D_2 derived by 3D and 5D calculations 39

4.1 The experimental result of H_2/Pd(110) 43
4.2 The reaction paths used in *ab initio* calculations 45
4.3 Potential energy surface of H_2 on Pd(110) 47
4.4 effects on sticking probability 48
4.5 Sticking probability for different azimuthal quantum numbers 50
4.6 Rotational heating 51
4.7 Rotational alignment for H_2/Pd(110) 52
4.8 Normal component scaling of sticking probability 53
4.9 Sticking probability along $< 1\bar{1}0 >$ and $< 001 >$ directions 54
4.10 Sticking as a function of incidence angle 56
4.11 Angular distribution of scattering intensity 59
4.12 Scattering intensity for cartwheel and helicopter rotation 60
4.13 Scattering probability versus kinetic energy for normal incidence 61

4.14 Scattering probability versus kinetic energy for off-normal incidence. . . 62

5.1 Experimental result of sticking coefficient for H_2 and D_2/Rh(111) . . . 66
5.2 The reaction paths used in *ab initio* calculation for H_2/Rh(111) 67
5.3 Elbow plots of H_2/Rh(111) 69
5.4 Sticking probability of the rotating molecules 71
5.5 Sticking probability in various azimuthal quantum numbers 73
5.6 Rotational temperature as a function of surface temperature 74
5.7 Rotational alignment for H_2/Rh(111) 74

List of Tables

2.1 The symmetry group of the square lattice 16

3.1 Parameters used in 3-5 dimensional potential of Pd(100) 29

4.1 The comparison between *ab initio* total energies and potentials 46

5.1 Energies and geometries of the barriers for H_2/Rh(111) 68

Chapter 1

Introduction

How and why do molecules break up on surfaces? Answering this question requires the application of two distinct branches of theory; we need to follow the motion of a molecule (i.e. solve the dynamics), and in order to do that we must compute the energy it has at each position. One of the early studies was made by Lennard-Jones, who proposed a model for understanding the energetics of molecular dissociation at a metal surface [1]. The Lennard-Jones model described an one-dimensional potential energy surface. However, if more than one coordinate is necessary to specify a configuration the model would not be sufficient. The next significant development in our understanding of molecular dissociation at metals came with the appearance of the first classical molecular dynamics (MD) simulations. Experimental studies of the reverse process, associative desorption, had begun with the work of Van Willigen in which the data have been interpreted within an one dimensional potential model. More realistic MD descriptions of the molecule-surface interaction were possible with potential energy surfaces (PES) using LEPS methods (see section 2.2). With LEPS potentials the dependence of the dissociation probability on translational and internal energy was investigated. After carrying out a comparison between MD and experimental results, it was quite clear that a better description of the gas-surface interaction potential was required. The H_2/Mg(0001) calculation by Nørskov et al. was the first to include a realistic surface [2]. This total energy calculation was based on the Jellium description for the surface including an atomic structure with pseudopotentials. This was the first real attempt to explain PES features by associating variations in the local state densities with changes in the molecular geometry.

Our understanding of gas-surface reactions has grown considerably in the last twenty years with improvements in both theory and experiment. Although classical dynamics is sufficient for a lot of molecule-surface interaction, for light molecules the nuclei motion should be described by a quantum dynamical method. There are two ways to determine quantum mechanical reaction probabilities, either by solving the time-dependent or the time-independent Schrödinger equation. The first work based on multi-dimensional quantum mechanical calculations presented two-, three-, and four-dimensional results within the time-dependent or wave packet formulation [3]. The influence of all molecular degrees of freedom was first used in either classical mechanics [4] or mixed quantum-classical method [5]. In order to obtain quantitatively accurate reaction probabilities it is necessary to perform six-dimensional (6D) quantum mechanical calculations for light molecules interacting with surfaces. The first 6D quantum dynamical study of the dissociative chemisorption of H_2 on a metal surface consisted of calculations addressing the non-activated dissociation on Pd(100) [6] within a coupled-channel method. The influence of the collision energy [7, 8], incident angle [9], vibrational state [10], rotational conditions [11] and zero point energy [12] on the reaction probabilities was reported in a series of papers. In most associative desorption experiments, the influence of translational motion and ro-vibrational conditions on the reaction can now be determined simultaneously. This can be done by combining the measurement of the polarization dependence of light used to detect the ro-vibrational state in which H_2 is desorbing (using resonance enhanced multiphoton ionization (REMPI)) with time of flight (TOF) techniques. The theoretical results are in agreement with available experimental observations.

We have continued the multi-dimensional quantum dynamical studies for the low-index transition metal surfaces. The motivation of the first part of this work was to understand the non-monotonous behavior of the rotational alignment which was observed in experiment. In the second part, we have studied the influence of the rotational conditions as well as parallel momentum on the reaction probabilities for the more corrugated Pd(110) surface. In the sticking curve as a function of beam energy for D_2/Rh(111), a step was observed [13] at high kinetic energies. In order to clarify this we have investigated the interaction of H_2 on Rh(111) in the third part of this work.

Chapter 2

Theory

In this chapter we will discuss the quantum dynamics theory of the molecule-surface interaction. The continuous potential energy surface is derived from electronic structure calculations. The full-dimensional potential energy surface enters the time-independent Schrödinger equation which is solved with a coupled-channel method.

2.1 Electronic states and potential energy surface

Molecular dynamics simulations imply the solution of two fundamental problems: the first is the determination of the forces exerted between the gas-phase particles and the surface atoms, the second is the development of a suitable collisional model to study the motion of molecules interacting with the surface.

To calculate the total energy for a static configuration of atoms is a complex many-body problem and therefore the exact solution is hard to achieve. The huge difference in the velocities of the electrons and nuclei allows a separation of their motions. This is the well-known Born-Oppenheimer or adiabatic approximation in which the electronic state of the system is at all times determined entirely by the initial state, i.e if we begin in the ground state we will always remain there irrespective of the translational energy of the nuclei.

This approximation implies that the total molecular wavefunction is written as a product of an electronic wavefunction and a nuclear wavefunction

$$\Psi_E = \psi_e(\mathbf{r_e}, \mathbf{R})\phi(\mathbf{R}). \tag{2.1}$$

Let us consider a system comprising of M nuclei and N electrons. By including only electrostatic interactions, the Hamiltonian of the system is given by

$$H = \sum_{\alpha=1}^{M} \frac{\hbar^2}{2M_\alpha}\nabla_\alpha^2 + \sum_{i=1}^{N} \frac{\hbar^2}{2m_e}\nabla_i^2 + V(\mathbf{r_e}, \mathbf{R}), \tag{2.2}$$

in this equation $\mathbf{r_e}$ and $\mathbf{R}$ are used as a shorthand notation for the electronic $\mathbf{r_1}, \mathbf{r_2}, ..., \mathbf{r_N}$ and nuclear $\mathbf{R_1}, \mathbf{R_2}, ..., \mathbf{R_M}$ positions, respectively. All electrostatic interactions, i.e. electron-electron, electron-nuclear, nuclear-nuclear, are included in $V(\mathbf{r_e}, \mathbf{R})$. The mass of the nucleus α is denoted by M_α and m_e is the mass of an electron. The time-independent Schrödinger equation is the starting point

$$H\Psi_E(\mathbf{r_e}, \mathbf{R}) = E\Psi_E(\mathbf{r_e}, \mathbf{R}). \tag{2.3}$$

The electronic wavefunction ψ_e for fixed nuclear positions $\mathbf{R}$ is a solution of the electronic Schrödinger equation

$$\left\{ \sum_{i=1}^{N} \frac{\hbar^2}{2m_e} \nabla_i^2 + V(\mathbf{r_e}, \mathbf{R}) \right\} \psi_e(\mathbf{r_e}, \mathbf{R}) = E_e(\mathbf{R}) \psi_e(\mathbf{r_e}, \mathbf{R}), \tag{2.4}$$

where $E_e(\mathbf{R})$ is now fulfilling the role of a potential function that is usually termed the potential energy surface or PES. Due to its complexity, this quantum mechanical problem has to be simplified before it can be treated. One way to do this is the Hartree-Fock approximation. The total wave function is written as one Slater determinant and fulfills the Pauli exclusion principle for electrons with the same spin by construction. In the Hartee-Fock ansatz, the electron correlation energy is not included, i.e. electrons with opposite spin are still not correlated.

A different view of the problem is the density functional approach. The density functional theory is based on two fundamental theorems by Hohenberg and Kohn.[14]

1. The ground state density $n(\mathbf{r_e})$ of a system of interacting electrons in an external potential uniquely determines this potential,

2. The true ground state density $n(\mathbf{r_e})$ minimizes the total energy functional $E[n]$.

The energy functional can be written in the following form

$$E[n] = \int V_{ext}(\mathbf{r_e}, \mathbf{R}) n(\mathbf{r_e}) d\mathbf{r_e} + \frac{1}{2} \int \int \frac{n(\mathbf{r_e}) n(\mathbf{r'_e})}{|\mathbf{r_e} - \mathbf{r'_e}|} d\mathbf{r_e} d\mathbf{r'_e} + T_s[n] + E_{xc}[n]. \tag{2.5}$$

T_s is the kinetic energy of the system, V_{ext} corresponds to the electron-nuclear interaction and all the remaining contributions to the energy are now contained in the last term, $E_{xc}[n]$, the so called exchange-correlation energy.

The exchange-correlation functional $E_{xc}[n]$ is not known in general, therefore it has to be approximated. One simple idea is to construct an energy functional which is exact in the limit of slowing varying charge densities (*local density approximations (LDA)*)

$$E_{xc}^{LDA} = \int n(\mathbf{r_e}) \epsilon_{xc}(n(\mathbf{r_e})) d\mathbf{r}, \tag{2.6}$$

where $\epsilon_{xc}(n(\mathbf{r_e}))$ is the exchange-correlation energy per particle which depends on the electron density distribution $n(\mathbf{r_e})$.

More general approximations, where E_{xc} is approximated by an expansion in higher order terms of the density gradient, are called *generalized gradient approximations (GGA)*. If we consider only the first order gradients, the exchange-correlation energy can be written as

$$E_{xc}[n] = \int n(\mathbf{r_e}) \epsilon_{xc}(n, \nabla n) d^3\mathbf{r_e}. \tag{2.7}$$

It can be expected that GGA will give better ground-state properties than LDA, since GGA was constructed to be a more precise approximation to the true density function. With electronic structure techniques, the total energy can be calculated with great accuracy for each **R**.

To map out the PES for a static surface we change the location, bond length and orientation of the molecule and compute the electronic energies for each discrete configuration of the nuclei. Since the potential depends on the nuclear coordinates, the electronic wavefunctions depend parametrically on **R** and the eigenvalue E_e is a function of the nuclear coordinates. By inserting E_e in the Schrödinger equation for the total system, and neglecting the coupling terms between nuclear and electronic motions, we arrive at the Schrödinger equation of the nuclear motion

$$\{\sum_{\alpha=1}^{M} \frac{\hbar^2}{2M_\alpha}\nabla_\alpha^2 + E_e^{BO}(\mathbf{R})\}\phi(\mathbf{R}) = E\phi(\mathbf{R}). \tag{2.8}$$

The last equation expresses that the nuclei move in an effective potential which is the electronic energy as a function of the internuclear distances.

2.2 Functional form of PESs

The potential energy surface plays a fundamental role in the understanding of collision processes between atoms and molecules. Total energy *ab initio* calculations within the concept of density functional theory just provide total energies for discrete configurations of the nuclei. In classical dynamics simulations we can use one particular configuration at any time but in order to perform a quantum dynamics simulation we have to determine a continuous representation of the potential energy. It is necessary to fit the points with analytic functions having the correct asymptotic behavior in agreement with the general topology of PESs. However it is still a major task as many different functions and parameters are required.

Although low-dimensional simulations are very important to understand and interpret the dynamics, the validation of electronic structure methods through comparisons with experiment often requires accurate high-dimensional simulations. The achievement of this goal requires the availability of accurate determination of high-dimensional potential energy surfaces.

In order to improve dynamics results, several fitting and interpolation methods have been proposed to build suitable analytical representation of the PES. The analytical representation of the potential energy surface can be either local or global. The local formulation of the PES relies on the adoption of simple functionals each describing a limited region of the interaction. On the contrary, global interpolations have a more complex analytical form to provide an accurate fit of the potential over the whole configuration space. One of the major goals in theoretical surface science is to be able to determine global high-dimensional PESs for such systems. In the next step we will address some of the fitting and interpolation methods based on *ab initio* calculations that have been applied to reactions of diatomic molecules with surfaces.

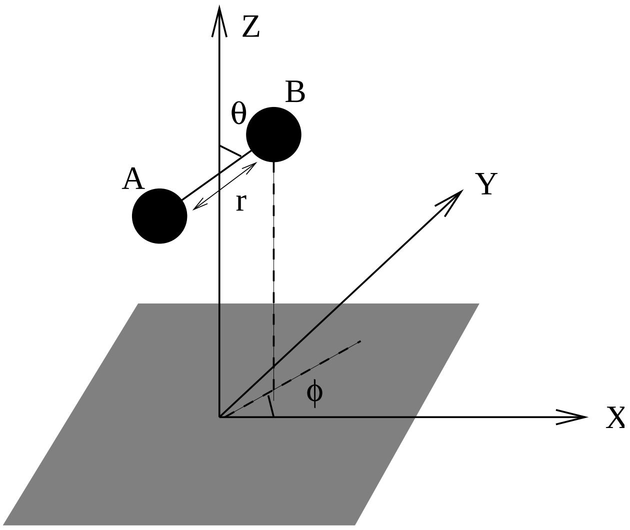

Figure 2.1: The six degrees of freedom of a diatomic molecule in the presence of a surface

2.2.1 Interpolations of PES based on *ab initio* calculations

The first analytical formulations of PES were derived from the LEPS and DIM potentials. In the *London-Erying-Polanyi-Sato (LEPS)*[15] method the functional form of the PES is expressed as

$$\begin{aligned} V &= U_m(\mathbf{R}) + U_a(\mathbf{R_1}) + U_a(\mathbf{R_2}) - \{V_m^2(\mathbf{R}) + [V_a(\mathbf{R_1}) + V_a(\mathbf{R_2})]^2 \\ &- V_m(\mathbf{R})[V_a(\mathbf{R_1}) + V_a(\mathbf{R_2})]\}^{1/2}, \end{aligned} \tag{2.9}$$

where U_m and V_m depend on the molecular coordinates, R, and U_a and V_a on the coordinates of the two atoms in the molecule, R_1 and R_2. U_a (U_m) and V_a (V_m) are the coulomb and exchange integrals in a Heitler-London model, and are chosen such that V reduces to the Morse potential at $Z \to \infty$ and describes atomic chemisorption potentials at large r and small Z, where r and Z are the internuclei distance and the height of the molecule above the surface. The barrier height and location can be well reproduced by parameters in the U_a (U_m) and V_a (V_m) functions. Although this fitting gives good qualitative description of the topologies of many different PESs, it can be very difficult to fit *ab initio* energies with this form. It is very useful, if LEPS is used as a guide for the PES in low symmetry configurations.

Within the *corrugation reducing procedure (CRP)*[16] the full 6D molecule-surface potential S_{6D} is written as the sum of 3D atom-surface potentials $R_{A,B}$ and the 6D interpolation function, I_{6D}

$$S_{6D}(X,Y,Z,r,\theta,\phi) = I_{6D}(X,Y,Z,r,\theta,\phi) + R_A(X_A,Y_A,Z_A) + R_B(X_B,Y_B,Z_B), \tag{2.10}$$

By this method we remove the large corrugation with respect to the atomic degrees of freedom (corrugation reducing procedure) and we are more easily able to interpolate the smoother function I_{6D} by using low order basis functions. An interpolation over (r, Z) can be obtained from *ab initio* calculations, trigonometric functions are used as basis functions for the interpolation over ϕ and θ and Fourier expansion for (X, Y). The 3D interaction potential between the surface and the atoms are also determined from *ab initio* calculations.

The potential energy surface in the *modified Shepard interpolation* [17, 18] scheme at some nuclear arrangement, X, is expressed as the sum of contributions from several data points as

$$V^{MS}(X) = \sum_{i=1}^{N_D} W_i(R) V_i(X), \tag{2.11}$$

where X and R are $3N$ Cartesian and $3N-6$ internal coordinates and N_d is the number of data points. The Taylor expansion about data points has the following form

$$\begin{aligned} V_i(\mathbf{X}) &= V^{(i)} + \sum_{j=1}^{3N} (X_j - X_j^{(i)}) \frac{\partial V}{\partial X_j}\Big|_{X=X^{(i)}} \\ &+ \frac{1}{2} \sum_{j,k=1}^{3N} [X_j - X_j^{(i)}][X_k - X_k^{(i)}] \frac{\partial^2 V}{\partial X_j \partial X_k}\Big|_{X=X^{(i)}}, \end{aligned} \tag{2.12}$$

where $V^{(i)}$, $\frac{\partial V^{(i)}}{\partial X_j}$ and $\frac{\partial^2 V^{(i)}}{\partial X_j \partial X_k}$ are the potential energy, the jth component of the gradient vector, and the jkth component of the Hessian matrix, calculated by *ab initio* electronic structure calculations at $X^{(i)}$. The weight function is proportional to

$$W_i(\mathbf{R}) \propto \sum_{j}^{3N-6} \left\{ (R_j - R_j^{(i)})^2 \right\}^{-p}, \tag{2.13}$$

where $2p$ should be greater than $3N-6$ and the order of the Taylor expansion.

An other method is to define the PES based on the symmetry property of the surface. In the present work we have expanded the potential of a diatomic molecule interacting with a surface in functions which are adapted to the symmetry of the surface.

2.2.2 PES adapted to the surface symmetry

The potential energy surface for our quantum dynamics calculations have been determined by *ab initio* calculations. Neglecting relaxation effects, the potential energy surface for the dissociative adsorption of a diatomic molecule over a surface is six-dimensional. One possible set of coordinates consists of the bond length r and the distance of the molecule's center of mass from the surface Z, two lateral coordinates that describe the position of the center of mass X,Y and two rotational degrees of freedom θ,ϕ (see Fig. 2.1). The analytical representation of the PES should be determined by a set of parameters and functions, as large as necessary and as small as possible without loosing important information. In order to solve the time-independent Schrödinger equation within the coupled-channel method, the coordinates in the Zr plane should be transformed into the reaction path coordinate s and the vibrational coordinate ρ perpendicular to the reaction path. We fit the PES along this direction by analytical functions adapted to the asymptotic behavior with a set of parameters

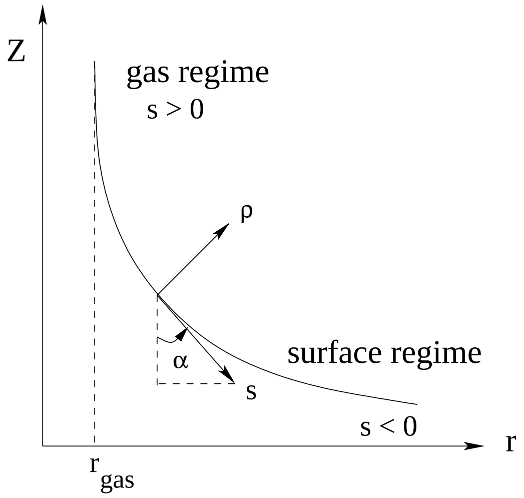

Figure 2.2: Illustration of the reaction path in Zr plane. Z is the center of mass distance from the surface and r is internuclei distance.

as a function of s-coordinate. As the first step a general reaction coordinate has to be defined, which describes all calculated pathways. This reaction path coordinate is defined via its curvature $\kappa(s)$

$$\kappa(s) = \frac{1}{R_0 \cosh^2(\beta(s - s_0))}. \tag{2.14}$$

Generally R_0, β will be determined from the minimum energy path found in the *ab initio* calculation.
The integral over the curvature defines the angle between the axis $r = r_0$ $(Z \longrightarrow \infty)$ and the reaction path which is illustrated in Fig 2.2

$$\alpha(s) = \int_{\infty}^{s} \kappa(s')ds' = \frac{1}{\beta R_0}(\tanh(\beta(s - s_0)) - 1). \tag{2.15}$$

The relation between the coordinates (Z, r) and the reaction path coordinate are given by an integral over trigonometric functions of the angle α

$$\begin{aligned} Z'(s) &= Z'_{gas} + \int_{s_\infty}^{s} \cos\alpha(s')ds' \\ r(s) &= r_{gas} + \int_{s_\infty}^{s} \sin\alpha(s')ds', \end{aligned} \tag{2.16}$$

where Z' is the mass scaled height $Z\sqrt{\frac{M}{\mu}}$ with the reduced mass μ and total mass M.
The PES should be adapted to the symmetry of the surface, therefore there is no general analytical form of the PES for different lattice structures. For the general discussion, the functional form of potential energy surface for a diatomic molecule over a fcc(100) surface will be considered.

The common way to describe the energy along the valleys of the elbows is to write a linear combination of terms with the structure

$$Y_{lm}(\theta, \phi) \cos(nGX) \cos(nGY), \tag{2.17}$$

where $G = 2\pi/a$ is the lattice constant of the reciprocal lattice and a is the lattice constant. The spherical harmonic induces transitions in the rotational l and azimuthal quantum numbers m, while the cos-terms are responsible for lateral momentum transitions. The investigation of a low-dimensional PES is very important to understand the role of different degrees of freedom of the molecule in the dissociation mechanism, therefore it is useful to separate the PES into the *corrugational*, *rotational* and *vibrational* parts. The corrugational, rotational, vibrational parts describe the dependence of the lateral coordinates on the topology of the surface, the effect of the anisotropy of the surface and the change of the vibrational frequency along the reaction path, respectively. The explicit dependence of the potential on the molecular orientation is termed anisotropy. It must be noticed that the anisotropy and corrugation are not independent due to the coupling of lateral and orientational coordinates in the potential energy function. According to the symmetry and data points of the *ab initio* calculation the following linear combinations are allowed

$$\begin{aligned} V^{corr} &= \sum_{m,n=0}^{2} V^{(c)}_{m,n}(s) \cos mGX \cos nGY \\ V^{rot} &= \sum_{m,n} \frac{1}{2} V^{(r1)}_{m,n}(s) \cos^2\theta \cos mGX \cos nGY \\ &+ \sum_{n=1}^{2} \frac{1}{2} V^{(r2)}_{n}(s) \sin^2\theta \cos 2\phi (\cos nGX - \cos nGY) \\ &+ \sum_{m,n=0}^{1} \frac{1}{2} V^{(r3)}_{m,n} \sin^4\theta \cos 4\phi \cos mGX \cos nGY. \end{aligned} \tag{2.18}$$

To determine the vibrational part of the PES, we have to consider the deviation of a certain pathway from the minimum reaction path

$$\Delta\rho(s, X, Y) = \frac{1}{2} d(s)(\cos GX + \cos GY), \tag{2.19}$$

where $d(s)$ is defined as $d(s) = d_0/\cosh^2(\beta(s - s_0))$ such that d_0 is the maximum displacement from the minimum reaction path. The change of the vibrational frequency could be determined by

$$\omega(s) = \omega_{gas}(1 - n(1 - \tanh\gamma(s - s_{vib}))), \tag{2.20}$$

the factor n corresponds to the relative change of the vibrational frequency along the reaction path. The length parameters γ and s_{vib} control the rate and position of the reduction of vibrational frequency. Then the vibrational part of the potential is

$$V^{vib} = \frac{\mu}{2}\omega^2(s)[\rho - \Delta\rho(s, X, Y)]^2. \tag{2.21}$$

The complete functional form of the potential energy surface is

$$V(s,\rho,X,Y,\theta,\phi) = V^{corr} + V^{rot} + V^{vib}. \tag{2.22}$$

The reaction path coefficients $V_{mn}(s)$ in Eq. (2.18) can be determined by a suitable choice of parameters in the combination of the functions which are adapted to the asymptotic behavior

$$\begin{aligned} V_{mn}(s) &= \sum_i A_{mn}^{(i)} \cosh^{-2}(B_{mn}^{(i)}(s - C_{mn}^{(i)}) \\ &+ D_{mn}^{(i)}(1 - \tanh(E_{mn}^{(i)}(s - F_{mn}^{(i)}))) \\ &+ G_{mn}^{(i)} \frac{\tanh(H_{mn}^{(i)}(s - I_{mn}^{(i)}))}{\cosh^2(J_{mn}^{(i)}(s - K_{mn}^{(i)}))}, \end{aligned} \tag{2.23}$$

the parameters A_{mn}, B_{mn} should be chosen so that the difference between fitting points and *ab initio* data points are as small as possible for each configuration, especially at the minimum and transition points, because of the crucial role of these regions in the dissociation process. The fitting method is based on 2D cuts through the high-dimensional potential energy surface so that the fitting and *ab initio* 2D cuts should be similar.

2.2.3 Analysis of surface topology

One way to map the energy surface is to make two-dimensional cuts through the energy surface, so-called elbow-plots; the two rotational angles and the two lateral coordinates are fixed and only the bond length and center of mass distance from the surface are varied. The schematic form of the elbow plot is shown in Fig. 2.3. Three major regions can be distinguished.

Entrance region: The reacting objects are still in their initial condition and the bond length dose not vary.

Reaction region: Starting the reaction; in this region charge transfer is dominant.

Adsorption region: The separation of the molecule into two atoms.

The location of the barrier within the reaction region (early and late barrier) determines the importance of molecular vibration in the dynamics. The vibrational mass of the molecule increases by a factor of 4 from the reduced mass to the total mass as the molecule moves through the reaction zone. This causes the vibrational levels to drop by a factor of 2. As far as vibrationally adiabatic effects are concerned, for an early barrier dropping of the vibrational levels occurs after the barrier, therefore it does not influence the dynamics, while for a late barrier it results in a vibrational state dependent decrease in the barrier height. In addition, the curvature of the reaction path couples the different vibrational states in the reaction zone, and if sufficiently strong, can induce vibrational transition. Thus from the form of elbow-plot, we are able to assess the crucial role of quantum vibrational states in the dynamics process.

On the basis of *ab initio* calculations, two general forms of corrugation, so-called *energetic* and *geometric*, have been identified. Not only the height of the barriers can be changed for each configuration (*energetic* corrugation) but also the barrier width

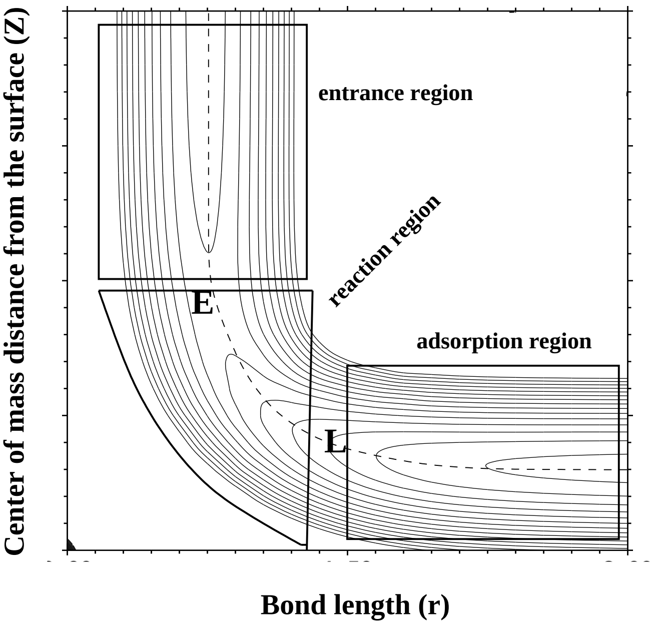

Figure 2.3: The two-dimensional potential surface, a so-called elbow potential, indicates the two important coordinates for understanding of the adsorption process. The reaction path is illustrated by the dash line . If the maximum of the dissociation barrier lies at the beginning of the reaction region, it is called early (E) and if it is at the beginning of adsorption region, it is called late (L).

(*geometric* corrugation). In the dynamical process the effect of the surface corrugation appears in the dependence of the sticking probability on the angle of incidence or parallel momentum of the molecular beam. The influence of the two types of corrugation on the parallel momentum of the molecule are different, therefore it is useful to distinguish between these two types of corrugation. Another presentation of the potential energy surface by which we can distinguish between the two types of corrugation, is a two-dimensional cut of the PES along the reaction path and one lateral coordinate. The energetic and geometric corrugation as a function of reaction path and surface coordinate X have been plotted in the Fig. 2.4. Fig (2.4a) corresponds to the simple corrugated Gaussian function and the geometric corrugation (Fig. 2.4b) is proportional to the simple function

$$V(X, s) \propto \cosh^{-2}\Big(\alpha(s - s_0(1 + \cos GX))\Big). \tag{2.24}$$

In the energetic corrugation the barrier height at the different sites might vary, but at each site the barrier occurs at the same point along the reaction path, while in the geometric corrugation only the barrier position is varied. In real systems combinations of both corrugations are found. In the application section we will see the influence of the two types of corrugation on the dissociation of H_2 over Pd(110).

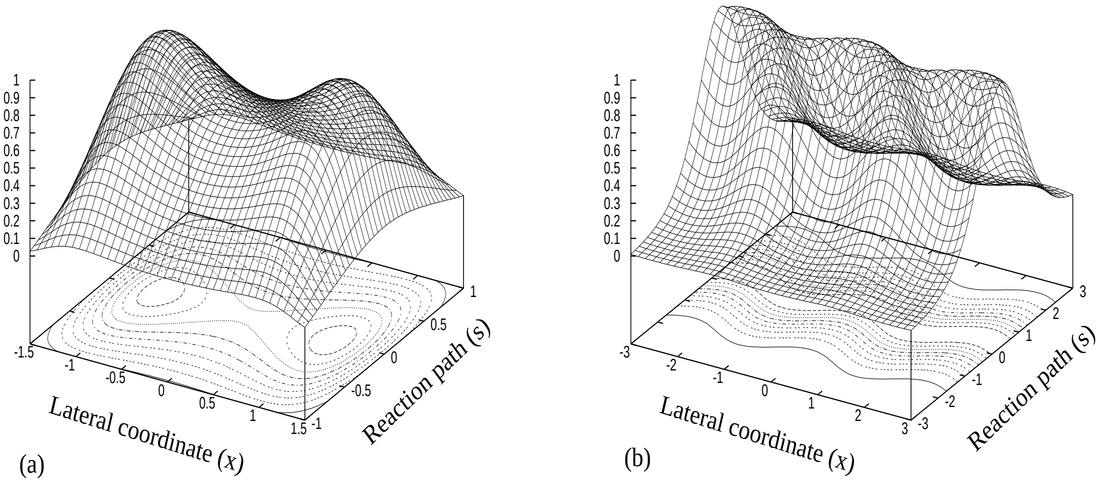

Figure 2.4: The underlying contour map is plotted as a function of the reaction path and its position in the unit cell. a) The height of the barriers varies at different sites but at each site the barrier occurs at the same point on the reaction path. This is illustrated for a simple corrugated Gaussian (energetic corrugation). b) The barrier positions are varied along the reaction path (geometric corrugation).

2.3 Dynamics of molecule-surface interaction

Surface processes can be assisted either by phonon or electron excitation processes in the substrate. Within semiclassical methods both these effects can be included in the dynamics. In order to study dynamics of H_2-surface interaction, quantum effects have to be taken into account due to the light mass of H_2. Because of the large mass mismatch between H_2 and substrate metal atoms in the quantum mechanical simulations the surface is usually assumed to be rigid. There are systems such as H_2 adsorption on Silicon where the energy transfer to the surface has been considered in the adsorption and desorption process using the surface oscillator model[19].

In order to solve Eq.(2.8), using quantum mechanics, an additional approximation should be made, because the ionic degrees of freedom R also include phonons. With the "rigid surface approximation", we are able to solve the system fully quantum mechanically with no dynamics approximations. The remaining degrees of freedom in Eq. (2.8) are the six molecular coordinates. The kinetic part of Eq. (2.8) can be expressed as a center of mass and relative nuclear motions, therefore the full-dimensional Hamiltonian for nuclear motion without phonon excitation is given by

$$H_{6D} = -\frac{1}{2M}\nabla^2_{\mathbf{R}} - \frac{1}{2\mu}\nabla^2_{\mathbf{r}} + V_{6D}(\mathbf{R}, \mathbf{r}), \tag{2.25}$$

where $\mathbf{R}$ is the vector of the center of mass coordinates (X, Y, Z) of the molecule, $\mathbf{r}$ the vector of the internal coordinates of the molecule (r, θ, ϕ) , M is the total mass and μ the reduced mass of the molecule. The internal part of the Hamiltonian can be expanded in terms of spherical coordinates

$$H_{6D} = -\frac{1}{2M}\nabla^2_{\mathbf{R}} - \frac{1}{2\mu}(\frac{\partial^2}{\partial r^2} + \frac{2}{r}\frac{\partial}{\partial r} - \frac{\mathbf{L}^2}{r^2}) + V_{6D}(\mathbf{R}, r, \theta, \phi), \tag{2.26}$$

with angular momentum operator $\mathbf{L}$.

The function r_e is defined as the equilibrium bond length, which is in principle a function of the other five coordinates X, Y, Z, θ and ϕ. The vibrational amplitude is usually small compared to the equilibrium bond length, this assumption means

$$|r_e(X, Y, Z, \theta, \phi) - r| \ll r. \tag{2.27}$$

With this assumption we can neglect the term $(2/r)(\partial/\partial r)$ in the Hamiltonian and the angular momentum part can be modified by $\mathbf{L}^2/r^2 \to \mathbf{L}^2/r_e^2$. Then the Hamiltonian can be simplified to

$$H'_{6D} = -\frac{1}{2M}\nabla^2_{\mathbf{R}} - \frac{1}{2\mu}(\frac{\partial^2}{\partial r^2} - \frac{\mathbf{L}^2}{r_e^2}) + V_{6D}(\mathbf{R}, r, \theta, \phi). \tag{2.28}$$

Because of the transformation of (Z, r) into the reaction path coordinates (s, ρ) as mentioned in Sec. 2.2.2, we use the mass scale height $(Z' = Z\sqrt{\frac{M}{\mu}})$ to express the Hamiltonian in terms of the reaction path coordinate

$$\begin{aligned} H'_{6D} &= -\frac{\hbar^2}{2\mu}\left(\eta^{-1}\frac{\partial}{\partial s}\eta^{-1}\frac{\partial}{\partial s} + \eta^{-1}\frac{\partial}{\partial \rho}\eta\frac{\partial}{\partial \rho} + \frac{\mathbf{L}^2}{r_e^2}\right) \\ &\quad -\frac{\hbar^2}{2M}\left(\frac{\partial^2}{\partial X^2} + \frac{\partial^2}{\partial Y^2}\right) + V_{6D}(X, Y, s, \rho, \theta, \phi), \end{aligned} \tag{2.29}$$

in which the coupling parameter η is defined by

$$\eta = 1 - \kappa(s)\rho, \tag{2.30}$$

where $\kappa(s)$ is the curvature of the lowest energy reaction path defined in Eq. (2.14) (the dashed line in Fig. (2.3)). The displacement of the minimum reaction path along the ρ axis is taken into account in the equilibrium bond length

$$r_e = r_e^0(s) + \cos\alpha(s)\Delta\rho(X, Y, s), \tag{2.31}$$

where $\alpha(s)$ and r_e^0 have been defined in the Eq. (2.15) and Eq. (2.16), respectively.
Within the vibrationally adiabatic approximation, this displacement from the minimum reaction path is neglected which is justified if $\cos\alpha_r(s)\Delta\rho(X, Y, s) \ll r_e^0$.
The scattering wave function is expanded as

$$\Psi_{6D}(X, Y, s, \rho, \theta, \phi) = \sum_{\mathbf{G}_{\parallel}jmi} \Phi_{\mathbf{G}_{\parallel}jmi}(s)e^{i(\mathbf{G}_{\parallel}+\mathbf{k}_{\parallel})\cdot\mathbf{R}_{\parallel}}Y_{jm}(\theta, \phi)\chi_i(\rho), \tag{2.32}$$

the lateral, rotational and vibrational motions are described by plane waves, spherical harmonic and harmonic oscillator eigenfunctions, respectively. $\mathbf{R}_{\parallel}$ is the two-dimensional vector (X, Y) describing the lateral coordinates of the molecule center of

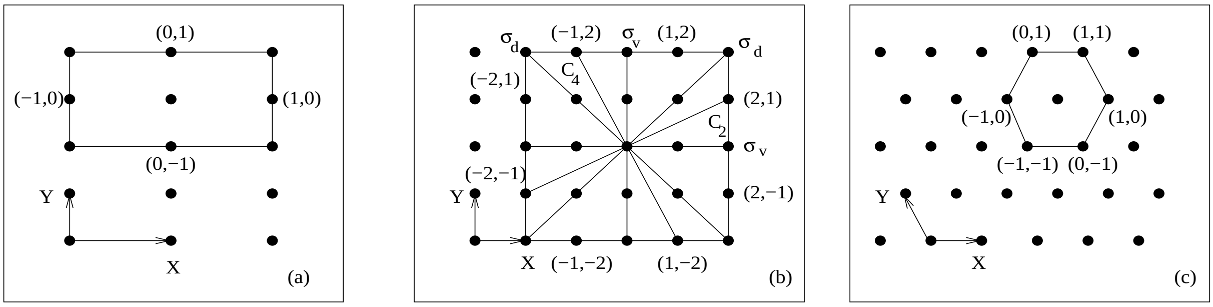

Figure 2.5: The two-dimensional lattice structure of a) fcc(110), b) fcc(100) and c) fcc(111) surfaces. The reciprocal lattice vector (G_{mn}) of the symmetry points are equivalent distance so that there are two equivalent channels for fcc(110), eight for fcc(100) (in the second levels of diffraction) and six for fcc(111). The equivalent $(2,1)$ points, in the case of the (100) symmetry, can be obtained by the appropriate symmetry operators, i.e. reflections and rotations.

mass, and $\mathbf{G}_{\|}$ are the vectors of the two-dimensional reciprocal lattice of the surface. Substitution of the scattering wave function in the Schrödinger equation, multiplying from the left with $e^{-i(\mathbf{G}'_{\|}+\mathbf{k}_{\|})\cdot\mathbf{R}_{\|}}Y_{j'm'}(\theta,\phi)\chi_{i'}(\rho)$ and integration over the coordinates X, Y, ρ, θ and ϕ leads to the coupled-channel equation

$$\begin{aligned}&\sum_{\mathbf{G}_{\|}jmi}\Big\{\Big[\frac{-\hbar^2}{2\mu}\eta^{-1}\frac{\partial}{\partial s}(\eta^{-1}\frac{\partial}{\partial s})+\hbar\omega(s)(i+1/2)+\frac{\hbar^2}{2\mu r_e^2}j(j+1)\\ +\;&\frac{\hbar^2}{2M}\mathbf{G}_{\|}^2-E\Big]\delta_{\mathbf{G}_{\|}\mathbf{G}'_{\|}}\delta_{ii'}\delta_{jj'}\delta_{mm'}+\int e^{-i(\mathbf{G}'_{\|}+\mathbf{k}_{\|})\cdot\mathbf{R}_{\|}}Y_{j'm'}(\theta,\phi)\chi_{i'}(\rho)\\ &V(X,Y,s,\rho,\theta,\phi)e^{i(\mathbf{G}_{\|}+\mathbf{k}_{\|})\cdot\mathbf{R}_{\|}}Y_{jm}(\theta,\phi)\chi_i(\rho)\Big\}\Phi_{\mathbf{G}_{\|}jmi}(s)=0.\end{aligned}\tag{2.33}$$

In this work this equation is solved within the concept of a coupled-channel method which will be explained in the next section. Actually, the lateral, rotational and vibrational motions of the molecule are described by well-known quantum wave functions and Eq. (2.33) determines the influence of the quantum numbers of the molecule (channels) along the reaction path during the dissociation process.

2.3.1 Coupled-channel equation and symmetry of the surface

In general, a large number of channels are required for the convergence of coupled channel methods. As computing time for such calculations is large, it is very useful to consider the symmetry properties of the surface. The application of symmetry reduces the number of coupled equations. Expanding the wave function into symmetry adapted basis functions enables us to represent the problem in its irreducible representation.
Consider Eq. (2.33): the matrix element of the potential energy along the lattice vectors (X,Y) is proportional to

$$V'_{mn,m'n'}\propto\int exp[-i(\mathbf{G}_{mn}+\mathbf{k}_{||})\cdot\mathbf{R}_{||}]V'(\mathbf{R}_{||})exp[i(\mathbf{G}_{m'n'}+\mathbf{k}_{||})\cdot\mathbf{R}_{||}]dXdY,\tag{2.34}$$

where $\mathbf{R}_{||} = (X, Y)$, $\mathbf{k}_{||} = (k_X, k_Y)$, $\mathbf{G}_{mn} = (2\pi m/a_X, 2\pi n/a_Y)$ are the reciprocal space vectors with lattice constants (a_X, a_Y) and $V(\mathbf{R}_{||})$ is the two dimensional periodic potential energy in the surface (X, Y) plane.
Consider a normal incidence beam $\mathbf{K}_{||} = (0, 0)$ on the fcc(100) lattice (Fig. 2.5b). $S_{0,0,m,n}$, the S-matrix element for scattering from the incident $(0, 0)$ channel into the final (m, n) must satisfy the relations

$$S_{00,mn} = S_{00,\pm m,\pm n} = S_{00,\pm n,\pm m}, \tag{2.35}$$

i.e. there are eight equivalent channels if $m \neq n \neq 0$, four if $m = n \neq 0$; or $m \neq 0$, $n = 0$; or $m = 0$, $n \neq 0$ (see Fig 2.5). This property is due to the invariance of Eqs. 2.33 (for $\mathbf{k}_{||} = (0, 0)$) under symmetry operations of the point group C_{4v}. To take advantage of this symmetry, one performs a transformation from the diffraction channel basis $H_{mn} := exp[i(\mathbf{G}_{mn}) \cdot \mathbf{R}_{||}]$ to a symmetry-adapted basis. The new basis functions are linear combinations of the H_{mn}, with coefficients corresponding to the irreducible representations of the group C_{4v} (see table 2.1). The totally symmetric (A_1) representation, for instance, is

$$\begin{aligned} A_1(m, n) &= 8^{-1/2}\Big(H_{mn} + H_{m(-n)} + H_{(-m)n} + H_{(-m)(-n)} \\ &+ H_{nm} + H_{n(-m)} + H_{(-n)m} + H_{(-n)(-m)}\Big). \end{aligned} \tag{2.36}$$

The eight equivalent points of fcc(100) are plotted in Fig. (2.5b). If the transformation to the symmetry-adapted basis is applied to Eqs. (2.33) or alternatively Eq. (2.34), a decoupling is obtained into separate coupled equations for each symmetry species. The application of a symmetry-adapted basis is not restricted to normal incidence. We can consider the case of $\mathbf{k}_{||} = \mathbf{G}_{kl}$ with integer values k, l. The vector addition of $\mathbf{k}_{||}$ and $\mathbf{G}_{mn}$ appears in the addition of indices

$$\mathbf{k}_{||} + \mathbf{G}_{mn} = \mathbf{G}_{k+m,l+n}, \tag{2.37}$$

then the coupled equations are exactly the same if we introduce a relabeling

$$k + m, l + n \rightarrow m, n. \tag{2.38}$$

For off-normal incident angle, it is necessary to obtain the symmetry adapted basis for the non-totally symmetric elements. The non-totally symmetric irreducible representation is obtained by a combination of the A_2, B_1, B_2 and $2E$ representations, which are listed in table (2.1). The sign of the linear combination of the H_{mn}s for each representation under certain transformation is shown in table 2.1. For example, the A_2 representation is expressed by

$$\begin{aligned} A_2(m, n) &= 8^{-1/2}\Big(H_{mn} - H_{m(-n)} - H_{(-m)n} + H_{(-m)(-n)} \\ &- H_{nm} + H_{n(-m)} + H_{(-n)m} - H_{(-n)(-m)}\Big). \end{aligned} \tag{2.39}$$

Table 2.1: C_{4v} point group. A_1, A_2 : non- degenerate symmetric representation with respect to C_n, B_1, B_2 : non-degenerate antisymmetric representation with respect to C_n and E: doubly degenerate representation.

C_{4v}	E	$2C_4$	C_2	$2\sigma_v$	$2\sigma_d$
A_1	1	1	1	1	1
A_2	1	1	1	-1	-1
B_1	1	-1	1	1	-1
B_2	1	-1	1	-1	1
E	2	0	-2	0	0

The two doubly degenerate E combinations have been obtained with the following four functions

$$\begin{aligned}
E_{1a}(m,n) &= \frac{1}{2}[H_{mn} + H_{m(-n)} - H_{(-m)(-n)} - H_{(-m)n}] \\
E_{1b}(m,n) &= \frac{1}{2}[H_{mn} - H_{m(-n)} - H_{(-m)(-n)} + H_{(-m)n}] \\
E_{1c}(m,n) &= \frac{1}{2}[H_{nm} + H_{n(-m)} - H_{(-n)(-m)} - H_{(-n)m}] \\
E_{1d}(m,n) &= \frac{1}{2}[H_{nm} - H_{n(-m)} - H_{(-n)(-m)} + H_{(-n)m}]. \qquad (2.40)
\end{aligned}$$

The application of surface symmetry properties to reduce the coupled equations, is not limited to the C_{4v} group and it is very useful for the higher symmetry group of the hexagonal lattice. The symmetry reduction in the rectangular lattice is of course less, but still useful.

2.3.2 INTRA-LORE method

The INTRA-LORE method is a numerically stable solution of the coupled-channel equations. A typical problem in the numerical solution of the time-independent Schrödinger equation using the coupled-channel method is stability. For a given total energy there are the so-called closed-channels with negative kinetic energy. In the second order Schrödinger equation this negative kinetic energy corresponds to the exponentially growing wave. By the INTRA-LORE method we are able to calculate directly the observable scattering matrix elements without the calculation of the wave functions. The second order Schrödinger equation can be transformed into the two first order differential equations in terms of local reflection matrix (LORE) and inverse local transmission matrix (INTRA).

As a simplification we will first consider the pure reflection case (LORE) without any curvature of the reaction path (no change in bond length), in the second part we will derive the INTRA matrix and then the curvature of the reaction path in the equations of the LORE and INTRA schemes will be also taken into account.

I. Local reflection matrix without curvature

In the pure reflection case, the potential increases indefinitely in one direction ($s \rightarrow -\infty$) of the reaction path and vanishes in the opposite direction ($s \rightarrow +\infty$). In the absence of curvature of the reaction path the kinetic energy is just proportional to the second derivative of the wavefunction $\psi(s, m)$ (m stands for the internal quantum numbers: vibrational and rotational quantum number and reciprocal wave vector). If ϵ_m is the energy of the internal state m, the wave number of the m-th channel is given by $\hbar^2 k_m^2 = \hbar^2 k^2 - 2M\epsilon_m$, M is the mass. The first step is to introduce a matrix notation of Schrödinger equation. We begin with the diagonal matrices

$$\begin{aligned} 1 &:= \delta_{mn} \\ k &:= k_m \delta_{mn}, \end{aligned} \tag{2.41}$$

which are independent of the reaction coordinate s. The potential has off-diagonal elements and depends on s

$$V(s) \ := \ V_{mn}(s). \tag{2.42}$$

The wave function $\psi(s, m)$ which is a vector, to begin with, can be considered as a matrix, too. For this purpose we introduce a second index n labeling the internal quantum numbers according to the internal conditions, $\Psi(\rho, s, m)_n$ denotes the solution of the Schrödinger equation with an incident plane wave of amplitude one in channel n and zero in all other channels. Then one can introduce a matrix representation of the wave function by

$$\Psi(s) := \Psi(s, m)_n = \Psi_{mn}(s). \tag{2.43}$$

The Schrödinger equation then takes the simple matrix form (in atomic units, i.e. $2m = \hbar = 1$)

$$\psi''(s) = (V(s) - k^2)\psi(s) = -q^2(s)\psi(s). \tag{2.44}$$

Here we have introduced a local wave number matrix $q(s)$. The sign of the square root is chosen such that $q(s)$ is positive in the allowed regions ($q^2 > 0$) and positive imaginary in the classically forbidden region ($q^2 < 0$). The logarithmic derivative of the wave function

$$\lambda(s) := \psi'(s)\frac{1}{\psi(s)}, \tag{2.45}$$

obeys then the Ricatti differential equation

$$\lambda'(s) + \lambda^2(s) = -q^2(s). \tag{2.46}$$

In the asymptotic region ($s \rightarrow +\infty$; $V(s) = 0$) the Schrödinger function for open channels ($k_m^2 > 0$) behaves as

$$\psi(s) = e^{-iks} - re^{iks}, \tag{2.47}$$

with the reflection coefficient r. The logarithmic derivative of this function can be written as

$$\lambda =: -ik\frac{1+\rho}{1-\rho} \quad ; \quad \rho = e^{iks} r e^{iks}. \tag{2.48}$$

For the general case we define now the local reflection coefficient (LORE) $\rho(s)$ by the equation

$$\lambda(s) =: -iq(s)\frac{1+\rho(s)}{1-\rho(s)}. \tag{2.49}$$

Taking the derivative of this equation and using equation (2.46) one finds, after some rearrangements:

$$\rho'(s) = i(q(s)\rho(s) + \rho(s)q(s)) - \frac{1}{2}(1-\rho(s))\frac{1}{q(s)}q'(s)(1+\rho(s)), \tag{2.50}$$

which is the differential equation for the LORE. It has the useful property that for a piecewise constant potential the first term on the r.h.s. vanishes at the steps and the second term at the plateaus. For that reason we will transform the potential for the calculation always into a piecewise constant one. In the following, we will use $V_m = V(s_m)$ for the potential at the reaction path position s_m with a discrete index m that refers to the m-th segment of the reaction path, starting with $m = 1$ far in the forbidden region ($s \to -\infty$). So we will use the short hand notation $a_m := a(s_m)$ for all s-dependent quantities.

At the plateaus the solution of Eq. 2.50 can be written as

$$\rho(s) = e^{iqs}\rho_0 e^{iqs}, \tag{2.51}$$

so that the propagation of ρ_m along a plateaus with step width d is described by

$$\rho_m^+ = e^{iq_m d}\rho_m^- e^{iq_m d}. \tag{2.52}$$

The superscripts + and - refer to the values at the left and right hand side of the plateaus.

For the steps, the logarithmic derivative has to be continuous, which means

$$q_{m+1}\frac{1+\rho_{m+1}}{1-\rho_{m+1}} = q_m\frac{1+\rho_m}{1-\rho_m}. \tag{2.53}$$

We can now introduce the relative index of reflection at the step

$$n = \frac{1}{q_m}q_{m+1}, \tag{2.54}$$

and express ρ_{m+1} as

$$\rho_{m+1} = \frac{((1-n) + \rho_m(1+n))}{((1+n) + \rho_m(1-n))}. \tag{2.55}$$

By equations (2.52) and (2.55) one can construct the solution for ρ everywhere once the LORE is known for a single value of s.

To determine such an initial value let us first consider a pure transmission problem.

In this case we get for a wave incident from the r.h.s. ($s \rightarrow +\infty$) of the barrier a transmitted wave on the l.h.s ($s \rightarrow -\infty$) $\psi = exp(-iks)t$ with a transmission matrix t. The logarithmic derivative on the l.h.s. then is $\lambda = -ik$, which leads to $\rho(-\infty) = 0$. Similarly for a pure reflection problem one may assume a very large and constant potential in the forbidden region leading to $\lambda = -iq$ and hence also to

$$\rho(-\infty) = 0, \tag{2.56}$$

which we will use as the general initial value.

So starting from (2.56) one applies (2.52) until the first step and then alternatively (2.55) and (2.52) until one reaches the region of constant potential in the entrance region. The LORE in this region is, apart from a phase factor and a kinematic factor, the physical reflection coefficient. The kinematic factor comes from the normalization of the plane waves to unit density. The fluxes in channel m therefore are proportional to k_m. Symmetrization leads to the unitary reflection coefficient of the asymptotic region

$$R_{mn} = \sqrt{k_m}\rho_{mn}\frac{1}{\sqrt{k_n}}. \tag{2.57}$$

Finally the quantity

$$P_{mn} = |R_{mn}|^2, \tag{2.58}$$

is the probability that a particle incident in an internal state n is reflected into an internal state m.

In a typical reaction on surfaces like dissociative adsorption the full scattering matrix U contains not only reflection but also transmission processes, which we will call sticking (described by the sticking coefficient S_{mn}), and desorption (described by desorption coefficient D_{mn}), which cannot be obtained directly from the LORE scheme. The sticking probability of a molecule on a surface can be determined from the whole matrices for sticking/desorption by

$$S_n(\epsilon) = 1 - \sum_n |R_{mn}|^2, \tag{2.59}$$

$S_n(\epsilon)$ is the sticking probability of a particle with an initial state n on the surface. The full scattering matrix can be written as

$$\mathbf{U} = \begin{pmatrix} L & S \\ D & R \end{pmatrix},$$

where the transmission matrices D and S cannot be determined from the LORE. In next step we also consider the inverse transmission matrix (INTRA).

II. Inverse transmission matrix without curvature

Since the pure reflection can be treated by LORE alone, we focus on the transmission case. In this case the solution of the Schrödinger equation (Eq. 2.44) for constant

q can be written as a sum of two terms proportional to $exp(\pm iqs)$. Now one makes the following ansatz for the wave function and its first derivative

$$\begin{aligned}\psi(s) &:= (1-\rho(s))\tau(s) \qquad (2.60)\\ \psi'(s) &:= -iq(s)(1+\rho(s))\tau(s), \qquad (2.61)\end{aligned}$$

where $\tau(s)$ is local transmission matrix.
The differential equations for local transmission matrix can now be derived from the Schrödinger equation

$$\tau'(s) = -iq(s)\tau(s) - \frac{1}{2q(s)}q'(s)(1+\rho(s))\tau(s). \qquad (2.62)$$

The boundary conditions for this equation are

$$\tau(-\infty) = t \qquad ; \qquad \tau(\infty) = 1. \qquad (2.63)$$

To produce a similar boundary condition for the local reflection matrix and local transmission matrix we introduce the quantity $t(s) = t/\tau(s)$ which may be called the inverse local transmission matrix (INTRA). Now the boundary values are

$$t(-\infty) = 1 \qquad ; \qquad t(\infty) = t. \qquad (2.64)$$

The differential equation for the INTRA can be easily written in term of $t(s)$ as

$$t'(s) = -iq(s)t(s) - \frac{t(s)}{2q(s)}q'(s)(1+\rho(s)), \qquad (2.65)$$

in this case for a piecewise constant potential the first term on the r.h.s. is also non-zero only on the plateaus and the second term only on the steps. Now with the same steps as a local reflection matrix, the local transmission matrix on the plateaus and step are

$$\begin{aligned}t_{m+1}(s) &= t_m e^{iq_m d} \qquad (2.66)\\ t_{m+1}(s) &= t_m e^{iq_m d}((n_m+1)+(n_m-1)\rho_{m+1})/2. \qquad (2.67)\end{aligned}$$

Unitary transmission matrix then can be obtained from the flux-normalized quantities

$$S_{mn} = \sqrt{k_m}t_{mn}\frac{1}{\sqrt{k_n}}. \qquad (2.68)$$

The full S-matrix can be obtained by combined INTRA-LORE solutions to study the sticking as well as scattering problems.

III. Reaction path with curvature

The dominant mechanisms for vibrational excitations in reactions is the change in bond length (described by a curvature $\kappa(s)$ of the reaction path) and in the frequency $\omega(s)$ of the vibrations perpendicular to the reaction path. Also a shift of the reaction path $b(s)$ should be taken into account. We will express this shift in terms of a dimensionless displacement function $u(x)$ and the vibrational zero point width $a(s) = \sqrt{\hbar/(\mu\omega(s))}$ (μ is the reduced mass)

$$b(s) = \int_{-\infty}^{s} a(x)u'(x)dx. \tag{2.69}$$

Instead of the original $\psi(r,s)$ (with a normal coordinate r which accounts for the vibrational degree of freedom) we introduce the function $\psi(\nu,s)$ with $\nu = (r-b(s))/a(s)$.

This generalization of the scheme involves some modification in the INTRA-LORE schemes which are derived in detail in Refs.[20–22]. We will present here just the final formulas. In this case the kinetic energy includes cross terms between the reaction path coordinate and the internal state coordinates, too. Now we have to distinguish in the partial derivative $\partial/\partial s$, the derivative ∂_s with respect to the explicit s, and ∂ with respect to the implicit s. Then the Schrödinger equation takes the form

$$(\partial_s + \partial)\eta^{-1}(\partial_s + \partial)\psi = \eta(V - k^2)\psi =: -q^2\frac{1}{\eta}\psi, \tag{2.70}$$

with $V = V_0 + \hbar\omega(n + 1/2) + \eta^{-1}\frac{\kappa}{a}\partial_\nu$ and coupling parameter $\eta(s) = 1 - \kappa(s)\rho$ (it should be noticed that ρ is perpendicular to the reaction path coordinate). We use the same indexing as in the preceding parts. The LORE and INTRA matrices on the plateaus are expressed by

$$\begin{aligned} \rho_m^+ &= e^{iq_m d}\rho_m^- e^{iq_m d} \\ t_m^+ &= t_m^- e^{iq_m d}, \end{aligned} \tag{2.71}$$

and on the step

$$\begin{aligned} \rho_{m+1} &= \frac{(\hat{n} - n) + \rho_m(\hat{n} + n)}{(\hat{n} + n) + \rho_m(\hat{n} - n)} \\ t_{m+1} &= t_m[(n + \hat{n}) + (n - \hat{n})\rho_{m+1}]/2, \end{aligned} \tag{2.72}$$

with the indices of reflection

$$n =: \frac{1}{q_m}e^{(c_m - c_{m+1})}q_{m+1} \;\; ; \;\; \hat{n} =: \frac{1}{\eta_m}e^{(c_m - c_{m+1})}\eta_{m+1}, \tag{2.73}$$

and

$$c_m = ln(a_m)\nu\partial_\nu + u_m\partial_\nu. \tag{2.74}$$

So, finally the only effect of the curvature is the occurrence of the two quantities n and $\hat{n}$ in (2.72).

2.3.3 The structure of computational simulation

The structure of the programme is based on the numerical coupled-channel method taking into account the symmetry property of the surface. In Fig. (2.6) the flow-chart of the coupled-channel simulation for the calculation of sticking probabilities is shown. The starting point is “read input parameters” which includes the parameterization of

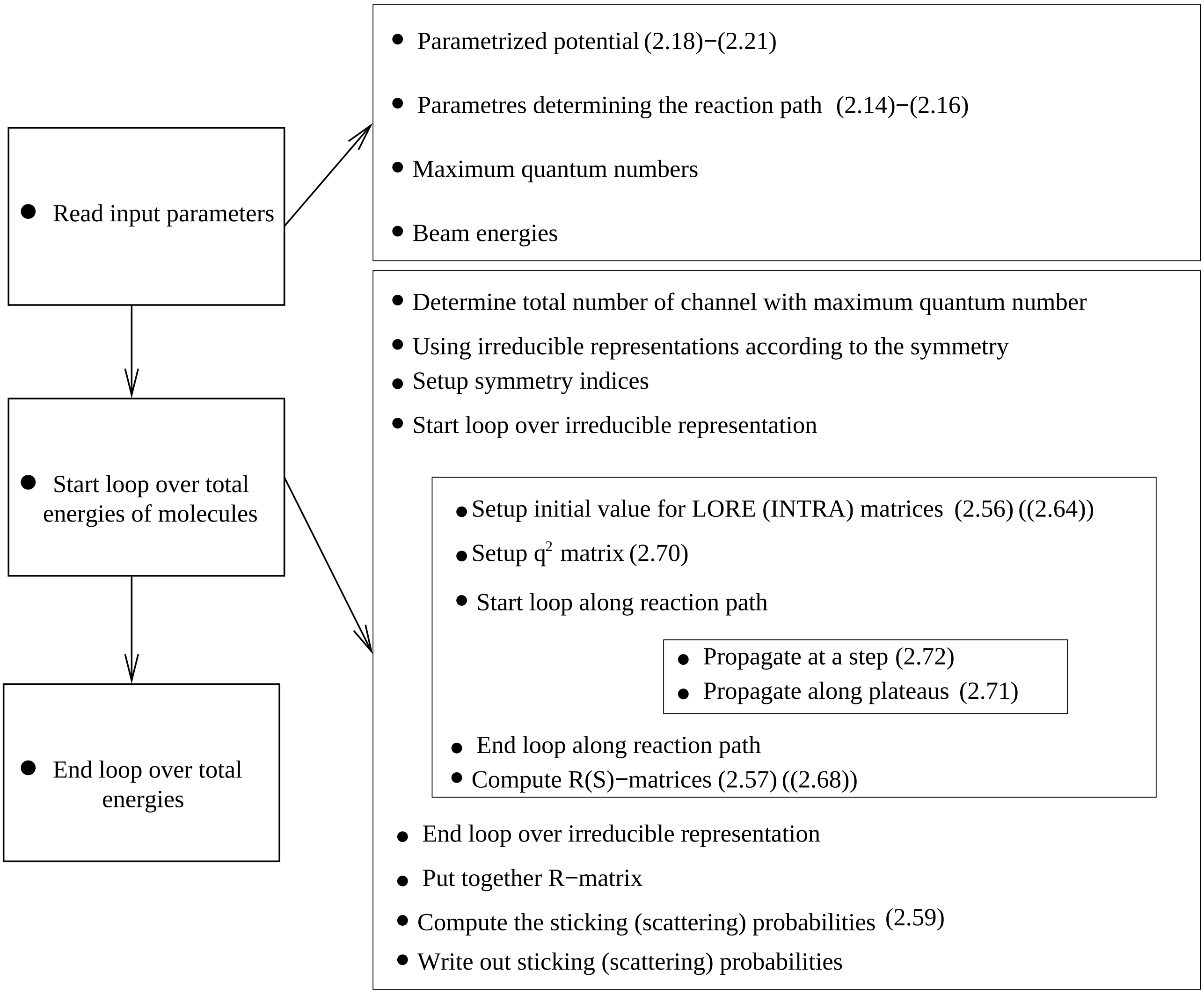
• Read input parameters
• Parametrized potential (2.18)−(2.21)
• Parametres determining the reaction path (2.14)−(2.16)
• Maximum quantum numbers
• Beam energies
• Start loop over total energies of molecules
• Determine total number of channel with maximum quantum number
• Using irreducible representations according to the symmetry
• Setup symmetry indices
• Start loop over irreducible representation
• Setup initial value for LORE (INTRA) matrices (2.56) ((2.64))
• Setup q2 matrix (2.70)
• Start loop along reaction path
• Propagate at a step (2.72)
• Propagate along plateaus (2.71)
• End loop along reaction path
• Compute R(S)−matrices (2.57) ((2.68))
• End loop over irreducible representation
• Put together R−matrix
• Compute the sticking (scattering) probabilities (2.59)
• Write out sticking (scattering) probabilities
• End loop over total energies

Figure 2.6: Flow-chart diagram of the coupled-channel computational simulation

the potential energy surface and the corresponding reaction path parameters, the choice of the maximum quantum numbers of wave function Eq. (2.32) (vibrational quantum number (ν), quantum numbers for parallel momentum (k_X , k_Y), polar and azimuthal rotational quantum numbers (l,m)) and the beam energies. Then the coupled-channels are solved as a function of the total energy. In this step, the channels are characterized by symmetry indices so that the channels with the same symmetry will not be taken into account in the calculation process. The local reflection matrix (inverse local transmission matrix) is determined within the irreducible representations of wave function. After putting together of R-matrices, in the last step the sticking probability (S matrix) or alternatively the scattering probability (R matrix) are written out.

Chapter 3

Rotational effects in adsorption of H_2/D_2 on Pd(100)

In this chapter we will discuss the influence of the rotational motion of small molecules on the dissociation dynamics using three- and five - dimensional simulations. In particular, we will focus on the effect of the change of the molecular bond length upon non-activated adsorption and desorption as well as the isotope effect.

3.1 Introduction

Hydrogen molecules interacting with a surface have been studied for a long time in surface science because of its technological importance, its chemical simplicity and the interest in quantum effects. The dynamics of the interacting particles is governed by the underlying potential energy surface (PES). However, the PES is not directly accessible by experiment. On the other hand, modern electronic structure methods provide a reliable tool to determine potential energy surfaces, but in order to make close contact to experiment, dynamical simulations have to be performed on the theoretically determined potentials [23]. Thus, dynamical studies are a decisive test of the accuracy of calculated potential energy surface

Insight into the dynamics of the adsorption process can be obtained by using molecular beam techniques to study the dependence of the adsorption probability on incident kinetic energy E_i, angle of incidence Θ_i, and initial quantum conditions of the beam [24]. For the time-reverse process, the desorption, state-specific detection of the desorbing molecules by laser techniques provides detailed information on the desorption dynamics [25, 26].

While the interaction of hydrogen with copper is a good candidate for activated adsorption, the H_2/Pd system is particularly interesting as an example of non-activated dissociation over a transition metal surface. The potential energy surface of the interaction of hydrogen with Pd(100) has non-activated paths towards dissociative adsorption and no molecular adsorption well. However, the majority of pathways towards dissociative adsorption has in fact energy barriers with a rather broad distribution of heights and positions, i.e. the PES is strongly anisotropic and corrugated [27].

A theoretical description of the dissociation dynamics of hydrogen on surfaces requires a quantum treatment due to the small mass of hydrogen. On the other hand, because of the large mass mismatch between hydrogen and the metal substrate atoms the energy transfer from hydrogen to the substrate atoms can usually be neglected [23, 28]. In the rotational excitation of H_2 scattered from Pd(111), a strong surface temperature dependence has been observed [29], but only at incident energies that are smaller than the energy necessary for the rotational excitation, i.e. for a situation in which the rotational excitation would be impossible without energy transfer from the surface. These findings have been confirmed in dynamical simulations in which the moving substrate was modeled by a single surface oscillator [30, 31]. Here we are not concerned with the rotational excitation in scattering but rather with the rotational effects in the dissociation on Pd(100) which is governed by the topology of the PES. In this context the surface phonons can be neglected.

The role of electronic excitations for the interaction of hydrogen with metal surfaces is still rather unclear. Although the excitation of electron-hole pairs at metal surfaces upon the adsorption of hydrogen has been observed [32], they usually correspond to a minority channel as far as inelastic effects in adsorption are concerned [33]. Hence it is also justified to neglect them for the purpose of the present study.

The sticking-coefficient S_0 as a function of the beam energy for hydrogen molecules impinging on Pd(100) has been measured by Rendulic *et al.* [24]. They found for low beam energies a decrease of S_0 with increasing beam energy up to about 0.25 eV from where on the sticking coefficient increases again. This behavior has been initially attributed to a precursor mechanism [34]. In this concept the molecules are temporarily trapped in a molecular physisorption state, the so called precursor, before they dissociatively adsorb. The energy dependence of S_0 is therefore related to the trapping probability into the precursor which decreases with increasing energy while the higher energy regime is dominated by direct adsorption. The dynamics of the interaction of H_2 with Pd(100) have been investigated in great detail in dynamical studies in which all six degrees of freedom of the hydrogen molecule were treated quantum dynamically [6, 8, 9]. These calculations have shown that an initial decrease of S_0 is not necessarily due to a precursor mechanism. On a PES which exhibits activated as well as non-activated pathways, slow molecules impinging in an unfavorable geometry can adapt their geometry in such away, that they enter non-activated pathways. This movement towards favorable adsorption pathways is called *steering*. Molecules with higher kinetic energy are too fast for this process and will be repelled. This results in a rather high sticking coefficient for low beam energies, which decreases with increasing energy. After a minimum in the sticking curve it increases again, indicating, that the kinetic energy is high enough to directly cross the barriers of the PES.

A similar effect is true for rotational excitation. Fast rotating molecules are less likely adsorbed than molecules in the ground state, since they do not steer in a geometry favorable for adsorption. Accordingly, the experimental result for dissociation of H_2 on Pd(111) indicates that the sticking probability initially decreases with increasing rotational quantum number. Due to detailed balance, desorbing molecules have therefore less rotational energy than expected for in equilibrium. This is called rotational cooling. However, the sticking probability of H_2/Pd(111) has been found to increase again for higher rotational quantum number [35]. Rotational cooling has been observed experimentally in desorption from Pd(100) [26]. Quantum dynamical calculations also predict a larger sticking probability for molecules with the rotational momentum $\mathbf{J}$ parallel to the surface normal $\hat{n}$ (helicopter rotation) compared to those with $\mathbf{J}$ perpendicular to $\hat{n}$ (cartwheel rotation). The degree to which the dissociation of molecules with helicoptering rotation is preferred over those with cartwheeling rotation is determined by the azimuthal corrugation of the dissociative potential. Thus, measuring the spatial alignment of the $\mathbf{J}$ of desorbing molecules yields a sensitive test of the anisotropy of the potential energy surface.

The experiments [36, 37] showed a non-monotonous behavior of the rotational alignment as a function of the rotational quantum number: first the rotational alignment increases, but for higher rotational quantum numbers it decreases again towards an almost isotropic rotational distribution [36, 37]. The high-dimensional quantum studies had been limited to rotational quantum numbers $j \leq 6$ because of high computing time for larger basis sets. However, non-monotonous behavior for rotational alignment has not been seen at low rotational quantum numbers in the six-dimensional quantum dynamics [8, 11, 38].

In this work we will study the cause of the non-monotonous behavior of the rotational alignment. On a three-dimensional potential energy surface, we are able to choose larger rotational quantum numbers for the rotational alignment calculation. For a better agreement between experiment and theory we have investigated the rotational alignment on five-dimensional potential energy surface including lateral coordinates.

3.2 Three-dimensional anisotropic potential

The six-dimensional potential energy surface of the dissociative adsorption of H_2 on Pd(100) has been calculated using *density functional theory* (DFT) within the *generalized gradient approximation* (GGA) and the full potential linear augmented plane-wave method[27]. The calculations indicate that the dissociation over the bridge and hollow site is non-activated while over the on-top site it is activated. For the two non-activated configurations, the potential energy is continually decreasing along the minimum energy path and the molecule can dissociate without any hindering barrier, while at the on-top position the molecule is first attracted towards an apparent local minimum before it hits a barrier. The six-dimensional PES has been parameterized by A. Groß et al. for a quantum dynamical simulation of the dissociation of H_2 on Pd(100) [6, 9].

For the reduced geometry employed here, the PES is based on the elbow plot (cut through the six-dimensional potential plotted as a function of molecular bond length and molecule-surface distance) for dissociation at the bridge site (most favorable pathway). A contour plot of this configuration is shown in Fig. 3.1.

However, in order to investigate the influence of the other degrees of freedom on

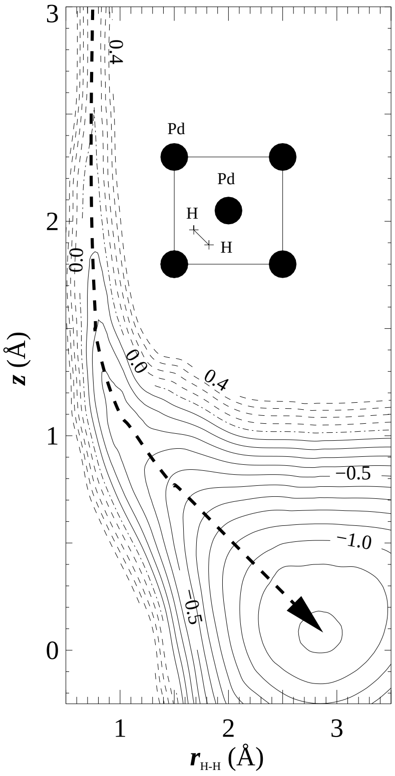

Figure 3.1: Two-dimensional cut through the six-dimensional potential energy surface of H_2/Pd(100) obtained by density functional calculations [27]. The coordinates in the figure are the H_2 center-of-mass distance from the surface z and the H-H interatomic distance r. Energies are in eV per H_2 molecule. The contour spacing is 0.1 eV. The lateral coordination and the orientation of the molecule are illustrated in the inset. The dashed line corresponds to the reaction path.

the dissociation dynamics, we have modified and simplified the dependence of the PES on the the orientation of the molecule.

The six-dimensional potential energy surface, suitable for the coupled-channel method is described in terms of two lateral coordinates (X, Y), two rotational coordinates (θ, ϕ) and two reaction path coordinates (s, ρ). If the molecular center of mass is fixed at the bridge site, the PES is reduced to four-dimensions

$$V(s, \rho, X, Y, \theta, \phi) \rightarrow V(s, \rho, \theta, \phi)|_{X=0,Y=0.5}. \tag{3.1}$$

It is possible to omit the perpendicular coordinate to the reaction path ρ using the vibrationally adiabatic approximation. We have assumed that the vibrations perpendicular to the reaction path coordinate s in the Zr-plane follow the motion adiabatically. This assumption has been studied in great detail by quantum dynamical calculation [10], in which the five-dimensional (vibrationally adiabatic) results are very close to the six-dimensional results. This can be understood from the fact that the vibrational coordinate corresponds to the fastest degree of freedom in the dissociation dynamics [39].

Then the PES reduces to the 3-dimensions

$$V(s,\rho,\theta,\phi) \rightarrow_{vibrationally\ \ adabatic} V(s,\theta,\phi). \tag{3.2}$$

First we want to study the rotational effects in the adsorption and desorption dynamics in fixed-site three-dimensional calculations. In this restricted geometry the PES is given in the following form

$$\begin{aligned} V(s,\theta,\phi) &= V_{reac}(s)\ +\ V_{vib}(s) \\ &\quad + V_{rot}(s)\ \cos^2\theta \\ &\quad + \frac{1}{2}\ V_{azi}(s)\ (1\ +\ \sin^2\theta\ \cos 2\phi)\ . \end{aligned} \tag{3.3}$$

Here $V_{reac}(s)$ is the potential along the minimum energy path, and $V_{rot}(s)$ and $V_{azi}(s)$ determine the anisotropy of the PES in the polar and azimuthal orientation, respectively. Their dependence on s is parameterized as

$$V_{reac}(s) \ = \ F\ (\tanh\lambda s - 1) \tag{3.4}$$

$$V_{rot}(s) \ = \ \frac{1}{2} V_{pol}\ (\ 1\ -\ \tanh\lambda s) \tag{3.5}$$

$$V_{azi}(s) \ = \ V_{azim}\ (\cosh\gamma\ (s - s_{azi}))^{-2}\ . \tag{3.6}$$

The constant F is related to the adsorption energy E_{ad} by $F = \frac{1}{2}E_{ad}$. The length scale of the minimum energy path is given by λ. The parameters V_{pol} and V_{azim} determine the maximum polar and azimuthal anisotropy.

Although we do not treat the molecular vibrations explicitly, we still take the change of the vibrational frequency along the reaction path into account via the term

$$V_{vib}(s) \ = \ \hbar\omega_{gas}\ \{1\ -\ n\ (1 - \tanh\gamma(s - s_{vib})\}. \tag{3.7}$$

The factor n gives the relative change of the vibrational frequency along the reaction path. This number $n = 0.38$ is actually the same as used in the six-dimensional quantum calculation [9], i.e., the vibrational frequency drops to 24% of its gas phase value along the reaction path. The parameters which are used in the three and five dimensional potential energy surfaces are listed in the table (3.1).

The three-dimensional Hamiltonian without curvature in the reaction path is given by

$$H_{3D} \ = \ -\frac{\hbar^2}{2M}\frac{\partial^2}{\partial s^2} + \frac{\hbar^2}{2\mu}\frac{\mathbf{L}^2}{r_e(s)^2}\ +\ V(s,\theta,\phi)\ , \tag{3.8}$$

where $\mathbf{L}$ is the angular momentum operator. M is the total mass of the hydrogen molecule, while μ is the reduced mass. $r_e(s)$ is the equilibrium hydrogen bond length along the reaction path. In the gas phase it is given by the hydrogen bond length 0.74 Å, but upon dissociative adsorption it increases up to 2.9 Å according to Fig. 3.1. This means that the moment of inertia $\mu r_e(s)^2$ also increases significantly along the

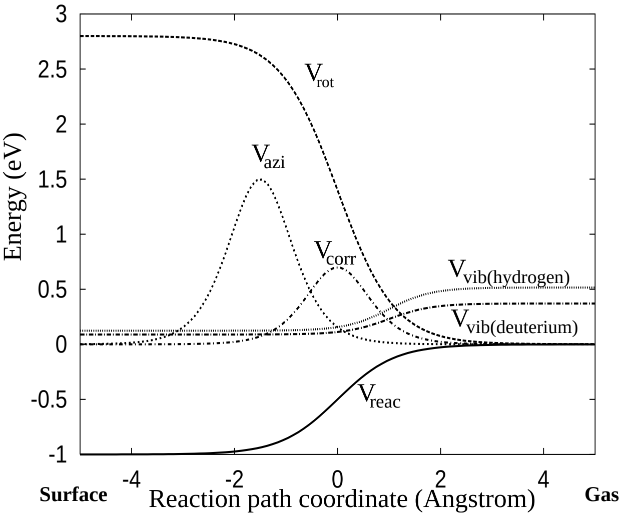

Figure 3.2: The functions $V_{reac}(s)$, $V_{rot}(s)$, $V_{azi}(s)$ and $V_{vib}(s)$ describing the most favorable reaction path and the anisotropy of the model potential energy surface used in the calculations.

reaction path, as defined in Eq. (2.16). The wave function is a superposition of spherical harmonics along the reaction path.

$$\Psi(s,\theta,\phi) = \sum_{jm} \Phi_{jm}(s) Y_{jm}(\theta,\phi). \tag{3.9}$$

Symmetry helps to reduce the computational effort of the calculation. Due to the inversion symmetry of the H_2 molecule only rotational transitions with Δj=even are allowed, where j is the rotational quantum number. In addition, we have used for the parameterization of the PES only rotational potential terms that cause Δm=even transitions, where m is the azimuthal quantum number of the H_2 molecule. This implies that there are four manifolds of differently excited molecules characterized by their quantum numbers j and m, which cannot mix up: j, m even; j, m odd; j even m odd; j odd m even. Within our three-dimensional calculations we have taken into account all four manifolds. The quantum dynamics is determined in a coupled-channel scheme within the concept of the local reflection matrix [LORE] [20]. Within this setup, the convergence of the results with respect to the basis set has been carefully checked. Calculations have been performed with a basis set consisting of rotational eigenfunctions with quantum numbers up to $j_{max} = 14$.

3.2.1 Rotational effects of H_2 and D_2 on an anisotropic surface

We have performed three-dimensional calculations of the sticking probability of hydrogen on Pd(100) for the center of mass of the hydrogen molecule fixed above the bridge site (see inset of Fig. 3.1). We investigate the two types of orientation of the molecule as a standard model to study rotational effects, namely the so-called cartwheel and

Table 3.1: Potential parameters used for the representation of the three-five dimensional model potential energy surface of H_2/Pd(100).

Reaction path parameters		
$s_0 = 2.5$	$r_0 = 1.2$	$\beta = 2.0$

Potential parameters (eV , Å, Å^{-1})				
$F = 0.5$	$\hbar\omega_{H_2(D_2)} = 0.516(0.371)$	$V_{pol} = 2.8$	$V_{azim} = 1.5$	$E_G = 0.7$
λ=0.9	γ=1.2	s_{azi}=-1.5	s_{vib}=1.0	$s_{barr} = 0.0$

helicopter rotation. The sticking probabilities of D_2 on Pd(100) are plotted in Fig. 3.3 as a function of the incident kinetic energy for different initial rotational states. The initial states in Fig. 3.3a) correspond to the cartwheel rotation for which the azimuthal quantum number is $m = 0$ whereas in Fig. 3.3b) results for initial helicopter rotation ($m = j$) are shown. Molecules rotating in the cartwheel fashion have their rotational axis preferentially oriented parallel to the surface so that they have a rather high probability hitting the surface in an upright fashion whereas for the helicoptering molecules the rotational axis is preferentially perpendicular to the surface. Note that the calculated sticking probabilities shown in Fig. 3.3 are larger than typical experimental values [24, 35, 40]. This is due to the restricted geometry of the 3D calculations in which the corrugation of the potential energy surface is not taken into account.

The steering effect [6] is operative at low energies for $j \leq 2$ in the cartwheel fashion, while in the helicopter fashion the steering effect occurs only for the rotationally ground state. At low energies, molecules impinging in an unfavorable configuration are redirected and reoriented by the anisotropy of the PES to non-activated pathways leading to the high sticking probability. This mechanism becomes less effective at higher kinetic energies where the molecules are too fast to be focused into favorable configurations towards dissociative adsorption. This causes the initial decrease in the sticking probability as a function of the kinetic energy. At even higher energies, the molecules have enough energy to directly cross the barriers, causing the sticking probability to rise again. The resonance structure in the sticking probability as a function of the kinetic energy is due to the opening up of new scattering channels [41–43].

Figure 3.3a) demonstrates that cartwheel rotation leads to a suppression of the sticking probability compared to the $j = 0$ non-rotating molecules. This behavior is well known as rotational hindering [44]: rotating molecules have a smaller probability to stick since they will rotate out of a favorable orientation during the adsorption process. Furthermore, molecules rotating in the cartwheel fashion have a high probability of hitting the surface in an upright fashion for which the PES is purely repulsive.

Rotational hindering is also present for the helicopter molecules with $m = j$. However, these molecules have their axis preferentially oriented parallel to the surface which is very favorable for dissociative adsorption. It means that molecules rotating in the helicopter fashion should dissociate more easily than molecules rotating in the cartwheel fashion. This steric effect overcomes the rotational hindering so that in fact the sticking probability increases for these molecules with increasing rotational quantum number j

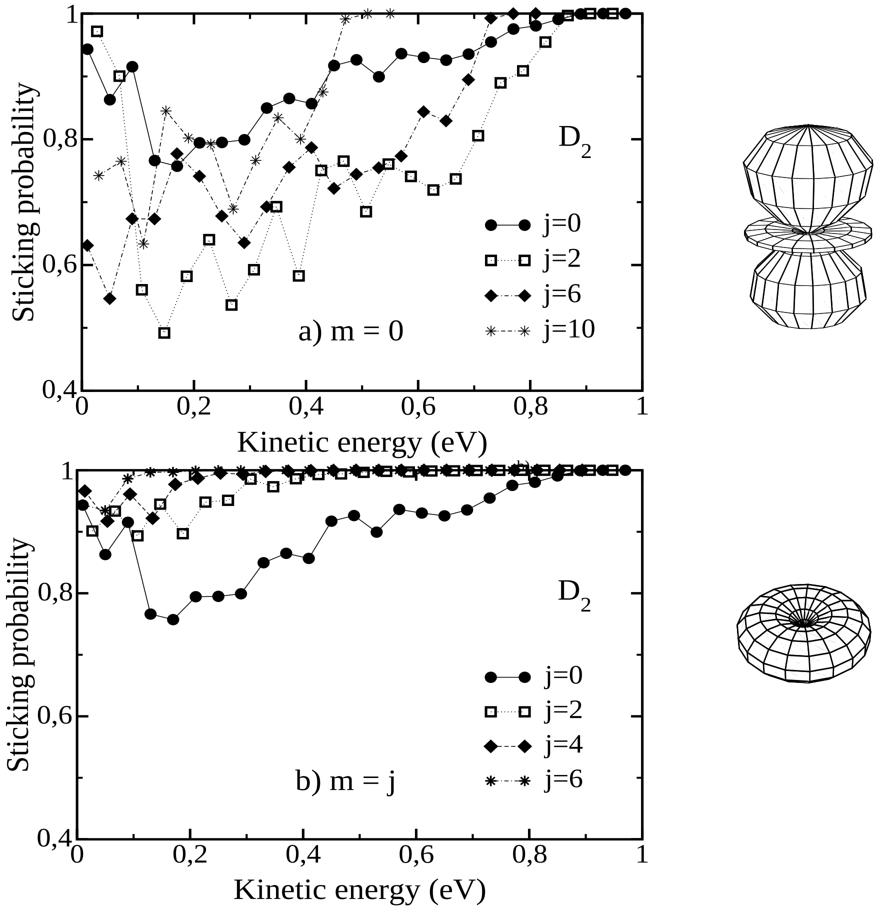

Figure 3.3: Three-dimensional calculation of the sticking probability of D_2 for a range of initial rotational states j as a function of the kinetic energy. a) Molecules initially rotating in the cartwheel fashion $m = 0$, b) molecules initially rotating in the helicopter fashion $m = j$. The initial wave functions for $j = 2$ in the cartwheel and helicopter fashion are plotted to show the preferred orientation of the molecular axis.

(see Fig. 3.3b) [6].

A closer look at Fig. 3.3a) indicates that the sticking probability is not monotonously decreasing with increasing j. Actually the sticking probability first decreases from $j = 0$ to $j = 2$ and then increases again for $j = 6$ and $j = 10$. Such a non-monotonous behavior has in fact been observed experimentally for D_2/Cu(111) [45] and H_2/Pd(111) [35]. Note that the experimental results have been derived for degeneracy averaged rotational states which means that they correspond to a sum over all azimuthal quantum numbers m. For kinetic energies smaller than 0.1 eV, the calculated degeneracy averaged sticking probabilities, which is plotted in Fig. 3.4), also exhibit a non-monotonous behavior with the minimum between j=4 and j=6 depending on the explicit energy. Since helicopter states usually do not show a clear non-monotonous dependence on the rotational quantum number (see Fig. 3.3(b)), this non-monotonous behavior in degeneracy averaged calculation must be due to states with $m < j$. According to the

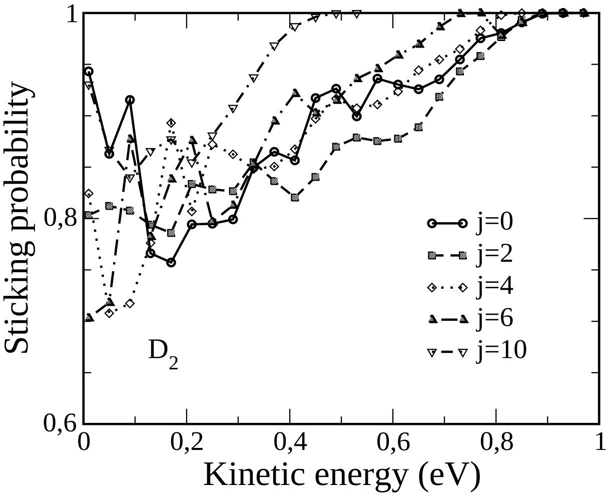

Figure 3.4: Three-dimensional calculation of the sticking probability of D_2 for a range of initial rotational states j as a function of the kinetic energy. Results are summed over the rotational degeneracy.

Ref. [44], which presents analogous 3D calculation of H_2/Cu(111), the m-dependence of the reaction probability for j=4 for azimuthally flat potential shows a decrease in the results having $m \leq 2$ and an increase in $m > 2$ results compared to the non-rotating molecules. At low energies, the degeneracy averaged sticking probabilities for $j < 10$ are smaller than the $j = 0$ results, so that there is still an overall rotational hindering, which is in qualitative agreement with the experiment for the H_2/Pd(111) system [35] where, however, only sticking probabilities for j up to $j = 5$ have been determined.

Steric effects in the rotational motion can also be observed for the time-reversed process of dissociative adsorption which is the associative desorption. Experimentally the so-called rotational alignment $A_0^{(2)}$ has been measured for hydrogen and deuterium desorbing from clean [36, 37, 46] and sulfur-covered Pd surfaces [47] by laser-induced florescence (LIF). The alignment parameters $A_0^{(k)}$ contain the complete dynamical information about the reaction product (or fragment). The $A_0^{(k)}$ correspond to the expectation values of the monopole, quadrupole and higher multipole moments of the angular momentum operators J

$$\begin{aligned} A_0^0 &= 1 \\ A_0^{(2)} &= \left\langle \frac{J_z^2 - J^2}{J^2} \right\rangle_j , \end{aligned} \tag{3.10}$$

where J_z is the z-component of the angular momentum operator J. The alignment parameters $A_0^{(2)}$ lie in the range

$$-1 \leq A_0^{(2)} \leq 2 \tag{3.11}$$

Molecules rotating preferentially in the cartwheel fashion have an alignment parameter $A_0^{(2)}(j) < 0$, while for molecules rotating preferentially in the helicopter fashion $A_0^{(2)}(j) > 0$.

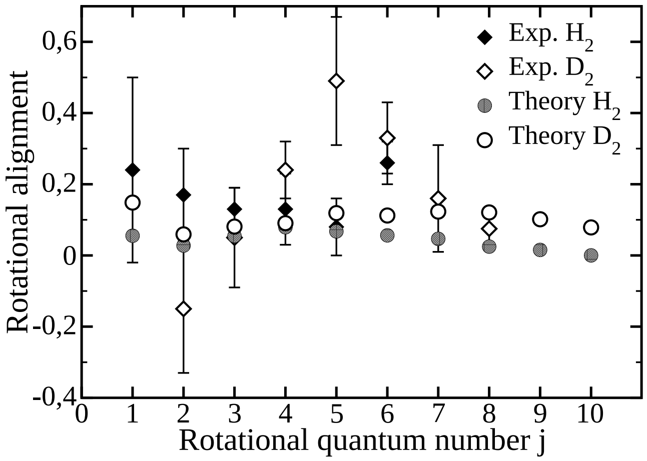

Figure 3.5: Rotational alignment of H_2 and D_2 molecules desorbing from Pd(100) at a surface temperature $T = 700K$. Diamonds correspond to the experimental results [36, 37] while three-dimensional quantum results are plotted as circles. Filled symbols: H_2, open symbols: D_2.

Theoretically, the rotational alignment in desorption can directly be evaluated from the state-specific sticking probabilities $S_n(E_\perp)$ where $E_\perp$ is the normal kinetic energy and n stands for a multi-index that describes the initial vibrational, rotational and parallel momentum state of the molecule. From these sticking probabilities vibrational and rotational distributions in desorption are derived via the principle of detailed balance or microscopic reversibility [10, 48, 49]. In detail, the population D_n of the state n in desorption at a surface temperature of T_s is given by

$$D_n(E_\perp) = \frac{1}{Z}\, S_n(E_\perp)\, e^{-\frac{E_n+E_\perp}{k_B T_s}} . \tag{3.12}$$

Here $E_\perp$ is the kinetic energy perpendicular to the surface, E_n is the energy associated with the internal state n, and Z is the partition sum that ensures the normalization of the distribution. To obtain the rotational alignment in desorption, the appropriate average over the probabilities D_n has to be performed. Since the substrate is kept fixed in the simulation, it does not participate dynamically in the adsorption/desorption process. Still it is assumed to act as a heat bath that determines the population distribution of the molecular states in desorption.

Experimentally the desorption of H_2 and D_2 from Pd(100) is characterized by positive alignment parameters showing a maximum around $j = 6$ [36, 37]. Six-dimensional quantum calculations of the rotational alignment so far had been limited to rotational quantum numbers $j \leq 6$ because of the high computational effort [11, 38]. In the present work, we have therefore extended these calculations to larger rotational quantum numbers in order to qualitatively understand the measured dependence of the alignment on the rotational quantum number j. In Fig. 3.5, the rotational alignment derived from our three-dimensional quantum calculations is compared with the experiment for a surface temperature of $T_s = 700$K. Our calculations show a non-monotonous behavior of the rotational alignment as a function of the rotational quantum number;

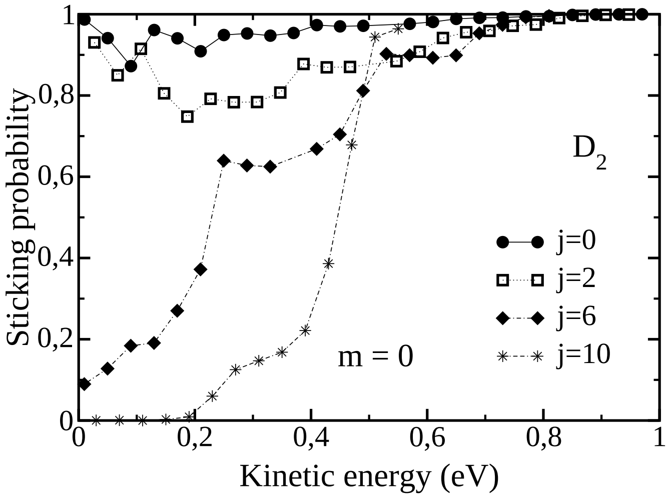

Figure 3.6: Three-dimensional calculation of the sticking probability of D_2 for a range of initial rotational states j as a function of the kinetic energy for molecules initially rotating in the cartwheel fashion $m = 0$. The D-D bond length and consequently the D_2 moment of inertia are kept frozen at their gas phase values.

hence the qualitative trend of the experiments is reproduced. The absolute values, however, are smaller than the experimental ones. This is caused by the low dimensionality of the calculations, as will become apparent later.

As far as the isotope effect between hydrogen and deuterium is concerned, the rotational alignment for H_2 is systematically smaller than for D_2. However, it is important to note that for a given rotational quantum number j the H_2 rotational energy is twice larger than the D_2 rotational energy since the H_2 moment of inertia is only half of the D_2 value (see Eq. (3.13)). Classically, there cannot be any isotope effect as a function of the energy if all masses in a system are scaled by the same amount [9, 50]. According to Groß et al. [9], at the same kinetic energy the classical equations of motion for an system with mass M_1 correspond to the equations of motion for a system with mass M_2 and rescaled time so that the trajectories remain exactly the same. Because of the different initial vibrational zero-point energies, the sticking probability of H_2 is larger compared to D_2 for six-dimensional quantum results. Due to the rather similar vibrational frequency of H_2 and D_2 in the adsorption regime, the apparent isotope effect of the theoretical results in Fig. 3.5 is almost entirely due to the different rotational energies associated with the rotational quantum numbers. Hence, the rotational alignments of H_2 and D_2 become rather similar if they are plotted as a function of the rotational energy.

The positive alignment of the desorbing hydrogen molecules is a consequence of the smaller azimuthal anisotropy of the PES compared to the polar anisotropy. For high rotational numbers, however, the difference in the sticking probabilities between cartwheel and helicopter molecules is rather small because of the adiabatic rotational-translational energy transfer. Hence it seems obvious that this adiabatic effect is also responsible for the non-monotonous behavior of the rotational alignment. The non-

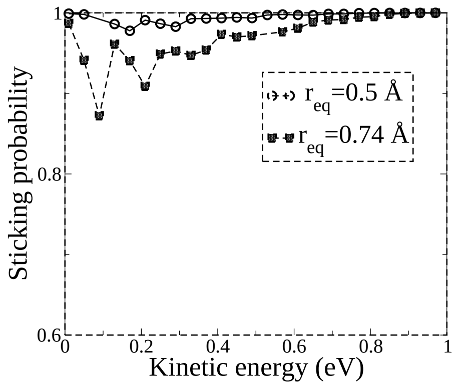

Figure 3.7: Three-dimensional quantum results of the sticking probability of hydrogen molecules on Pd(100). The hydrogen bond length kept fixed at 0.5 Å and 0.74Å values.

monotonic behavior of the j-dependence of the sticking probability in the cartwheel fashion and alternatively for the rotational alignment have been explained by the competition between the rotational hindering and an opposing adiabatic effect due to the extension of the hydrogen bond length upon dissociation [44]. Along the reaction path, the bond length $r_e(s)$ is stretched and thus the moment of inertia $I = \mu r_e^2(s)$ increases. Consequently, the rotational energy

$$E_{rot}(j) = \frac{\hbar^2 j(j+1)}{2I} \tag{3.13}$$

associated with the rotational state decreases. Assuming that the dissociation occurs rotationally adiabatic, i.e., without any change in the rotational quantum state, this would correspond to an effective energy transfer from the rotation to the translation which increases with the rotational quantum number. If the bond is not extend at the barrier, there can be no rotational enhancement by cartwheel fashion. Now the dissociation is certainly not rotationally adiabatic because of the strong θ and ϕ dependence in the potential energy surface.

3.2.2 Rotational effect with frozen bond length

In order to check whether this picture of the adiabatic energy transfer still approximately holds, we repeated the three-dimensional calculations using exactly the same potential except for the moment of inertia that we kept fixed at its gas phase value. The results of these calculations are shown in Fig. 3.6 for D_2 molecules initially rotating in the cartwheel fashion. In fact, now there is a general monotonous dependence of the sticking probability on the rotational quantum number j. Increasing the initial rotational quantum number suppresses the sticking probability so that we have the case of pure rotational hindering. This confirms that it is indeed the adiabatic rotational-translational energy transfer that is responsible for the non-monotonous behavior of the sticking probability as a function of the rotational quantum number observed in experiment.

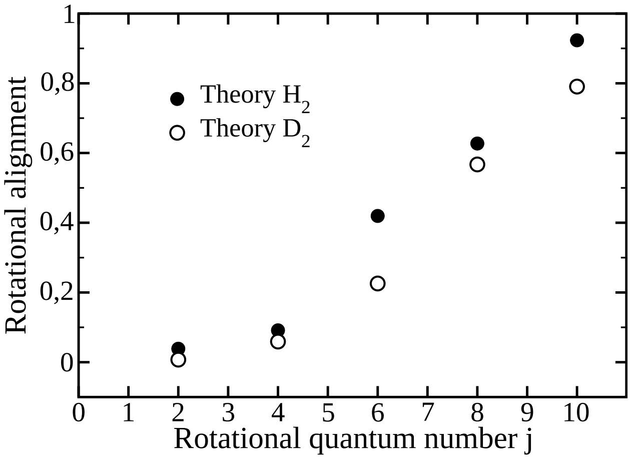

Figure 3.8: Three-dimensional quantum results of the rotational alignment of hydrogen molecules desorbing from Pd(100) at a surface temperature $T_s = 700$ K with the hydrogen bond length and moment of inertia kept fixed at their gas phase values.

While for $j = 6$ and $j = 10$ the sticking probability is strongly reduced if no change of the bond length is taken into account, for $j = 0$ and $j = 2$ the sticking probability is in fact increased compared to the case with variable bond length. This is at first sight particularly surprising for the non-rotating $j = 0$ state where one would expect no effects due to a modification of the bond length. However, a $j = 0$ state is spherical isotropic, i.e., it contains all orientations with equal weight. Since molecules with an upright orientation cannot dissociate, they have to be re-oriented before dissociation. Actually the forces can reorient the molecule into a favorable orientation for dissociation. This effect is similar to the steering effect and corresponds to the excitation of rotational motion. Quantum mechanically one would expect that for a smaller moment of inertia this excitation is suppressed since the quantum of rotational energy $E_{rot}(j)$ (Eq. 3.13) becomes larger. Rotational hindering dominates and the sticking coefficient should be decreased for the smaller bond length. Classically, on the other hand, it is easier to re-orient an object with a smaller moment of inertia since the energy associated with a rotation with frequency ω, $E^{cl}_{rot} = I\omega^2$, is proportional to the moment of inertia. In order to further confirm this view we calculated the sticking probability for hydrogen molecules with a smaller constant hypothetical bond length of 0.5 Å (see Fig. 3.7). Indeed we found that the sticking probability for molecules in the $j = 0$ state increases even further compared to the bond length of 0.74 Å. Apparently for the re-orientation of hydrogen molecules upon dissociative adsorption the classical picture is more appropriate.

In addition, we have determined the rotational alignment in desorption for molecules with a constant moment of inertia. And indeed, under these conditions the rotational alignment is monotonously rising, as Fig. 3.8 demonstrates. This confirms that it is the change of moment of inertia which causes the non-monotonous behavior of the rotational alignment.

3.3 Five-dimensional corrugated potential

The next logical step is to account for the corrugation of the surface. In order to have a more realistic description of the hydrogen dissociation dynamics on Pd(100) we have extended our calculations and also taken the lateral degrees of freedom of the molecule into account. Although the consideration of a low-dimensional PES to understand and interpret the dynamics is very important, the comparison of theoretical results with experiment often requires high-dimensional simulations. Actually, for the five-dimensional potential we have also simplified the parameterization of the full-dimensional potential for H_2/Pd(100) [6, 9]. The five-dimensional potential energy surface including corrugation which satisfies the symmetry of the surface is given by

$$\begin{aligned} V(s,\theta,\phi,X,Y) &= V_{reac}(s) \; + \; V_{vib}(s) \\ &+ \; V_{rot}(s) \; \cos^2\theta \\ &+ \; \frac{1}{4} V_{azi}(s) \; (2+\sin^2\theta\cos 2\phi) \; (\cos GX - \cos GY) \\ &+ \; \frac{1}{4} V_{corr}(s) \; (2+\cos GX + \cos GY) \; , \end{aligned} \tag{3.14}$$

where a is the lattice constant and $G = 2\pi/a$ corresponds to the lattice constant of the reciprocal lattice. For V_{reac}, V_{rot} and V_{azi} we have taken exactly the same parameterization as in the three-dimensional calculations. Because of the symmetry properties of the surface, the two $(0.0, 0.5, 90°, 90°)$ and $(0.5, 0.0, 90°, 0.0°)$ configurations are equivalent, and therefore, the coupling between anisotropy and corrugation should be taken into account. The corrugation term V_{corr} is parameterized according to

$$V_{corr}(s) \; = \; E_G \; (\cosh\gamma(s - s_{barr}))^{-2}. \tag{3.15}$$

Here $E_G = 0.7$ eV is the energetic corrugation amplitude and $s_{barr} = 0.0$ the position of the barrier. The position of the barrier does not depend on the lateral coordinates. This implies that we only take energetic corrugation into account and no geometrical corrugation [51, 52]. The reaction path dependence of the corrugation has been plotted in Fig. 3.2 in comparison with the other parameters.

The five-dimensional Hamiltonian is then given by

$$\begin{aligned} H_{5D} \;\; &= \;\; -\frac{\hbar^2}{2M} \left(\frac{\partial^2}{\partial s^2} + \frac{\partial^2}{\partial X^2} + \frac{\partial^2}{\partial Y^2} \right) \\ &\quad + \frac{\hbar^2}{2\mu} \, \frac{\mathbf{L}^2}{r_e(s)^2} \; + \; V(s,\theta,\phi,X,Y) \; . \end{aligned} \tag{3.16}$$

Now, in this case we have to additionally consider the basis wave function which describes the lateral motion of molecule. The five-dimensional wave function is expressed by

$$\Psi(s,\theta,\phi,X,Y) = \sum_{i,k,j,m} \Phi_{i,k,j,m}(s) e^{(\mathbf{G_{ik}}+\mathbf{K})\cdot\mathbf{R}} Y_{jm}(\theta,\phi). \tag{3.17}$$

The lateral and reciprocal lattice coordinates are defined in Eq. (2.32). Since the

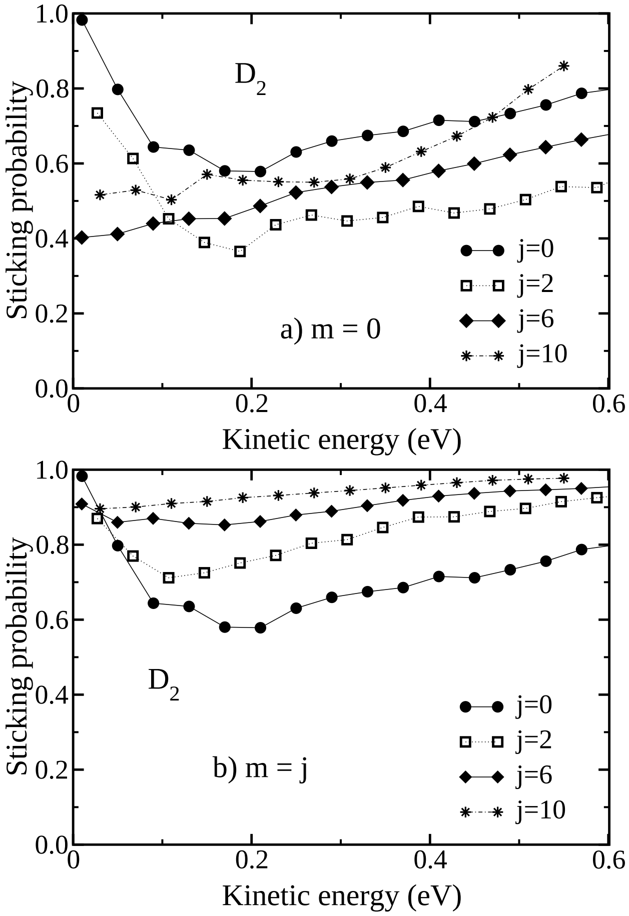

Figure 3.9: Five-dimensional calculation of the sticking probability of D_2 for a range of initial rotational states j as a function of the kinetic energy under normal incidence. a) Molecules initially rotating in the cartwheel fashion $m = 0$, b) molecules initially rotating in the helicopter fashion $m = j$.

computational demand of the five-dimensional calculation is already rather large, we have just taken into account the manifold with j, m even, as is contains also the ground state $j = m = 0$. The basis set used in the coupled-channel algorithm included rotational quantum numbers up to $j_{max} = 10$ and a maximum parallel momentum of $p_{max} = 8\hbar G$. The convergence of the results with this basis function has been carefully checked.

3.3.1 Rotational effect of H_2 and D_2 on corrugated surface

We have performed five-dimensional vibrationally adiabatic quantum calculations of the dissociation of hydrogen using the potential (3.14). The 5D quantum results of the sticking probability for D_2 are plotted in Fig. 3.9. Note the different scale compared to Fig. 3.3. Due to the additional corrugation the sticking probability in general is lower compared to the three-dimensional calculations. The qualitative trends in the

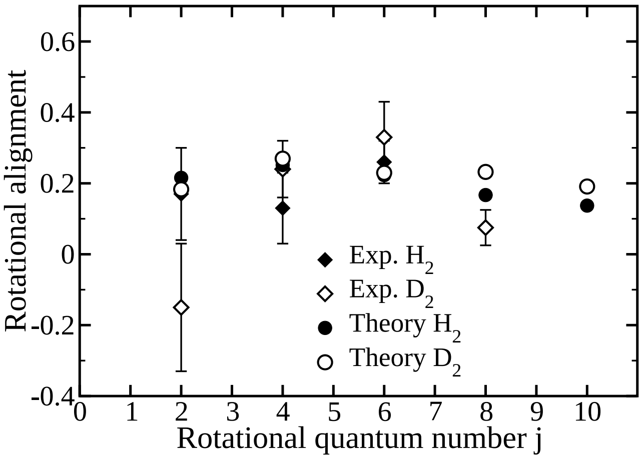

Figure 3.10: Comparison of the rotational alignment of H_2 and D_2 molecules desorbing from Pd(100) at a surface temperature $T = 700K$ derived from five-dimensional quantum calculations (circles) with the experimental results [36, 37] (diamonds). Filled symbols: H_2, open symbols: D_2.

dependence of the sticking probability on the initial rotational state, however, are the same as in the three-dimensional calculations. For cartwheel molecules the sticking probability shows a non-monotonous behavior as a function of the rotational quantum number j with the minimum for $j = 2$, while for the helicopter molecules the sticking probability rises with increasing j. Consequently, all the conclusions for the dependence of the sticking probability on the rotational state derived in the context of the three-dimensional calculations remain valid.

Furthermore, we have also determined the rotational alignment in H_2 and D_2 desorption from Pd(100) according to the five-dimensional quantum calculations. Since we have been taken into account only transition probabilities for the manifold of even rotational and azimuthal quantum numbers, there are no alignment results for the odd rotational numbers avaliable. In addition, the rotational alignments shown in Fig. 3.10 correspond to an average over only even m. The error associated with this approximation, however, is rather small [38].

Fig. 3.10 shows that the non-monotonous behavior of the calculated rotational alignment is still reproduced, but the absolute values of the alignment are larger by a factor of about two compared to the three-dimensional calculations. The calculated values now agree satisfactorily with the experimental results. In fact, if we do not include the corrugation term in the 5D calculations, i.e. if we set $E_G = 0$, then the rotational alignment is very similar to the 3D case (see Fig. 3.11). Only when we include the rotationally isotropic corrugation V_{corr}, the rotational alignment is increased by about a factor of two. This is indeed very surprising since the anisotropy of the potential energy surface is not changed by the inclusion of the term V_{corr}.

This unexpected behavior can in fact easily be understood by considering that the rotational alignment basically depends on the ratio of the desorption probabilities between helicopter and cartwheel molecules. Taking into account the corrugation

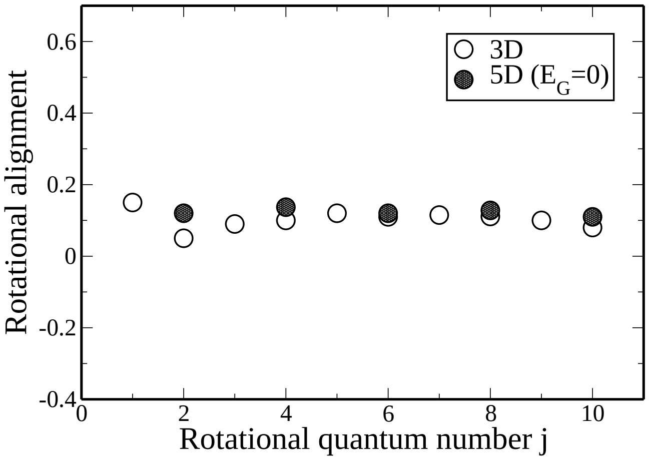

Figure 3.11: Comparison of the rotational alignment of D_2 molecules desorbing from Pd(100) at a surface temperature $T = 700K$ derived from five-dimensional quantum calculations without corrugation term $E_G = 0$ (filled circles) with the three-dimensional results (open circles).

term V_{corr} leads to a decrease in the adsorption and desorption probabilities that is to first order independent of the rotational state. This constant downshift, on the other hand, increases the ratio between the reaction probabilities of helicopter and cartwheel molecules, thus increasing the rotational alignment.

Chapter 4

Six-dimensional quantum dynamics of H_2 on Pd(110)

In this chapter we will first study the six-dimensional quantum dynamics of the dissociative adsorption of H_2 on Pd(110). We will focus on the influence of the rotational initial conditions as well as the angle of incidence on the reaction probabilities. We will also discuss the scattering of H_2 from the Pd(110) surface.

4.1 Dissociative adsorption of H_2 on Pd(110)

4.1.1 Introduction

Understanding H_2 adsorption and dissociation on low index metal surfaces is the first step toward the modeling of more complex catalytic reactions on surfaces. The dynamics of H_2 on metal surfaces have been studied in the last years, both experimentally [24, 26, 34, 35, 37, 40, 46, 53–57] as well as theoretically [6, 9, 16, 23, 28, 44, 51, 58–68]. Like most other transition metals palladium can be used as a catalyst for hydrogenation and dehydrogenation. Due to the high rate of permeation for hydrogen through palladium samples, the interaction between hydrogen and palladium is especially interesting.

The theoretical description of quantum dynamical studies in which all six degrees of freedom of the H_2 molecule are explicitly included have been performed for the low-index (100) and (111) surfaces [6, 9, 19, 59, 65, 67], since their high symmetry allows a considerable reduction of the computational effort by using symmetry-adapted wave functions [9, 69, 70]. Due to the relatively low symmetry of the fcc(110) structure, a large number of channels has to be taken into account, resulting in large computational requirements.

In this work, we report a six-dimensional quantum dynamical study of H_2 dissociation on a (110) surface, namely for the system H_2/Pd(110). This choice is mainly motivated by the fact that sticking coefficients were measured experimentally by molecular beam experiments for H_2/Pd(110), allowing for a direct comparison with experiment [71]. With this investigation we are able to see the possible differences in adsorption dynamics on a more corrugated surface Pd(110) with respect to Pd(100) and Pd(111). The potential energy surface (PES) used in our study has been derived from first-principles electronic structure calculations based on density functional theory (DFT) within the generalized gradient approximation [72], and the dynamical calculations have been carried out employing a computationally very efficient coupled-channel scheme [20, 21].

Recent studies for H_2/Pd(111) have proposed still another interpretation for the non-monotonous behavior of the sticking probability based on dynamical trapping [17, 66, 67]. Impinging molecules are, first, attracted by the surface and reach a region where the anisotropy and corrugation of the PES produce an energy transfer from translation perpendicular to the surface into other molecular degrees of freedom, mainly rotation. If too much kinetic energy normal to the surface has been lost, they are unable to go back into vacuum. Therefore, they remain temporarily trapped near the surface which favors dissociation. Eventually most of the dynamically trapped molecules dissociate. The dissociative adsorption of H_2/Pd(110) for normal incidence has been studied by classical and quasiclassical molecular dynamics simulations [68]. In these calculations, a PES has been employed that was adjusted to DFT calculations in a corrugation-reducing scheme (see Sec. 2.2) [73]. This study mainly focused on the role of dynamic trapping. According to their quasiclassical calculations, the sticking probability takes a minimum value of about 0.7 at an incidence energy of 150 meV. The calculated sticking probabilities are in good agreement with the ones determined by us, regarding the different methods used in both studies.

We have in particular focused on the effects of the corrugation and anisotropy of the PES on the H_2 dissociation probability. The topological variation in each dimension manifests itself as a particular observable due to the corresponding dynamical variable. For instance, the dependence of the dissociation barrier on molecular orientation will appear as a rotational effect in the dissociation, or the surface corrugation (energetic or geometric)will be reflected in the sticking probability as a function of the angle of incidence. The (110) surface exhibits a rather open structure with troughs running along the $[1\bar{1}0]$ direction. Our results agree well with the available experimental data for the sticking probability as a function of the initial kinetic energy and the angle of incidence. We have further analyzed the influence of the initial rotational state characterized by the rotational quantum numbers j and m. We have found some well-known effects such as the *steering* effect at low energies beam and the *rotational hindering* effect in the cartwheel fashion as explained in previous chapter. However, we found a surprisingly large rotational enhancement of the dissociation probability if the preferential orientation of the molecular axis is slightly further off from the perpendicular orientation, i.e., for $m > 0$. We attribute this to the strong coupling between the corrugation and anisotropy of the potential energy surface. Based on these findings, we predict an unusual rotational heating and a rather small rotational

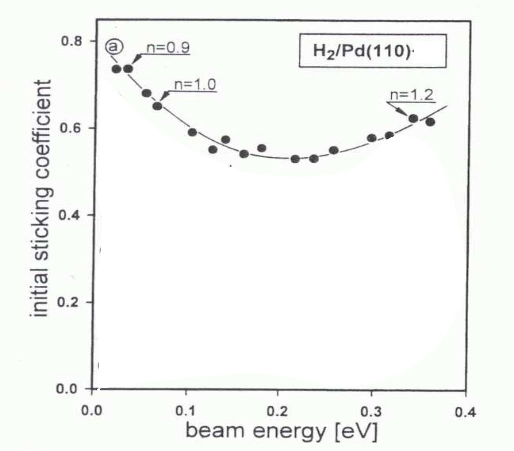

Figure 4.1: Initial sticking coefficient as a function of beam energy has been reported by experimental measurement [71]. The values n describe the angular variation of the sticking coefficient through the approximation $S(\theta)\cos(\theta) \sim \cos^n(\theta)$.

alignment in desorption. For non-normal incidence, we find a strong deviation from normal-energy scaling which also depends on the azimuthal angle of incidence.

After this introduction we first explain the experimental situation of H_2 on Pd(110), then we will describe the construction of the potential energy surface and the computational details of the quantum dynamical calculations. After that we will discuss the influence of the kinetic energy, rotational state and angle of incidence on the dissociation dynamics.

4.1.2 Experimental situation

Ch. Resch *et al.* measured the energy dependence and the angular variation of the initial sticking coefficient for a monoenergetic nozzle beam of hydrogen interacting with Pd(111) and Pd(110) [71]. The initial sticking coefficient is shown as a function of beam energy for H_2/Pd(110) in Fig. 4.1. According to Resch *et al.* at low beam energies a decrease of the sticking coefficient up to about 0.2 eV occurs due to precursor mediated adsorption while at high beam energies the sticking coefficient increases due to an activation barrier in the dissociative chemisorption. The exponent n of the approximation $S(\theta)\cos(\theta) \sim \cos^n(\theta)$ has been entered for a number of different beam energies. At low energies total energy scaling is observed with exponents n of the order of unity. The sticking coefficient as a function of angle of incident could be obtained, for example at 0.35 eV, through the relation $S = S_0 \cos^{0.2}(\theta)$ which we have used for comparison with our theoretical results. It should be noted that the sticking coefficient for H_2/Pd(110) is larger than for H_2/Pd(100) and H_2/Pd(111).

In molecular beam experiments, supersonic beams of molecules are directed at the surface of interest. These beams are formed by the rapid expansion of a gas flowing through a nozzle which leads to translational energy distributions that are considerably narrower than those of thermal beams [34]. The mean translational energy is primarily controlled by choosing the temperature T_N of the nozzle through which the molecules emerge. This has the unwanted side-effect of changing the populations of the initial ro-vibrational states, which are usually given by a Boltzmann distribution according to some effective temperature. Thus many plots of S(E) are actually $S(T_N)$ curves. These are only the same when vibration and rotation have no influence on the dissociation. According to the our theoretical calculations, the dissociation probability strongly depends on the rotational state, therefore, we have also included the $S(T_N)$ results in our theoretical calculation.

4.1.3 Parameterization of *ab initio* results and QMD

In order to perform the quantum dynamical simulations, we need a continuous analytical form of the potential energy surface. Consequently, the first step is the parameterization of the *ab initio* PES as a function of the six coordinates of the H_2 molecule using a suitable analytical form. These six coordinates were defined in the previous chapters. The metal substrate is kept fixed in the quantum dynamical simulations. The dissociative adsorption of a hydrogen molecule on the Pd(110) surface has been studied by *ab initio* total energy calculations [72]. These calculations are based on density functional theory (DFT) together with the generalized gradient approximation (GGA), using a plane wave basis and ultra-soft pseudo-potentials as reported by Ledentu *et al.* The configurations studied in the *ab initio* calculations are shown in Fig. 4.2. The reaction pathways are characterized by a specified position of the center of mass and the chosen orientation of H_2. According to the *ab initio* results, pathways (1) and (6) are unactivated pathways while the other pathways correspond to activated dissociation of H_2 molecules.

The parameterization of the potential energy surface has been obtained through the following functional form which is adapted to the symmetry of a fcc(110) structure

$$\begin{aligned} V^{corr}(s,X,Y) &= V_0^c(s) + V_1^c(s)\cos G_X X + V_2^c(s)\cos G_Y Y \\ &\quad +V_3^c(s)\cos G_X X\cos G_Y Y \end{aligned} \tag{4.1}$$

$$\begin{aligned} V^{rot}(s,X,Y,\theta,\phi) &= V_0^r(s)\cos^2\theta + [V_1^r(s)\cos G_X X + V_2^r(s)\cos G_Y Y \\ &\quad + V_3^r(s)\cos G_X X\cos G_Y Y]\sin^2\theta\cos(2\phi) \end{aligned} \tag{4.2}$$

$$V^{vib}(s,\rho) = \frac{\mu}{2}\omega^2(s)[\rho - \Delta\rho(s,X,Y)]^2. \tag{4.3}$$

In order to determine the parameters of this analytical form with the reaction path functions as defined in the Eq. (2.23), the PES is constructed by considering two polar orientations of the molecular axis, parallel (θ= 90°) and perpendicular (θ= 0°) to the surface. For the parallel geometry, we have used the published H_2/Pd(110) elbow plots obtained in DFT calculations by Ledentu *et al.* [72]. Unfortunately, no *ab initio* data for the perpendicular H_2 orientation on Pd(110) was available. Assuming that the polar anisotropy of the H_2/Pd PES does not vary significantly between different low-index Pd surfaces, we have used the laterally independent polar anisotropy calculated

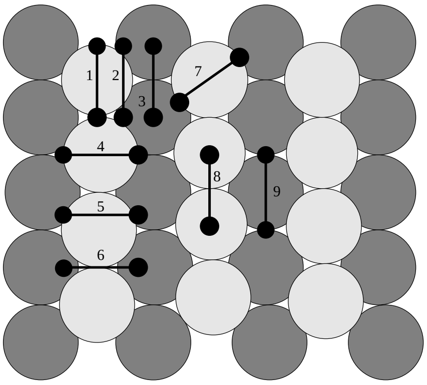

Figure 4.2: The different reaction paths of the Pd(110) used in *ab initio* calculations: (1) short bridge-top-short bridge (sb-top-sb); (2) pseudo-three-fold-pseudo-three-fold (p3f-p3f); (3) hollow-long bridge-hollow (h-lb-h); (4) long bridge-top-long bridge (lb-top-lb); (5) near long bridge-top-long bridge (near lb-top-lb); (6) pseudo-three-fold-short bridge-pseudo-three-fold (p3f-sb-p3f); (7)pseudo-three-fold-top-pseudo-three-fold (p3f-top-p3f); (8) top-short bridge-top (top-sb-top); (9) long bridge-hollow-long bridge (lb-h-lb).

for the H_2/Pd(100) system [9, 27]. The direction corresponding to $\phi= 0°$ is associated with the molecular axis of H_2 aligned along the [10] or x direction. Out of the nine published elbow plots we have used six to adjust the parameters in our interpolation scheme. The remaining three elbow plots have served as test examples.

In Fig. 4.3a and b, two elbow plots are shown which are in fact derived from the analytical fit to the *ab initio* PES [72]. In the insets of Fig. 4.3a & b, the coordinate axes of the surface unit cell are defined. In the following, we will denote by [10] or x the $[1\bar{1}0]$ direction and by [01] or y the [001] direction. In the fit, we have mainly tried to obtain an accurate representation of the PES close to the transition states since these regions are crucial for the dissociation dynamics. As far as the transition state energies of the adsorption paths determined by Ledentu *et al.* [72] are concerned, the mean difference between the *ab initio* results and the interpolation is around 50 meV (see table 4.1). Generally, the deviation is about 100 meV on the average.

Two parameterized elbow potentials are shown in Fig. 4.3a & b for the H_2 molecule above the so-called short-bridge and long-bridge position, respectively, with its molecular axis parallel to the surface and perpendicular to the bridge axes. Fig. 4.3a corresponds to the most favorable reaction route along which H_2 molecules can spontaneously dissociate. It smoothly leads from the molecule in the gas phase to the dissociated atoms on the surface. Note that the regions of the elbow plot for H-H distances above approximately 2.0 Å which are not crucial for the dissociation dynamics have been fitted with less accuracy. At the long-bridge position (Fig. 4.3b), the dissociation is no longer non-activated, and there is a shallow minimum before the barrier which is, however, only about 100 meV deep. Furthermore, the minimum energy path bends much more sharply compared to the short-bridge position. It is important to note that the PES of H_2 on Pd(110) consists of a combination of non-activated and activated paths to dissociative adsorption. In order to compare the barrier heights and

Table 4.1: Energies and geometries of transition states. The mean difference between *ab initio* results and the parameterized fitting is around 50 meV.

Pathway	Z(Å)	r(Å)	$E_{abinitio}$(eV)	$E_{fitting}$(eV)
(1) sb-top-sb	1.42	1.42	-0.032	-0.051
(2) p3f-p3f	1.03	1.32	0.013	0.13
(3) h-lb-h	0.63	0.87	0.081	0.075
(4) lb-top-lb	0.99	2.49	0.178	0.28
(5) near lb-top-lb	2.20	1.52	0.108	0.151
(6) p3f-sb-p3f	1.14	0.94	-0.160	-0.150
(7) p3f-top-p3f	1.36	1.60	0.035	0.065
(8) top-sb-top	1.49	1.98	0.208	0.252
(9) lb-h-lb	0.75	0.84	0.311	0.347

positions for different reaction pathways, we have also plotted the PES as a function of the reaction path in Fig. 4.3c for different reaction paths. In fact along the [001] or y direction, for example pathways 1,2,3, the barrier positions vary for each configuration (geometric corrugation), while along the $[1\bar{1}0]$ or x direction, for example pathways 4,5,6, the barrier positions are located at approximately the same reaction path coordinate (energetic corrugation).

Our parameterization which is adjusted to *ab initio* calculations at high-symmetry points represents an assumption about the form of the PES at low-symmetry configurations which is not necessarily correct. However, in the absence of *ab initio* calculations for low-symmetry configurations it is not possible to judge the reliability of this interpolation. Using the parameterization of the *ab initio* PES, the time-independent Schrödinger equation for the two hydrogen nuclei moving on the six-dimensional PES (see Eq. 2.33) has been solved by coupled-channel calculations using the concept of the *local reflection matrix* (LORE) and the *inverse local transmission matrix* (INTRA)[20, 21]. As usual, the H_2 dissociation probability is identified with the transmission probability to enter the dissociation channel (large s) from the gas phase. The quantum mechanical scattering solutions are expressed as a superposition of plane waves for the lateral motion of the H_2 center of mass, spherical harmonics for the rotational motion and harmonic oscillator eigenfunctions for the vibrational motion perpendicular to the reaction path. The basis set used in the coupled-channel algorithm included rotational quantum numbers up to j_{max}=8, vibrational quantum number up to ν_{max}=2 and maximum parallel momentum p_{max}=$10\hbar G$ with $G = \min(G_X, G_Y) = \min(2\pi/a_X, 2\pi/a_Y) = 2\pi/a_Y$, where a_X and a_Y are the lattice constants of the surface unit cell of the (110) surface along the [10] and [01] directions, respectively. The convergence of the results as a function of the size of the basis set has been carefully checked. Since the vibration corresponds to the fastest time-scale in the H_2 dynamics, its motion is effectively decoupled from the motion of the remaining degrees of freedom. Therefore, five-dimensional vibrationally adiabatic calculations give results very similar to full six-dimensional calculations [10]. Because of the reduced

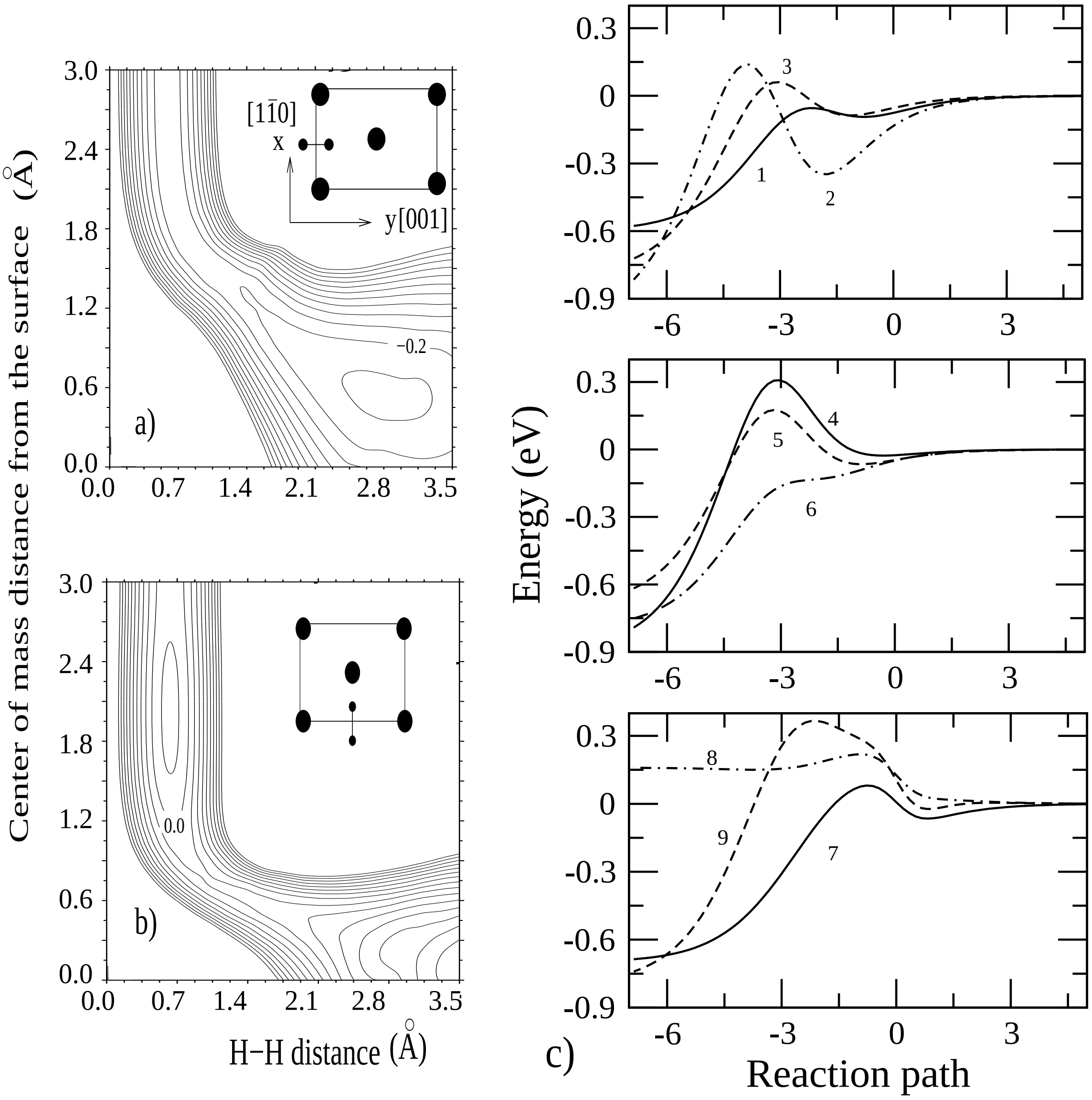

Figure 4.3: a) and b) Elbow potentials of H_2 at the short bridge and the long bridge position of Pd(110) according to the analytical interpolation of the *ab initio* results [72]. The coordinates are the H_2 center of mass distance from the surface Z and the H-H interatomic distance r. The molecular orientation is parallel to the surface and perpendicular to the corresponding bridge, as indicated in the insets. The level spacing of the contour lines is 0.2 eV. c) Potential energy as a function of reaction path for the different configurations.

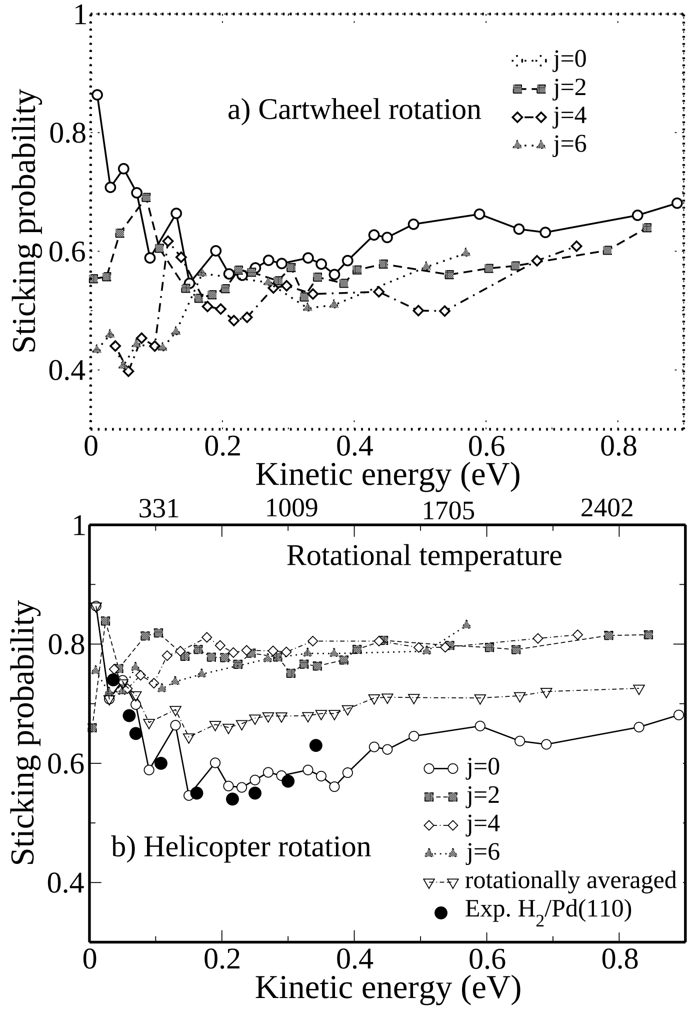

Figure 4.4: Calculated sticking probability of H_2 for a range of initial rotational states j as a function of kinetic energy under normal incidence. a) Molecules initially rotating in the cartwheel fashion $m = 0$, b) molecules initially rotating in the helicopter fashion $m = j$. The rotationally averaged results have been determined by averaging over rotational quantum numbers according to a Boltzmann distribution with a rotational temperature $T_{\text{rot}} = 0.8\,T_N$, where T_N is the nozzle temperature. The corresponding rotational temperatures are indicated above the figure. In addition, the experimental results of a molecular beam experiment are included [71].

computational effort, the majority of results presented later have been obtained in 5D vibrationally adiabatic calculations. However, we have carefully checked whether there is a significant deviation between 5D and 6D results.

4.1.4 Rotational effect on the reaction probabilities

In Fig. 4.4, we have plotted the calculated sticking probability of H_2 impinging on Pd(110) under normal incidence as a function of the kinetic energy for different initial rotational states. In Fig. 4.4b, results of a molecular beam experiment are included. It is obvious that the observed non-monotonous behavior of the sticking probability as a function of the kinetic energy is well-reproduced for initially non-rotating molecules ($j = 0$) in the calculations. It is now well accepted that the initial decrease of the H_2 sticking probability in non-activated dissociation systems with increasing energy is a consequence of the suppression of the steering effect [6, 9, 16, 66]: At low kinetic energies, the slow molecules can be very efficiently steered to nonactivated pathways towards dissociative adsorption by the attractive forces of the potential. This mechanism becomes less effective at higher translational energy leading to smaller dissociation probabilities.

As we see in Fig. 4.4, the dissociation probability strongly depends on the rotational state. Figure 4.4a shows the sticking probability for molecules rotating in the cartwheel fashion with $m = 0$. In these rotational states, the molecules have a high probability to hit the surface in an upright orientation in which they cannot dissociate. In addition, the dissociation probability is further reduced for molecules that are more rapidly rotating (higher j), in particular at low kinetic energies. Rapidly rotating molecules will rotate out of a favorable configuration for dissociation during the interaction with the surface. This rotational hindering [44, 60] becomes less effective at higher kinetic energies where the impinging molecules are rather fast. The steric effect competes against the rotational hindering and increases the sticking probability for the molecules rotating in helicopter fashion. If the molecules are rotating in the so-called helicopter fashion with $m = j$, then the rotational axis of the H_2 molecule is preferentially oriented perpendicular to the surface and the molecular axis of H_2 parallel to the surface. This orientation is favorable for dissociation. As Fig. 4.4b shows, additional helicopter rotation indeed leads to an enhanced sticking probability, which has also been found at other surfaces [6, 60]. Interestingly, the rotational enhancement of the sticking probability for helicopter molecules seems to be independent of the particular rotational quantum number j. We note that for higher rotational quantum numbers there is also a rotationally adiabatic effect in dissociative adsorption since the bond length $r_e(s)$ and thus the moment of inertia $I = \mu r_e^2(s)$ increases [44, 60]. For rotationally adiabatic motion, the rotational energy

$$E_{rot}(j) = \frac{\hbar^2 j(j+1)}{2I}, \tag{4.4}$$

in a particular rotational state decreases due to the rise in the moment of inertia I which leads to an effective energy transfer from rotation to translation. According to the previous chapter, if there are no rotationally adiabatic effects, one would expect that the dissociation probability decreases monotonously with increasing j, in particular for molecules rotating in the cartwheel fashion [60]. Figure 4.4a shows that the rotational hindering does not further rise for $j \geq 4$. This means that bond length effects play a significant role in the dissociation dynamics [44, 60]. In particular it means that the adiabatic energy transfer from rotations to translations contributes to the rotational effects in the system H_2/Pd(110).

In order to analyze the dependence of the sticking probability on the rotational state in more detail, we have plotted in Fig. 4.5 the calculated results for H_2 molecules

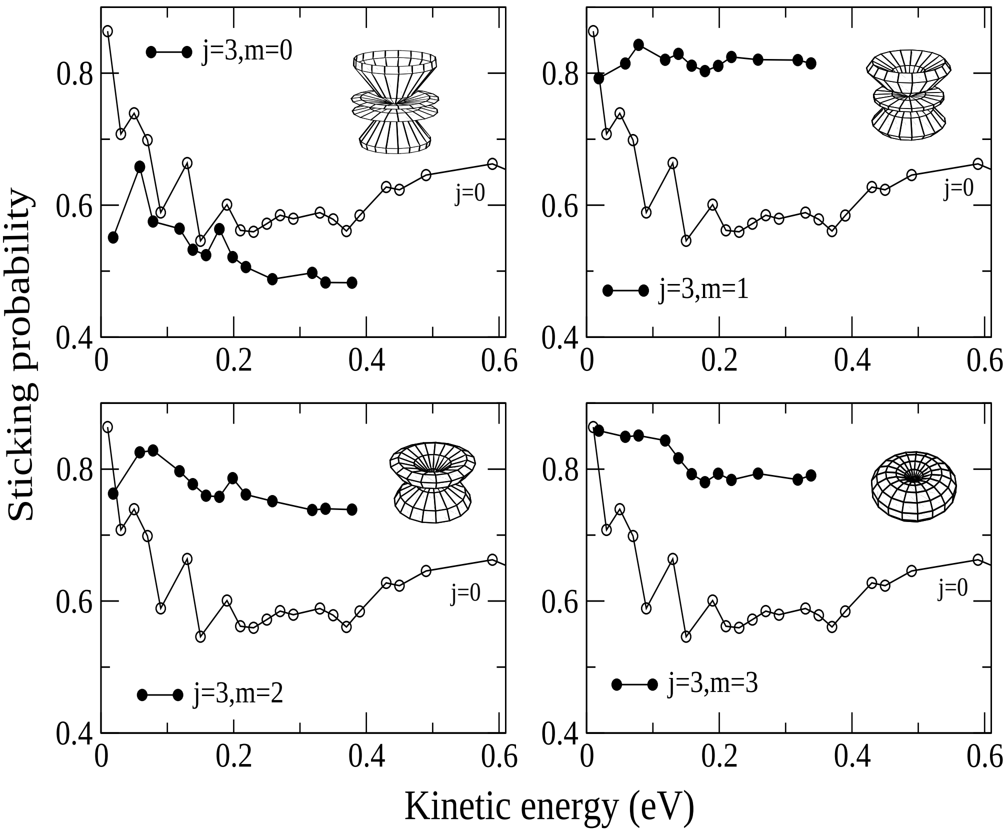

Figure 4.5: Calculated sticking probability of H_2/Pd(110) as a function of kinetic energy for H_2 molecules initially in the $j = 3$ state for different azimuthal quantum numbers m. For the sake of comparison, the results for $j = 0$ are also included. The insets show the probability distribution of the corresponding $(j = 3, m)$ rotational state.

initially in the $j = 3$ state for different azimuthal quantum numbers m. For $(j = 3, m = 0)$, we find the expected rotational hindering for this cartwheel mode. However, in contrast to other surfaces [11, 44] we find for all states with $(j = 3, m > 0)$ a significant enhancement of the sticking probability. We have confirmed that this is true not only for the $j = 3$ states, but also for the other j states. This strong enhancement represents a surprising results. As far as the rotational effects in the dissociation of H_2 at the more densely packed (111) and (100) surfaces are concerned, usually one finds a rotational enhancement smoothly increasing with m [11, 44]. We attribute the strong rotational enhancement for $m \geq 1$ found here to the rather open structure of the (110) surface which leads to a strong corrugation in the H_2-surface interaction. Perpendicular to the troughs which are running along the [10] direction there is pronounced variation of the barrier position which we can see, for example, for pathways 1, 2, 3 in Fig 4.3c. Then the orientation of the molecule parallel to the surface is not necessarily the energetically most favorable one. This might be the cause for the rotational enhancement of any $m \geq 0$ rotational mode, not just the $m = j$ helicopter mode. This strong rotational enhancement has several consequences that could be observed experimentally.

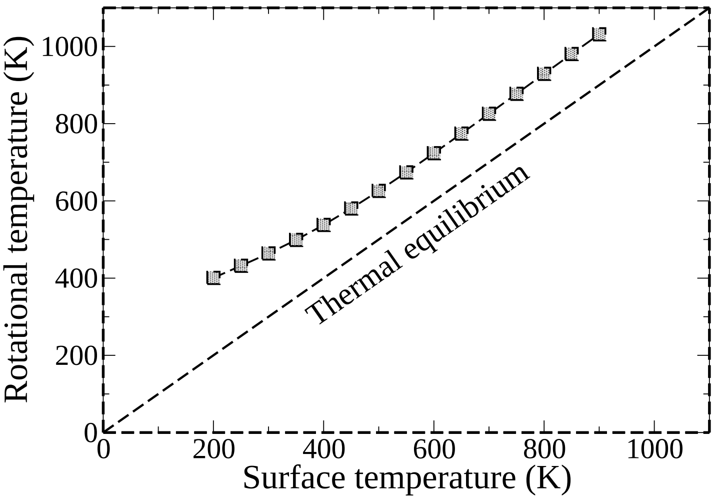

Figure 4.6: Rotational temperature of desorbing H_2 molecules as a function of surface temperature. The solid line represents the thermal equilibrium.

As mentioned in Sec. 4.1.2, the H_2 molecules in the molecular beam experiments are not in their ro-vibrational ground state. The distributions are rather characterized by Boltzmann factors with effective temperatures. As far as the rotations are concerned, the corresponding temperature is about 80% of the nozzle temperature T_N, which is related to the kinetic energy by $E_{kin} = \frac{5}{2} k_B T_N$ [34]. We have simulated this effect by determining a rotationally averaged sticking probability according to

$$S_{tot}(E_{kin}) = \frac{1}{Z} \sum_{j,m} S(E_{kin}, j, m) \exp\left(\frac{-E_{rot}(j,m)}{k_B T_{rot}} \right) , \tag{4.5}$$

where Z is the partition sum, and T_{rot} is specified by $T_{rot} = 0.8 \cdot T_N = 0.8 \cdot 2 E_{kin}/(5 k_B)$. The sticking probability determined according to Eq. 4.5 is also included in Fig. 4.4b. Due to the fact that almost all rotational states with $m > 0$ cause an enhancement of the sticking probability, the combined effect of all rotational states is to lead to an effective increase in the sticking probability at kinetic energies larger than 0.1 eV. This effect should in fact be seen experimentally, if the rotational temperature of the molecular beam is changed by seeding techniques. This rotational effect in the dissociation probability should also be observable in the time-reversed process of dissociative adsorption, the associative desorption. The strong rotational enhancement in adsorption should also lead to a so-called rotational heating in desorption. The rotational temperature in desorption is related to the mean rotational energy $T_{\mathrm{rot}} =< E_{\mathrm{rot}} > /k_B$. Thus, the mean rotational energy of desorbing molecules should be larger than in thermal equilibrium. In Fig. 4.6, we have plotted the calculated rotational temperatures in desorption as a function of the surface temperature. Indeed we find a small rotational heating which has not been found before in the desorption of molecules. Usually one finds rotational cooling in desorption [26]. Unfortunately, the rotational effects in the system H_2/Pd(110) have not been measured yet. We note, however, that for H_2/Pt(110), no rotational enhancement has been found for $j = 1$ and $j = 2$, but rather

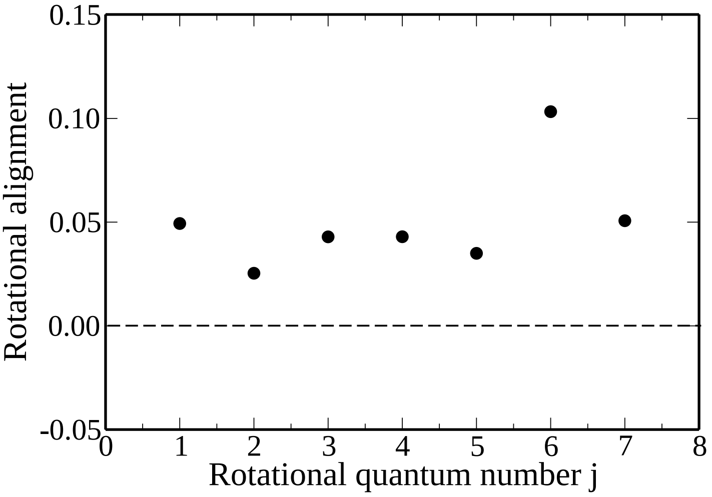

Figure 4.7: Calculated rotational alignment in desorption as a function of the rotational quantum number for a surface temperature of $T = 700$ K.

a rotational hindering [56].

As a further property of desorbing molecules, the rotational alignment can be measured [36, 37, 46]. It is expressed by the quadrupole moment of the orientational distribution of desorbing molecules as defined in Eq. 3.10. The quadrupole alignment factor $A_0^{(2)}$ can be experimentally determined by using REMPI and LIF, and gives us information regarding the degree of alignment and orientational preference of H_2. Molecules rotating preferentially in the cartwheel fashion have an alignment parameter $A_0^{(2)}(j) < 0$, while for molecules rotating preferentially in the helicopter fashion $A_0^{(2)}(j) > 0$. From the calculated sticking probabilities, desorption distribution can be directly derived using the principle of microscopic reversibility [26, 60]. Fig. 4.7 shows the calculated rotational alignment for a surface temperature of 700 K. Since the sticking probability is enhanced for $m > 0$, the molecules desorb preferentially in states with $m > 0$. This leads to a positive alignment parameter. However, this alignment is much smaller than found for H_2 and D_2 desorbing from other surfaces [11, 36–38, 60]. This is at first surprising result regarding the strong enhancement of the sticking probability for molecules rotating in the helicopter mode. However, rotational states with $m > 0$ show a strong enhancement of the sticking probability. The small alignment is caused by the fact that the rotational enhancement is similar for all $m > 0$ states so that there is no pronounced preference for the maximum $m = j$ state.

4.1.5 Parallel momentum effects

Let us now focus on the role of the corrugation in the dissociation dynamics. The dependence of the sticking probability on the angle of incidence θ_i is directly related to the corrugation of surface. For a perfectly flat surface, the sticking scales with the normal component of the translational energy, the so-called *normal-energy scaling*, due to the fact that the parallel momentum cannot be converted into normal momentum [52].

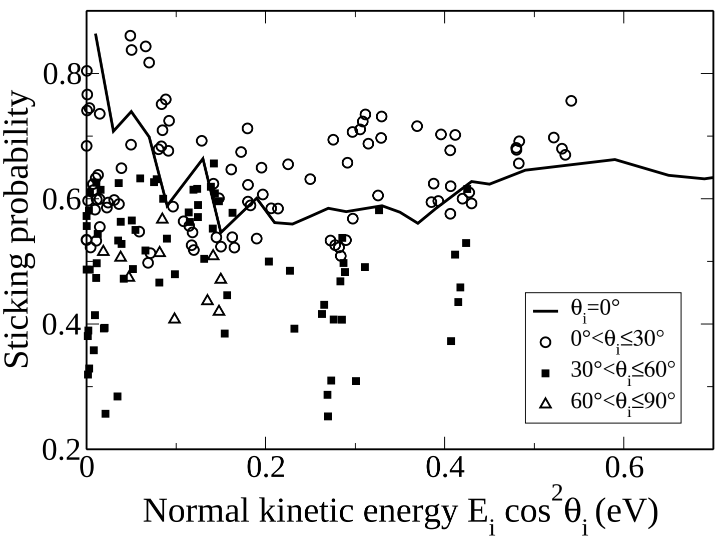

Figure 4.8: Sticking probability as a function of normal component of the incident energy for molecules initially in the vibrational and rotational ground state. The solid line denotes the normal-incidence data while the results for non-normal incidence are grouped according to their angle of incidence θ: 0° − 30°: circles, 30° − 60°: boxes, 60° − 90°: triangles. Note that the non-normal incidence data are obtained for different azimuthal angles.

However, for a corrugated surface also the parallel component of the kinetic energy will play a role. In Fig. 4.8, we have summarized our results for the sticking probability for different angles of incidence as a function of the normal component of the kinetic energy. If we had normal-energy scaling, all the data should be very close to the sticking curve for normal incidence, $\theta = 0°$. However, we see that additional parallel momentum strongly influences the sticking probability due to the strong corrugation of the H_2/Pd(110) PES. The dependence on the angle of incidence is in fact much stronger than on the smoother Pd(100) surface, which has been reported by Groß *et al.* [9].

We first note that the influence of additional parallel momentum on the dissociation probability shows a non-monotonous behavior. For an angle of incidence larger than 30° the dissociation is suppressed compared to the normal-incidence results. For angles of incidence below 30°, there is both a suppression and an enhancement of the sticking probability caused by additional parallel momentum. For the majority of incidence conditions with $\theta \leq 30°$, however, additional parallel momentum enhances the dissociation. Furthermore, we see a large scatter in the data for the same normal kinetic energy. This is caused by the strong corrugation which leads to a strong dependence of the sticking probability on the lateral kinetic energy at the same normal kinetic energy. In addition, it is caused by the azimuthal anisotropy of the (110) surface. The atom rows along the troughs running in the $[1\bar{1}0]$ direction which we denote by [10] or x (see the inset in Fig. 4.3a) are in fact close-packed. One would expect that along this direction the corrugation is relatively weak. However, the DFT calculations [72] as well as our parameterization (see Fig. 4.3c) showed that there is a strong variation of the barrier height to dissociative adsorption between the top site and the short bridge site

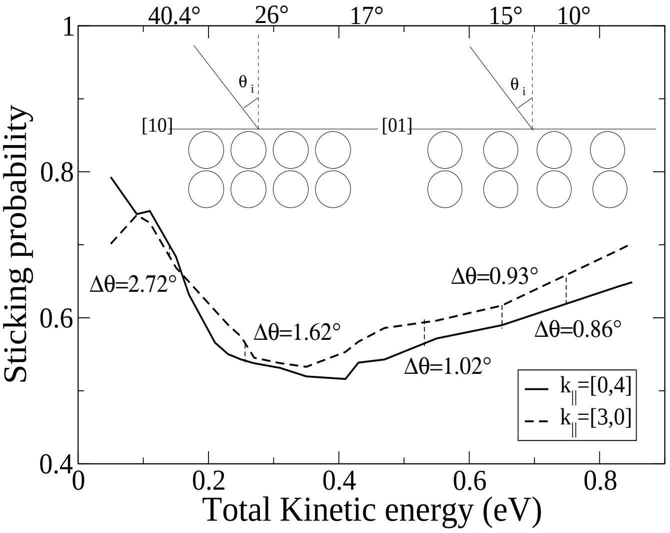

Figure 4.9: Sticking probability as a function of the total kinetic energy under non-normal incidence along the [10] and [01] directions, respectively. The parallel momentum has been kept fixed to $p_\| = 3\hbar G_X \equiv [30]$ and $p_\| = 4\hbar G_Y \equiv [04]$. The corrugation along these different directions is indicated in the insets. The angles of incidence for the [10] direction are shown at the upper axis, and the difference in the incident angles to the [01] direction are added in the figure.

along [10], whereas along the [001], [01] or y direction perpendicular to the troughs, it is rather both the barrier position and height that varies.

In Fig. 4.9, we have plotted the sticking probability for non-normal incidence along the [10] and [01] directions, respectively, for constant parallel momentum. In order to save the computational time, we have determined the sticking probability for non-normal incidence only for parallel momenta that correspond to vectors of the surface reciprocal lattice. Note that the ratio between the length of the two unit vectors of the surface reciprocal lattice is $G_X/G_Y = \sqrt{2}$. Since $\sqrt{2}$ is no rational number, it is impossible to get the same angle of incidence along different azimuths if the parallel momenta are multiples of the reciprocal lattice vectors. In Fig. 4.9, we show results for two parallel momenta, $p_\| = 3\hbar G_X$ and $p_\| = 4\hbar G_Y$, since $3G_X \approx 4G_Y$.

We find that except for the lowest energies, the sticking probability for an angle of incidence along the [10] direction is larger than along the [01] direction. However, the differences are still relatively small. We have analyzed the dependence of the sticking probability on the angle of incidence for three different azimuths in more detail in Fig. 4.10. In addition to the [01] and [10] directions we have also considered the [11] direction which corresponds to the diagonal of the surface Brillouin zone. At the lowest kinetic energy, $E_i = 0.05$ eV, the sticking probability is almost independent of the angle of incidence, in agreement with the experimental results [71]. A similar behavior has also been found in the case of H_2/Pd(100) [9, 24]. At higher kinetic energies, there is first a slight increase in the sticking probabilities with increasing angle of incidence, and then a decrease which is most pronounced at the highest kinetic energy considered, $E_i = 0.7$ eV. Except for the lowest kinetic energies, the highest sticking probabilities are found for the incidence along the [10] direction. In order to analyze the effect of the corrugation on the sticking probability, it is helpful to distinguish between so-called energetic and geometric corrugation [44, 52]. Energetic corrugation corresponds to a situation in which only the barrier height but not its position is varied while in the case of geometric corrugation it is the other way around. In the case of energetic corrugation, additional parallel momentum leads to an effective averaging over the barriers within the surface unit cell. This causes a suppression of the sticking probability for kinetic energies below the average barrier height [44, 52]. At a geometrically corrugated surface, on the other hand, the sticking probability is increased by additional parallel momentum. This increase is caused by the fact that an impinging molecular beam under non-normal incidence will hit a larger fraction of barriers where the local potential gradient is aligned to the direction of incidence [44, 52]. This effect can be so strong that it leads to an enhanced sticking probability for non-normal incidence for constant kinetic energy. However, it is important to note that for a highly corrugated surface no clear distinction between energetic and geometric corrugation can be made. For example, strong energetic corrugation can lead to a variation of equipotential contour lines below the minimum barrier height that is rather similar to the variation caused by geometric corrugation alone. Furthermore, for a system with both activated and non-activated paths to dissociative adsorption, such as H_2/Pd(110), again no real distinction between energetic and geometric corrugation can be made since for the non-activated paths no barrier location can be defined.

At the lowest kinetic energies in Fig. 4.10, $E_i = 0.05$ eV, the steering effect is operative. The fact that the sticking probability is almost constant as a function of the polar and azimuthal angle of incidence indicates that the steering effect does not depend on the angle of incidence. At higher energies, steering becomes less effective. As Fig. 4.10 shows, the angular dependence of the sticking probability for incident beams along the [01] and the [11] direction is rather similar. Both show first a slight increase as a function of the incident angle with a maximum at 20°-30°, and then a decrease which is the stronger, the higher the kinetic energy.

The [10] direction corresponds to the direction along the close-packed rows of the (110) surface. One would expect that along this direction the corrugation is less pronounced than along the [01] direction which is perpendicular to the troughs of the (110) surface. Hence it is surprising that we find an initial increase in the sticking probability as a function of the angle of incidence in an energy regime where the sticking probability is rising as a function of the kinetic energy for normal incidence. Hence this increase is indicative of a strong corrugation effect along this direction. And indeed, an analysis of the PES confirms that the variation of the transition state energies for some fixed molecular orientation has a larger variation along the close-packed [10] direction than along the [01] direction (compare, e.g., pathways 1, 2, 3 with pathways 4, 5, 6 or pathways 8 and 9 with pathways 1 and 8 in Fig. 4.3c). Along the [01] direction, i.e. perpendicular to the troughs of the (110) surface, the sticking probability does not exhibit any significant increase as a function of the angle of incidence. This result is in fact in agreement with simple three-dimensional calculations for a system with both activated and non-activated paths to dissociative adsorption, where the role of additional parallel

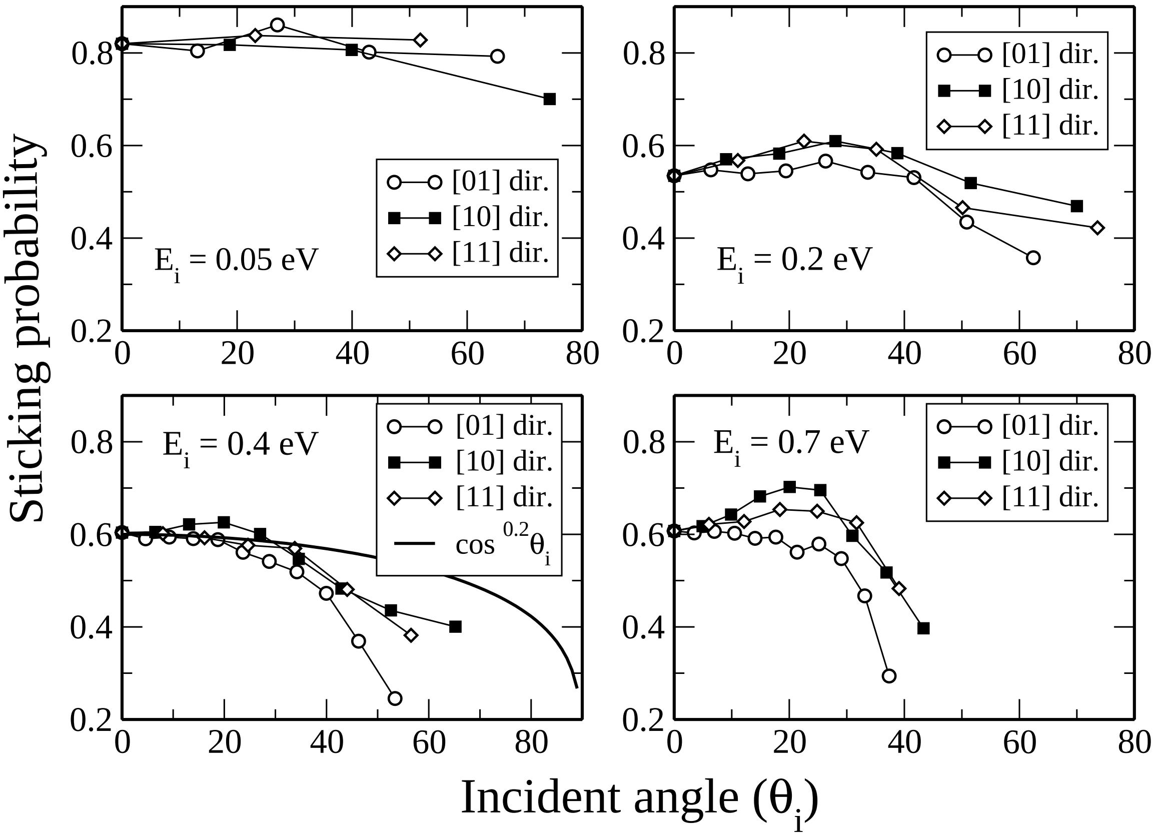

Figure 4.10: The sticking probability as a function of incident angle at different initial kinetic energies. The azimuthal angles of incidence are along the [01], [10] and [11] directions, respectively.

momentum has been found to be rather similar to the case of energetic corrugation in a purely activated system [52]. The fact that the results for the azimuthal incidence along [01] and [11] are very similar demonstrates that a molecular beam incident along the diagonal of the surface Brillouin zone also experiences a strong corrugation. In the experiment [71], the incident azimuth has not been specified. For $E_i = 0.35$ eV, the sticking probability has been found to scale according to $S(\theta_i) \propto \cos^{0.2}\theta$. We have included this scaling in the panel for $E_i = 0.4$ eV of Fig. 4.10. For angles below $30° - 40°$ experiment and theory agree well, depending on the azimuth. Above 40°, the theoretical results seem to be smaller than the experimental curve. However, also the range of incident angles used in the experiment has not been specified in Ref. [71].

4.2 Scattering of H_2 from Pd(110)

4.2.1 Introduction

In order to complement the six-dimensional quantum dynamical study, we will also investigate the scattering of hydrogen molecules from the Pd(110) surface. Of course, not all molecules in a beam will be oriented correctly to be able to dissociate, and these will then contribute to diffraction. A strong corrugation of the potential energy surface has a considerable influence on the angular distribution of the reflected portion of a molecular beam since molecules incident at different sites will be scattered through different angles. Because of the transfer of kinetic energy into the internal degree of freedom of the molecule rotational and vibrational states can be excited during the scattering process [39, 41]. The molecular vibrations follow the scattering process almost adiabatically due to the short time scale of the molecular vibration. However, for a strong anisotropic surface, the molecular rotation can be efficiently excited during the scattering process. This rotational excitation leads to additional peaks in the diffraction pattern, the so-called rotationally inelastic diffraction peaks.

There are two qualitatively different ways in which the solid could assist in transforming the translational energy into the rotational one. In a purely diffractive process the initial and final kinetic energy and parallel momentum of the molecule are strictly conserved within a reciprocal lattice vector, while in a dissipative scattering process, in addition to the above, surface phonons are created/annihilated covering a much wider range of possible scattering energies and parallel momenta. In the case of D_2 and H_2 scattered from LiF(100) surface, no evidence of a direct lattice vibration coupling to the rotational states has been found [74], whereas surface phonon exchange occurring simultaneously with the molecule rotational transition has been reported for H_2 on NaF(001) surface [75]. Experimentally, rotationally inelastic diffraction of hydrogen molecules has been first observed in the scattering from MgO [76] and NaF [75]. For metal surfaces with a high barrier, the rotationally inelastic diffraction peaks are hard to resolve apart from HD scattering [77]. Bertino *et al.* [78] resolved rotationally inelastic peaks as well as rotationally elastic ones in the diffraction pattern of D_2/Ni(110). Also, deuterium scattering from Rh(110) surface has been studied by Cvetko *et al.* [79]. They have reported rotationally inelastic scattering involving the D_2 rotational transition $j \rightarrow 2$ which has been derived from the observed diffraction patterns. Furthermore, in this system, quite strong off-specular diffraction peaks have been observed.

Gross *et al.* [41] have looked at rotationally elastic and inelastic diffraction for H_2/Pd(100) at normal and off-normal incidence. They have found a high intensity in off-specular as well as rotationally inelastic diffraction peaks. In particular, the off-specular diffraction intensities indicate a high corrugation in the PES. In the case of the more corrugated Pd(110) we have found that some off-specular peaks become larger than specular peaks, especially at small incident angles. Also, the intensity of some rotationally inelastic peaks is higher than rotationally elastic ones.

In the present work, after discussing some calculational details, we will first look at the angular distribution of the scattering intensity , then the energy dependence of the rotationally elastic and inelastic diffraction probability at normal and off-normal incidence will be studied.

4.2.2 Calculational details

The coherent elastic scattering of molecules is more complex than atomic scattering because in addition to parallel momentum transfer the internal degrees of freedom of the molecules, rotations and vibrations, can be excited during the scattering process. Consider a beam of molecule with initial wave vector $\mathbf{K}_i$ and final wave vector $\mathbf{K}_f$ which is scattered elastically at a periodic surface. The energy conservation is expressed in the following form:

$$\frac{\hbar \mathbf{K}_f^2}{2M} = \frac{\hbar \mathbf{K}_i^2}{2M} + \Delta E_{rot} + \Delta E_{vib}. \tag{4.6}$$

In fact, in this conservation relation, the energy transfer processes to the surface is neglected due to the rigid surface approximation. Furthermore, due to the adiabatic property of molecular vibrations, the excitation of molecular vibrations in molecule-surface scattering is negligible, while the anisotropy and corrugation of the surface leads to rotationally inelastic diffraction probabilities.

Bloch's theorem states that in scattering of particles from a crystal surface, only well defined parallel translational momentum states (diffraction states) are allowed due to the periodicity of the surface. Then, the component of the wave vector parallel to the surface after the scattering is given by

$$\mathbf{K}_f^{||} = \mathbf{K}_i^{||} + \mathbf{G}_{mn}, \tag{4.7}$$

where $\mathbf{G}_{mn}$ is a vector of the two-dimensional reciprocal lattice. The internal parallel momentum dose not change ($\mathbf{G}_{mn} = 0$) for the so-called specular peak. In the case of an anisotropic and corrugated surface the probability of off-specular diffractions are considerable.

As mentioned in Sec. 2.3.2, in the solution of the time-independent Schrödinger equation based on the coupled-channel scheme both the sticking coefficient as well as the reflection coefficient is included. Therefore, the reflection matrix is obtained with the same parameterization of the PES as before within the coupled-channel method using the combined INTRA-LORE method. Here, we only considered incident parallel momenta corresponding to a reciprocal lattice vectors to reduce the computational effort.

4.2.3 Angular distribution of scattering intensity

The scattering intensity as a function of the final angle of the molecule has been plotted in Fig. 4.11. The total initial kinetic energy is $E_i = 82$ meV. The incident parallel momenta correspond to $2\hbar G_X$ ($3\hbar G_X$) along the $< 1\bar{1}0 >$ or [10] and $3\hbar G_Y$ ($4\hbar G_Y$) along the $< 001 >$ or [01] direction which leads to the small (large) incident angles illustrated in Fig 4.11. The molecules are initially in the rotational ground state $j_i = 0$ and (m, n) corresponds to the parallel momentum transfer $\Delta \mathbf{G}_{||} = (mG_X, nG_Y)$.

At the small incident angle some off-specular peaks are clearly higher than the specular peak for the incidence along both directions. The highest peak occurs in fact for the backscattering into the direction of incidence which corresponds to the fourth order diffraction peak at $\theta_f = -20°$ for the molecule incident along the [01] direction. The same mechanism is also operative for the molecule incident along the [10] direction in which the most probable angle of scattering is at $\theta_f = -15°$. The

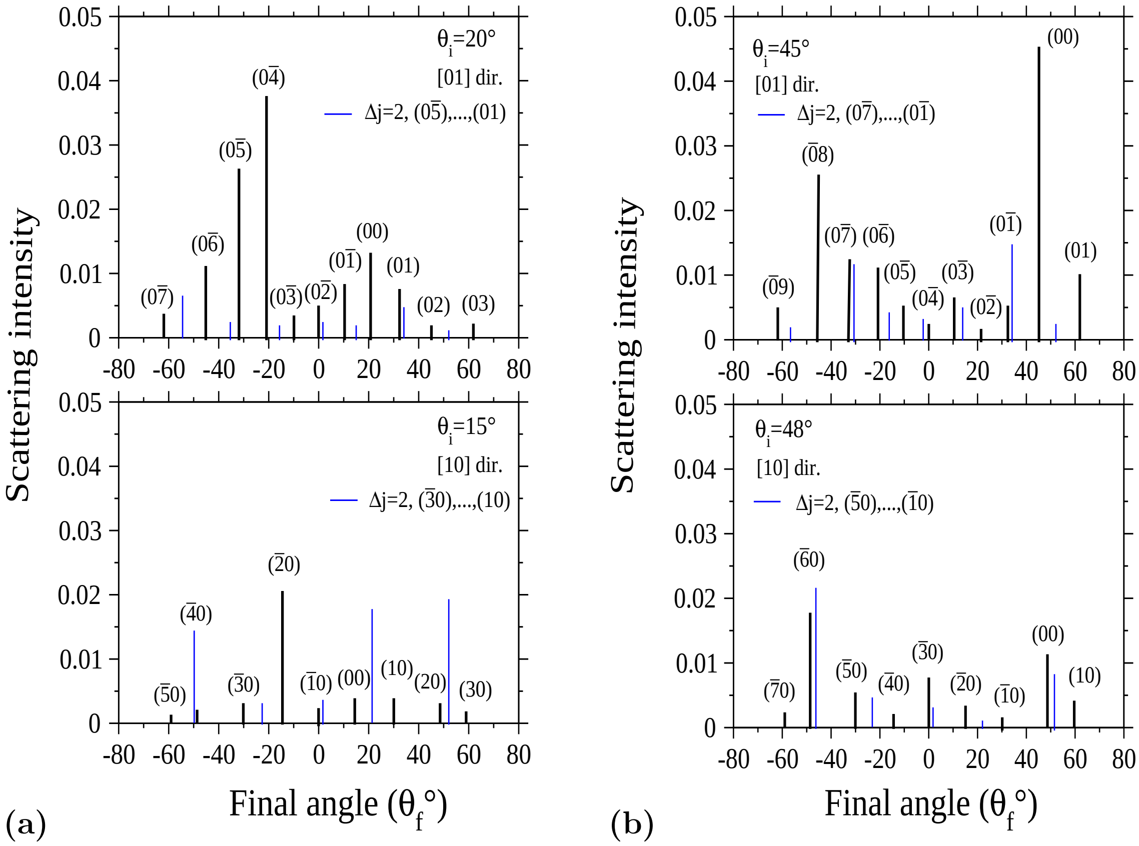

Figure 4.11: Scattering intensity as a function of final angle in the different parallel momentum transfer a) for small incident angle, b) for large incident angle. The initial kinetic energy is E_i=82 meV along the $< 1\bar{1}0 >$ and $< 001 >$ directions and the molecule are initially in the ro-vibrational ground state. Thick lines correspond to the rotationally elastic and thin lines to the rotationally inelastic scattering.

presence of high diffraction peaks for $G \neq 0$ in Fig. 4.11 confirms the strong corrugation of the H_2/Pd(110). At the higher incident angle the distribution of scattering angle along the [01] and [10] direction behaves differently so that specular diffraction peak is larger than off-specular diffraction peaks along [01] direction while along the [10] direction the $(\bar{6}0)$ diffraction peak becomes larger than the specular peak. It should be noted that in a helium atom scattering experiment the off-specular peaks are about two orders smaller than the specular peak [80]. Because of the strong corrugation and anisotropy of the H_2/Pd(110) potential energy surface, the molecules incident at the different sites will be scattered through different angle, hence, the angular distribution of the scattering intensity is sensitive to the incident angle and site of incidence.

In addition, rotationally inelastic diffraction peaks corresponding to the rotational excitation $j = 0 \rightarrow 2$ are plotted in Fig. 4.11. The intensity of the rotationally inelastic diffraction peaks is comparable to the rotationally elastic ones. Actually, the intensity of some rotationally inelastic peaks is higher than the roationally elastic ones along the [10] direction, due to the large variation in the transition state height and position

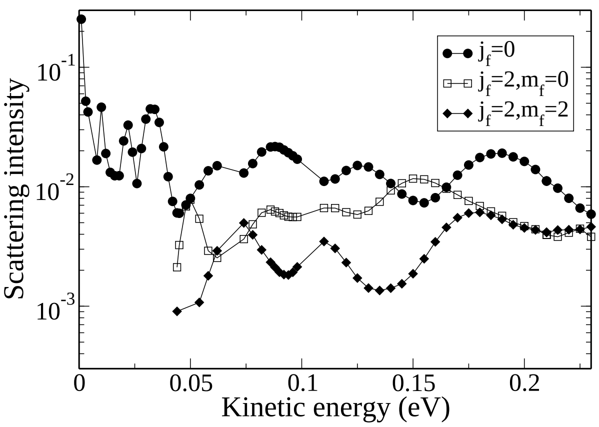

Figure 4.12: The excitation probability as a function of internal kinetic energy under normal incidence. The rotational axis of scattering molecule is parallel to the surface for the so-called cartwheel rotation ($m_f = 0$) and perpendicular to the surface the so-called helicopter rotation ($j_f = m_f$).

along this direction. It demonstrates that more parallel momentum energy could be converted into the rotational energy to assist the rotational excitation. The rather low probability of elastic rotationally scattering for the incidence along the [10] direction can be caused by higher inelastic rotationally scattering, it means only a few non-rotating molecules start to rotate during the scattering process.

The results for the rotationally inelastic diffraction peaks $j = 0 \rightarrow 2$ have been summed over all final azimuthal quantum number m_j but for all peaks the excitation probability for cartwheel rotation is approximately one order of magnitude larger than for helicopter rotation.

The scattering probability as a function of kinetic energy is shown in Fig. 4.12 for the scattered molecule in the cartwheel and helicopter fashion. The scattering intensity for the non-rotating molecule is also included to compare with rotating molecule. According to the principle of detailed balance, in a equilibrium situation the internal flux on the surface from the gas-phase should equal the desorption and scattering flux. Therefore, if the molecule rotates preferentially in helicopter fashion in the adsorption process, in scattering the cartwheel rotation should dominate.

4.2.4 Energy dependence of the scattering intensity

In Fig. 4.13 the results of the scattering intensities for normal incident molecular beams initially in the ro-vibrational ground state for different diffraction peaks in roationally elastic and inelastic conditions are shown. In the experiment, the molecular beams are not monoenergetic molecular beams but have a certain velocity spread; therefore, we have averaged our results with a Gaussian function with an initial velocity spread $\Delta v_i/v_i = 0.05$ close to the experimental conditions. The results show the oscillatory behavior in the scattering intensity which is a consequence of the quantum nature of H_2 scattering. Let us first focus on the specular peak. The oscillations at low energies

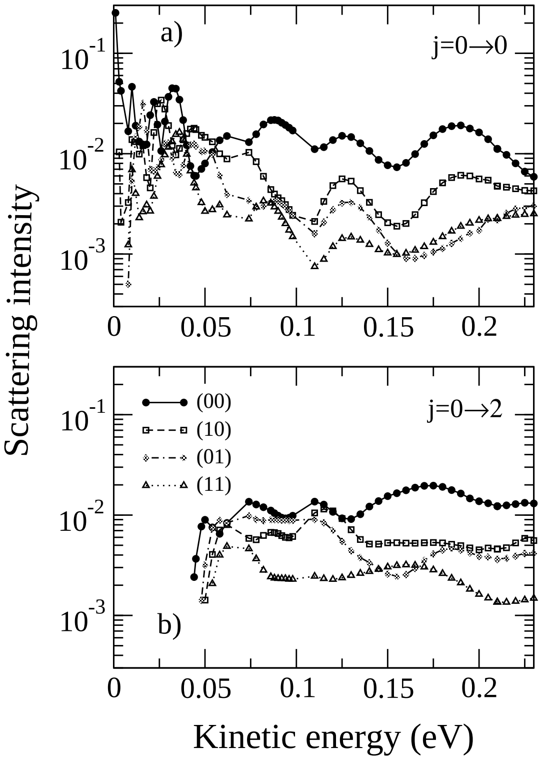

Figure 4.13: Scattering probability as a function of kinetic energy with an initial velocity spread $\Delta v_i/v_i = 0.05$ in the ro-vibrational ground state under normal incidence. a) Rotationally elastic b) rotationally inelastic diffraction. The results are summed over all final azimuthal quantum number m_j.

reflect the opening up of new scattering channel. The first pronounced dip at E_i= 10 meV coincides with the opening up of (01) and (11) diffraction peaks. The starting point of the rotationally inelastic scattering channel at E_i= 45 meV correspond to the dip of specular intensity and the two peaks for the (01) and (10) diffraction levels. This strong coupling between parallel momentum and rotational excitation is due to the anisotropy and corrugation of the potential energy surface.

Not all peaks are due to the opening up of new scattering channels. Because of the transfer of normal momentum to parallel momentum and angular momentum molecular adsorption states can turn into scattering states and the suppression of the sticking probability enhances the scattering intensity. The scattering resonances can also be caused by this so-called selective adsorption resonance.

A closer look at Fig 4.13 indicates that the probability of the specular peak is higher than the off-specular peaks, however, due to the larger variation of the barrier heights along the [10] direction which is caused by the strong corrugation along this direction, the (10) diffraction probability is larger than the (01).

The scattering intensity under off-normal incidence has been plotted in Fig. 4.14 along and perpendicular to the troughs running in $[1\bar{1}0]$ direction. The initial parallel momentum is $p_{||} = 2\hbar G_X$ along the $< 1\bar{1}0 >$ and $p_{||} = 3\hbar G_Y$ along the $< 001 >$

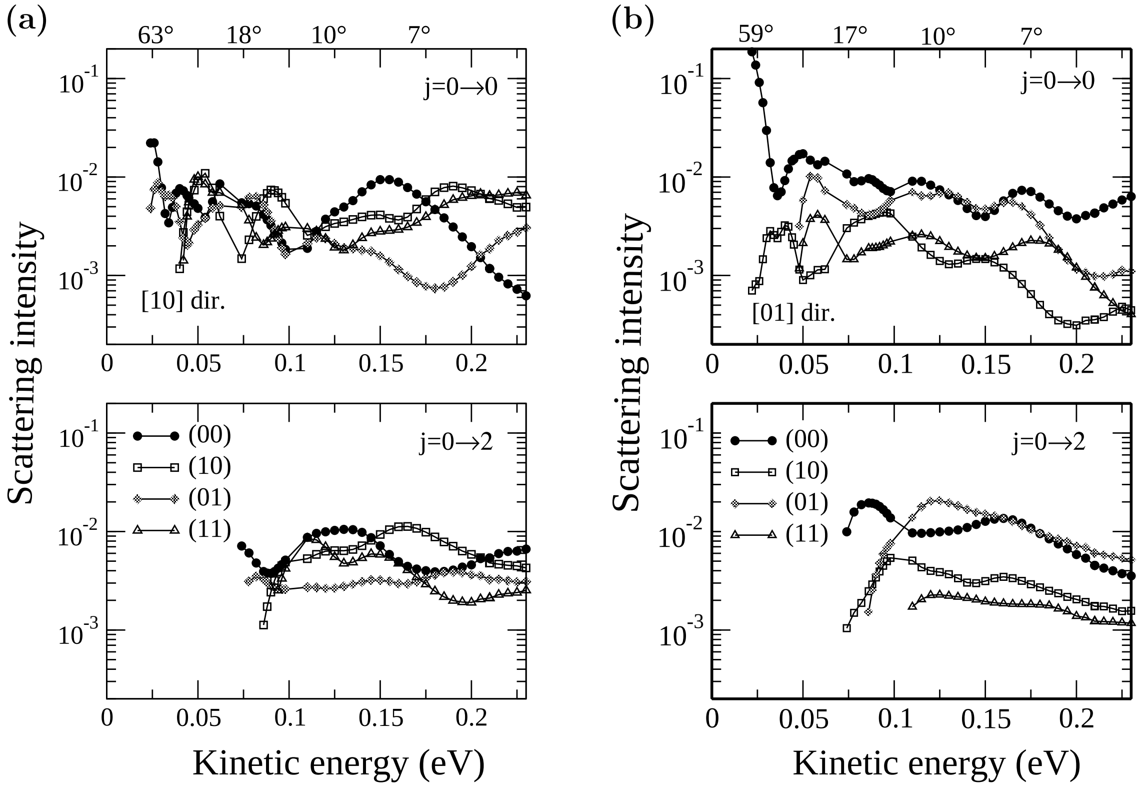

Figure 4.14: Scattering probability as a function of kinetic energy with an initial velocity spread $\Delta v_i/v_i = 0.05$ in the ro-vibrational ground state under off-normal incidence. The incident parallel momentum corresponds to the a) $2\hbar G_X$ along the $< 1\bar{1}0 >$ direction and b) $3\hbar G_Y$ along the $< 001 >$ for rotationally elastic $j = 0 \rightarrow 0$ and rotationally inelastic $j = 0 \rightarrow 2$ scattering. The intensities are summed over all final azimuthal quantum number.

directions. The comparison between scattering intensities in high symmetry directions should be made for the same incident angle. Since the ratio between the length of the two unit vectors of the surface reciprocal lattice is $G_X/G_Y = \sqrt{2}$ it is impossible to obtain the same angle for different directions if the incident parallel momentum corresponds to a reciprocal lattice vector, but $(p_{||})_{01}/(p_{||})_{10} = 1.5$ is almost equal to $\sqrt{2}$. The scattering probability depends on the incident angle which is given at the upper x-axes in the figures. Under off-normal incidence, the probabilities of the off-specular peaks are very close to the specular peak because the change of parallel momentum in molecule-surface scattering is much more probable for off-normal incidence than for normal incidence. The probability of the specular peak decreases at high energies such that at around 0.25 eV it becomes lower than all of off-specular peaks for molecule incidence along the [10] direction. For an angle of incidence along the troughs running in $< 1\bar{1}0 >$ direction, the scattering intensity of the (10) diffraction level is larger than the (01) diffraction while along the [01] direction it is the other way round. Because of the energetic corrugation along the [10] direction the transfer of parallel momentum into the x-component is more probable than the y-component while along the [01] direction it is vice versa, due to the geometric corrugation. Because of the strong anisotropy and corrugation of H_2/Pd(110) some off-specular rotationally inelastic scattering intensity becomes larger than the (00) peak at higher energies so that along the [10] direction the off-specular diffraction (10) is more probable than specular diffraction. This behavior has also been found for scattering of hydrogen molecules from Pd(100) [41]. This has been attributed to the fact that the rotationally anisotropic component of the potential is more corrugated than the isotopic component. Because Pd(110) is a more corrugated surface, this also causes the high probability of some off-specular rotationally inelastic scattering for H_2/Pd(110).

Chapter 5

Dissociative adsorption of H_2 on Rh(111)

In this chapter we will discuss the dissociative adsorption of H_2 on Rh(111). In particular, we will follow the interaction process of rotating molecules on the azimuthally flat surface.

5.1 Introduction

Molecular beam experiments as well as quantum dynamical studies for non-activated adsorption systems indicate that the sticking probability under normal incident of molecules on a surface first decreases with energy at low kinetic energy, and then increases at high kinetic energy [6–8, 11]. As shown by Gross *et al.* [8, 9, 41], the sticking curve for non-rotating hydrogen molecule on Pd(100) exhibits strong oscillations which are especially pronounced at low kinetic energies. Most of these can be attributed to the opening up of new scattering channels whenever a new rotation-diffraction channel becomes open, the total reflection probability goes through a maximum, and the sticking probability through a minimum. Still, the oscillations were also observed at energies at which new channels do not open up. These are caused by temporary trapping into metastable adsorption states due to energy transfer to parallel motion [81] or rotational motion [82]. The choice of H_2/Rh(111) study is motivated by an interesting available experimental result. In the experimental sticking curve versus kinetic energy for D_2/Rh(111) a step at 450 meV is observed. The first suggestion was the opening up of new dissociation channel at this energy.

In order to analyze this step in the sticking probability, the dissociative adsorption of H_2 on Rh(111) is studied in this work. The potential energy surface is obtained by *ab initio* total energy calculation using density functional theory and the (GGA). As usual, two approximations are made. First, the Born-Oppenheimer approximation is made to decouple the motion of the electrons from the nuclear motion, restricting the

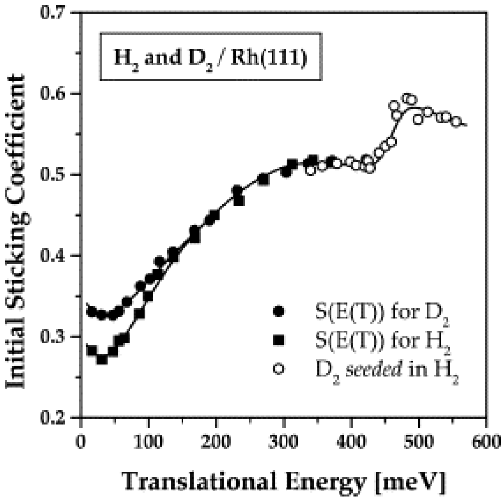

Figure 5.1: Sticking probability of hydrogen and deuterium on Rh(111) as a function of beam energy according to experimental measurement [13]. At around 450 meV there is a bump in the sticking curve. Surface temperature is T$_s$=223 K.

reaction to take place on the electronic ground state PES only. In this way, electron-hole pair excitations are neglected. Second, the energy exchange with the surface through phonons is also neglected. Employing these two well-known approximations we have solved the Schrödinger equation using a coupled-channel method.

This chapter will start with the presentation of the experimental situation and the description of the computational method including the analytical form of the PES based on symmetry-adapted functions and quantum calculational details, and at the end we will present the dynamics results.

5.2 Experimental situation

One of the experimental methods for obtaining a certain control over the translational and internal degrees of freedom in a molecular beam is the seeding technique, that is mixing the gas of interest with another gas of different molecular mass. A heavier seed gas slows the molecules down and a lighter seed gas speeds them up. Seeding allows an investigation of possible contributions of internal energy of the molecule, and one can obtain higher kinetic energies that are not accessible using the pure gas. M. Beutl *et al.* [13] measured the energy dependence of the sticking coefficient for hydrogen and deuterium on Rh(111). According to M. Beutl *et al.* there is a difference between $S[E(T)]$ and $S[E]_{T=const.}$ curves. It indicates that the rotational state of the hydrogen molecule influences the sticking coefficient. In Fig. 5.1 this experimental results are shown. The most interesting finding in Fig. 5.1 is the step in the dependence of the sticking coefficient for deuterium at a beam energy at around 450 meV. The sticking coefficients in this energy range were obtained by seeding deuterium in hydrogen. Beutl *et al.*, additionally obtained the angular variation of the sticking coefficient at a beam energy of 495 meV. A plot of the $S(\theta)$ data versus normal energy shows the step in

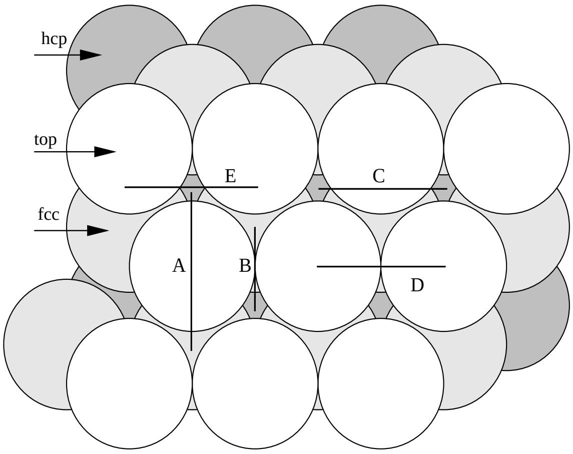

Figure 5.2: Schematic presentation of (111) surface showing different geometries with the molecule parallel to the surface used in *ab initio* calculations: (A) fcc-top-hcp; (B) fcc-br-hcp; (C) fcc-top-fcc; (D) top-br-top; (E) top-fcc-top.

the sticking curve, too. It is attributed to the fact that with increasing the beam energy from 400 meV to 500 meV an additional adsorption channel within the unit cell becomes available.

5.3 Parameterization of *ab initio* potentials and QMD calculation

The *ab initio* total energy calculations of H_2/Rh(111) in order to obtain the potential energy surface have been carried out using *density functional theory* (DFT) within the *generalized gradient approximation* (GGA), using a plane wave basis and ultra-soft pseudopotentials by Sung Sakong [83]. In total, seven different pathways have been studied by the *ab initio* calculations. Among the seven geometries, five geometries correspond to the molecule parallel to the surface, which are shown in Fig. 5.2. The selection of these pathways includes different molecular orientations and locations of the center of mass in the unit cell. The pathways in which the hydrogen molecule remains essentially parallel to the surface with the atoms oriented towards high-symmetry sites are the energetically favorable ones, while the PES's are dominated by repulsive walls for small values of Z for the molecules rotating out of a plane parallel to the surface. The 2D cuts from the parameterized potential for six pathways are plotted in Fig. 5.3 in which elbow plots a)-d) correspond to the PES for parallel orientations ($\theta = 90°$) while elbow plots e) and d) show two typical PES's for a upright orientation ($\theta = 0°$). Energies and geometries of the transition states for the molecule parallel to the surface as obtained by *ab initio* calculation are listed in table 5.1. The fcc-top-hcp orientation (pathway (A)) shows the most favorable energy pathway. As we can see in Fig. 5.3, all of the barriers lie at the beginning of the reaction zone, a so-called early barrier. The pathways (B) and (D) are located at the same lateral position, but at different orientations. Based on the *ab initio* calculation, the difference between transition state of the pathways (B) and (D) is 0.003 eV. Because of this small difference one can assume that the potential energy surface is azimuthally flat. According to this fact, the PES is parameterized in a five-dimensional (5D) model in which the azimuthal degree of freedom is not taken into account. The five degrees of freedom are the reaction path coordinate s and perpendicular to the reaction path ρ, the coordinate corresponding to the center of mass distance from the surface Z and internuclear distance r respectively, two translational degrees of freedom X and Y and the polar rotation θ. The unit vectors associated with the lateral coordinates X and Y are nonorthogonal. The analytical form of the PES adapted to the symmetry of the surface is given by

$$\begin{aligned}
V^{corr} &= V_1^{(c)}(s) + V_2^{(c)}(s)\big[\cos GX + \cos GY + cos(GX + GY)\big] \\
&+ V_3^{(c)}\big[\cos 2GX + \cos 2GY + cos(2GX + 2GY)\big] \\
V^{rot} &= V_1^{(r)}(s)\big[\cos GX + \cos GY + cos(GX + GY)\big]\cos^2\theta \\
&+ V_2^{(r)}(s)\big[\cos(2GX + GY) + \cos(2GY + GX) + \cos(GX - GY)\big]\sin^2\theta \\
V^{vib} &= \frac{\mu}{2}\omega^2(s)\rho^2.
\end{aligned}$$

In Fig. 5.3 the elbow plots of different pathways are shown. In the absence of any azimuthal dependence in the PES pathways (B) and (D) become equivalent; therefore, from the seven high-symmetry sites of *ab initio* configurations, six pathways have been used in the parameterization. In this interpolation we have also focused on the accurate fitting of the transition state energies such that the difference between the *ab initio* results and parameterized potential energies is smaller than 25 meV, however, the deviation is around 50 meV on the average.

The use of nonorthogonal coordinates requires special attention. The Hamiltonian is modified using nonorthogonal coordinates

$$\begin{aligned}
H_{5D} &= -\frac{\hbar^2}{2\mu}\left(\eta^{-1}\frac{\partial}{\partial s}\eta^{-1}\frac{\partial}{\partial s} + \eta^{-1}\frac{\partial}{\partial\rho}\eta\frac{\partial}{\partial\rho} + \frac{\mathbf{L}^2}{r_e^2}\right) \\
&-\frac{\hbar^2}{2M\sin^2\gamma}\left(\frac{\partial^2}{\partial X^2} - 2\cos\gamma\frac{\partial}{\partial X}\frac{\partial}{\partial Y} + \frac{\partial^2}{\partial Y^2}\right) + V_{5D}(X, Y, s, \rho, \theta), \quad (5.1)
\end{aligned}$$

Table 5.1: Energies and geometries of transition state for the molecules parallel to the surface based on the *ab initio* calculation.

Pathway	Z(Å)	r(Å)	E_b (eV)
(A)	-	-	no barrier
(B)	2.0	0.8	0.138
(C)	2.25	0.74	0.027
(D)	2.0	0.74	0.141
(E)	1.95	0.8	0.200

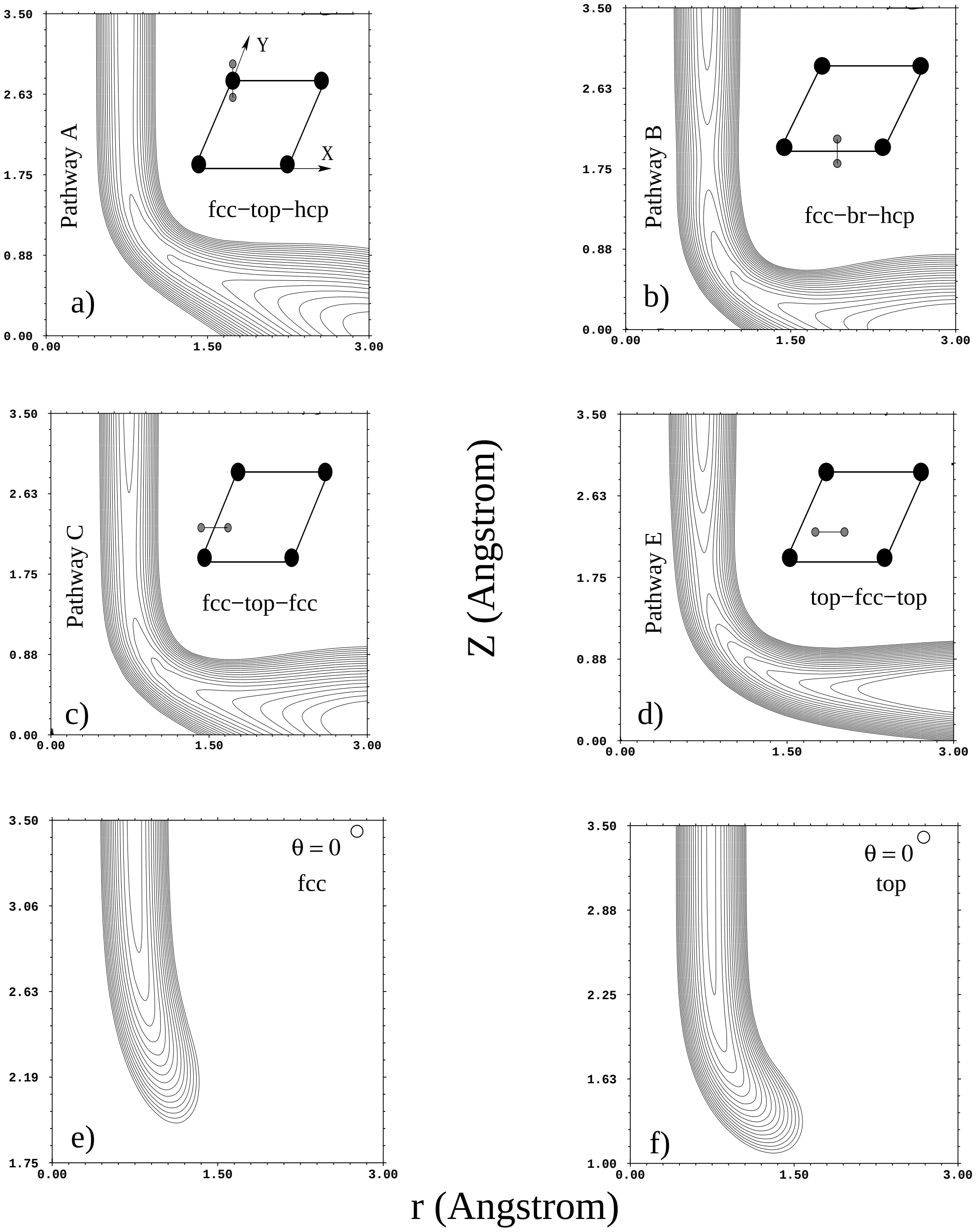

Figure 5.3: 2D-section through the PES for the dissociative adsorption of H_2 lying parallel (a), b), c) and d) configurations) and perpendicular (e) and f) configurations) to the surface over Rh(111) in various configurations. The position of hydrogen molecules is illustrated in the inset. Contour lines are drawn at intervals of 0.2 eV.

where as usual the masses M and μ are the total and reduced mass of H_2 and γ is the angle between the X and Y axes so that for fcc(111) $\gamma = 60°$. The 5D interaction potential is given by a linear combination of the appropriate potentials in Eq. 5.1. In fact, the Hamiltonian describes the motion of a hydrogen molecule in all six degrees of freedom on the azimuthally flat surface. The azimuthal motion of molecule has been considered through the use of the spherical harmonics as the rotational basis functions, where the basis wave function used in the time-independent Schrödinger equation is defined as Eq. 2.32. As mentioned in the second chapter, the computational effort is reduced if the symmetry properties of the surface are taken into account. In the case that the molecule is incident along a symmetry direction of the surface a much more efficient method is obtained if the wave function is expanded in symmetry adapted diffraction eigenfunctions. Here, we limit ourselves to a calculation of the case of normal incidence on the surface which has $C_{6\nu}$ point group symmetry, with the molecule-surface potential being independent of the azimuthal angle ϕ. In the case of normal incidence, we need to include only parallel translational eigenfunctions which are totally symmetric under $C_{6\nu}$ symmetry. The symmetry adapted eigenfunctions are given by

$$\begin{aligned} H_{mn} &= 12^{-1/2}\Big(H_{mn} + H_{nm} + H_{(-m)(-n)} + H_{(-n)(-m)} \\ &+ H_{m(m-n)} + H_{(m-n)m} + H_{(-m)(n-m)} + H_{(n-m)(-m)} \\ &+ H_{(-n)(m-n)} + H_{(m-n)(-n)} + H_{n(n-m)} + H_{(n-m)n}\Big), \end{aligned} \tag{5.2}$$

where H_{mn} is defined as Sec. 2.3.1. Now the matrix element of the potential interaction should be calculated using the symmetry adapted eigenfunctions.

The efficient coupled-channel method using the concept of the local reflection matrix (LORE) is also used in solving the time-independent Schrödinger equation to obtain the reaction probabilities in this work. The quantum numbers associated with the basis set are rotational quantum numbers up to $j_{max} = 8$, vibrational quantum number up to $\nu_{max} = 2$, and parallel momentum quantum numbers up to $p_{max} = 8\hbar G$, respectively. The convergence of the results with respect to the basis set has been carefully checked.

5.4 Rotational effects on the azimuthally flat potential

In Fig. 5.4 the sticking probability as a function of the kinetic energy of hydrogen molecules under normal incidence for different rotational conditions is shown. The results collected in Fig. 5.4a correspond to the sticking probability for molecules which rotate preferentially in the cartwheel fashion. In addition, we have also included the rotationally averaged result to analyze a general influence of rotational effects. Depending on the parallel or antiparallel coupling of the nuclear spins of the H_2 molecules one distinguishes between ortho-hydrogen and para-hydrogen. Then, normal hydrogen corresponds to a mixture of %75 ortho-hydrogen (parallel spins) with %25 para hydrogen (antiparallel spins) according to the degeneracy of the spin states (triplet and

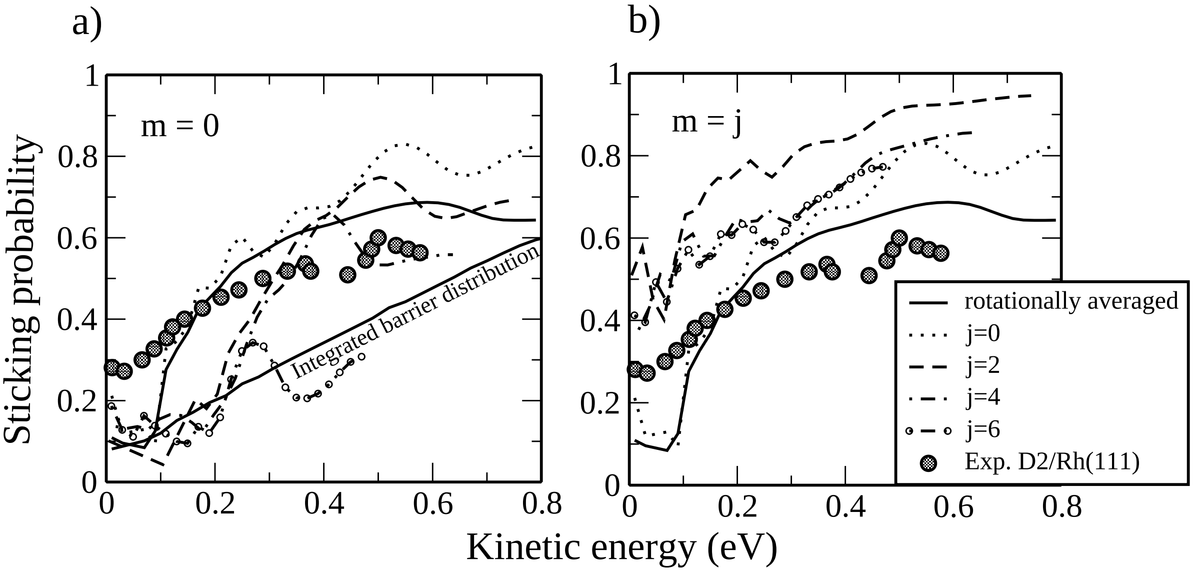

Figure 5.4: Sticking probability versus kinetic energy of molecular beam under normal incidence in different rotational conditions. a) Molecules initially rotate in the cartwheel fashion, b) Molecules initially rotate in the helicopter fashion. The rotationally averaged result is included. The additional bump in the sticking curve [13] is reproduced only in the case of cartwheel rotation.

singlet). In principle, for n-hydrogen the Boltzmann summation should be performed independently for para- and ortho-hydrogen, i.e., for even and odd rotational quantum number; thus we have taken into account the distinction between para- and ortho-hydrogen for the rotationally averaged simulation. Then, in order to calculate rotationally averaged reaction probabilities, as discussed in the previous chapter, the sticking probability for different rotational quantum numbers should be combined according to the Boltzmann distribution. Distinguishing between odd and even rotational quantum number leads to the following form for the sticking probability

$$\begin{aligned} S_{tot}(E_{kin}) &= \frac{3}{4}\frac{\sum_{j_{odd}m} S(E_{kin}, j_{odd}, m)\exp(-E_{rot}(j_{odd}, m)/K_B T_{rot})}{\sum_{j_{odd},m}\exp(-E_{rot}(j_{odd}, m)/K_B T_{rot})} \\ &+ \frac{1}{4}\frac{\sum_{j_{even}m} S(E_{kin}, j_{even}, m)\exp(-E_{rot}(j_{even}, m)/K_B T_{rot})}{\sum_{j_{even},m}\exp(-E_{rot}(j_{even}, m)/K_B T_{rot})}, \end{aligned} \quad (5.3)$$

where as before T_{rot} is defined by $T_{rot} = 0.8 \cdot T_N$. The result of this is also plotted in Fig. 5.4.

The integrated barrier distribution P_b(E) is the fraction of the configuration space for which the barrier towards dissociation is less than E, which corresponds to the sticking probability in the classical sudden approximation or the so-called hole-model [84]. P_b(E) is defined as

$$P_b(E) = \frac{1}{2\pi A}\int \Theta(E - E_b(\theta, \phi, X, Y))\cos\theta d\theta d\phi dX dY, \quad (5.4)$$

where X, Y, θ and ϕ are the lateral and orientational coordinates of the molecule and A is the area of the surface unit cell. The function Θ is the Heavyside step function. E_b is the minimum energy barrier along a cut through the six-dimensional space (see Fig 5.3), where in our parameterized potential E_b is independent of the azimuthal coordinate. The integrated barrier distribution is also included in Fig. 5.4a. Let us first focus on the non-rotating molecules in the dissociative adsorption. The quantum sticking probability for a molecule under normal incidence in the rotational and vibrational ground-state is larger than the sticking probability based on the hole-model. In contrast to the H_2/palladium interaction, the steering of the molecules into favorable pathways at low energies is small, due to the fact that there are only a few non-activated pathways towards dissociative adsorption. The small integrated barrier distribution is clearly illustrated at low energies. At higher energies, the molecules can be steered into the favorable orientation, giving a higher dissociation probability than one would expect simply from the fraction of dissociation barriers (considering all possible sites and orientations). Interestingly, the sticking probability starts to decrease at the kinetic energy around 500 meV and then increases again at 650 meV, although no additional adsorption channel opens up. Therefore, the steering effect is operative at kinetic energies up to 500 meV for non-rotating molecules, but at about 500 meV steering becomes suppressed. The presence of the bump in the sticking probability is not restricted to the non-rotating molecule, it is reproduced for the molecules which rotate preferentially in the cartwheel fashion.

As usual for the cartwheel rotation, rotations of the molecule reduce the sticking probability very efficiently, i.e. rotational hindering is dominant. Rotational averaging for n-hydrogen demonstrates a suppression of the sticking probability compared to the non-rotating molecules. The sticking curve from the experimental result which is illustrated by black circles in Fig 5.4, is in semi-quantitative agreement with the theoretical calculation. According to the experimental results there is a detectable isotope effect between the desorption of hydrogen and deuterium molecules in the low energy regime due to the different rotational states, but this effect becomes very small at higher energies. Based on this fact, we can compare the theoretical calculation for H_2 with the D_2/Rh(111) experimental results, especially at high energies. In Fig. 5.4b the sticking probability is plotted for the molecules which rotate with their axis perpendicular to the surface ($m = j$). The non-monotonous behavior of the j-dependence of the sticking probability is operative for helicoptering molecules so that for $j = 2$ the effect of rotation enhances dissociation while for $j > 2$ the sticking probability decreases with the increasing of the rotational quantum number. Two opposite effects compete, i.e. rotational hindering and the favorable parallel orientation of the molecule. Apparently , adiabatic bond length effects do not play any role, because of the early barrier. As a consequence we do not observe any rotational enhancement for larger j as in the case of the H_2/Pd systems. Furthermore, since the surface is flat, we have in addition to $\Delta j = \pm 2$ the selection rule $\Delta m = 0$. This means that for helicopter molecules with $m = j$ only rotational transitions with $\Delta j = +2$ are possible, i.e. the rotational energy can not be converted in translational energy. It should be noted that we have fitted our calculation by the Gaussian function with initial velocity spread $\Delta v_i / v_i = 0.05$ to obtain a rather smooth sticking curve for the clear distinction between different curves.

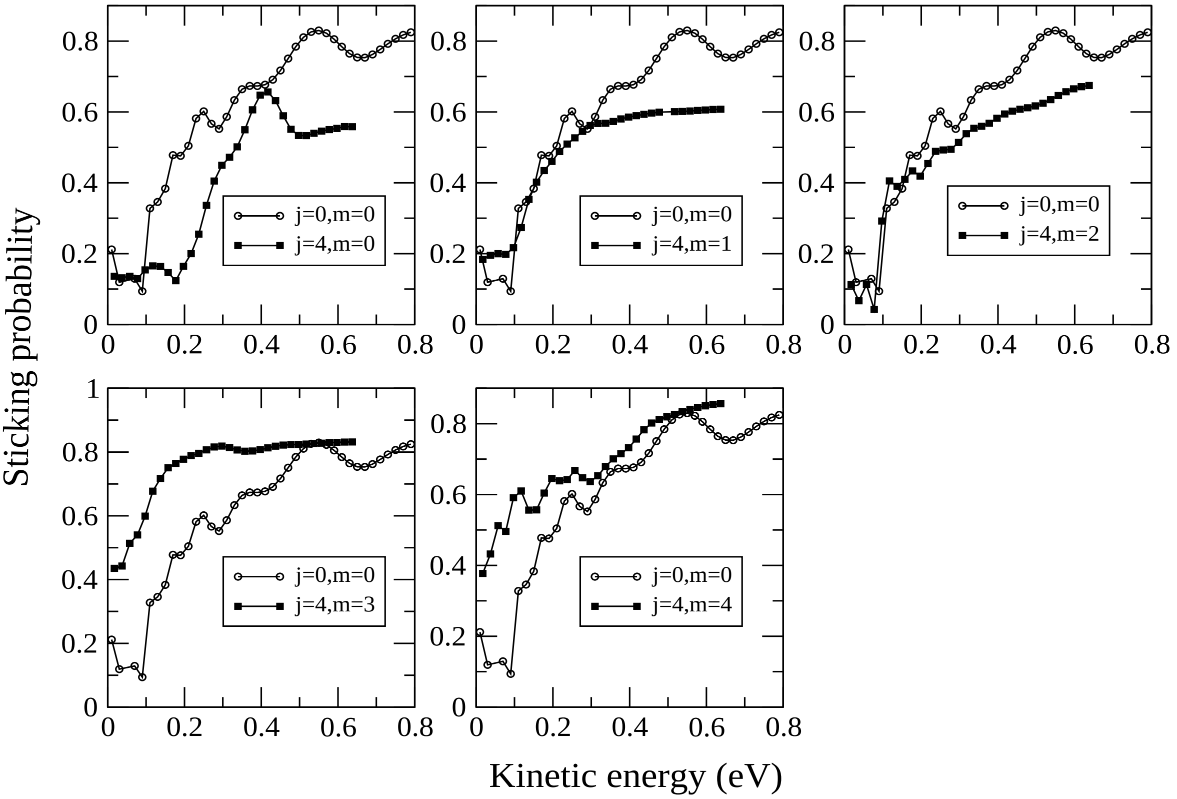

Figure 5.5: Sticking probability versus kinetic energy for the molecules rotating in the j=4 state for various azimuthal quantum numbers. The results for non-rotating molecules are included to follow the rotational effects.

In order to clarify the role of azimuthal quantum number in the dissociative adsorption we have plotted the sticking probability for $j = 4$ in various azimuthal quantum numbers in Fig 5.5. The rotation of the molecule with $m \leq 2$ hinders the dissociation while for $m > 2$ the rotation assists the dissociation. In contrast to H_2/Pd(110) a relatively monotonous enhancement of the sticking probability is found in this case.

Since in experiments, the influence of the molecular rotation is usually determined in desorption we have to analyzed the rotational temperature and rotational alignment, respectively. In contrast to the strongly corrugated Pd(110) surface which shows rotational heating in desorption, well-known rotational cooling is found for H_2 desorption from Rh(111). This result is indicated in Fig 5.6 in which the rotational temperature lies below the thermal equilibrium, i.e. there is a suppression of the sticking probability for rapidly rotating molecule.

The rotational alignment parameters, which are shown in Fig. 5.7, are positive reflecting the fact that the parallel orientation of the molecule (helicoptering molecule) is favorable for dissociation. Due to the non-monotonous behavior of the sticking probabilities for the molecules in the helicopter fashion, we have also found a non-monotonous behavior for the rotational alignment as a function of rotational quantum number. The maximum value of alignment appears at $j = 3$ and decreases then

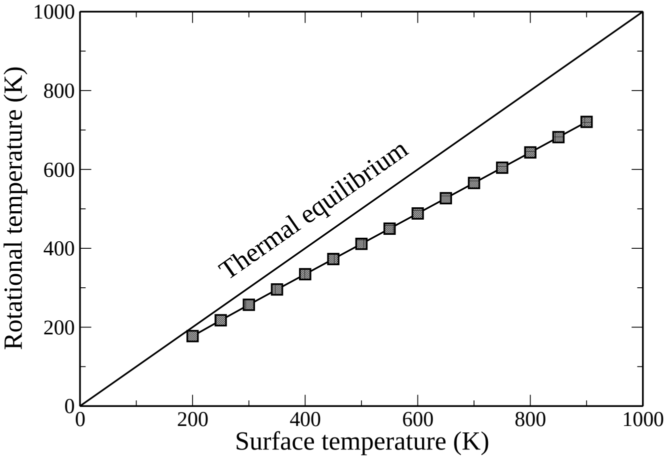

Figure 5.6: Calculated rotational temperature as a function of surface temperature in desorption process. Thermal equilibrium is illustrated by solid line.

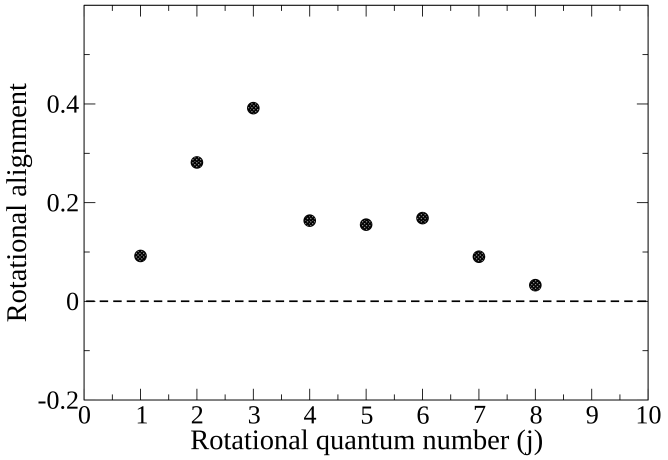

Figure 5.7: Calculated rotational alignment in desorption as a function of the rotational quantum number for a surface temperature of $T = 700$ K.

again. Unfortunately there is no experimental result avaliable for both the rotational temperature as well as the rotational alignment to check our calculational results.

Chapter 6

Conclusions

The multi-dimensional quantum dynamics of light molecules interacting with metals has been studied using a coupled-channel method within the concept of the local reflection matrix (LORE) and the inverse transmission matrix (INTRA). The potential energy surfaces (PES) are parameterized based on the symmetry-adapted functions using *ab initio* total energy calculations within the concept of DFT calculations and generalized gradient approximation.

We have first investigated the rotational dynamics in the non-activated adsorption system H_2/Pd(100). The used potential energy surface is based on *ab initio* calculations, but it has been simplified and adjusted in order to systematically study the influence of the topology of the potential energy surface on adsorption and desorption properties. The non-monotonous behavior of the sticking probability and the rotational alignment in desorption observed in experiment are well-reproduced by our calculations. A fixed molecular bond length during dissociation shows a monotonous increasing for the rotational alignment and a monotonous decreasing for the sticking probability in the cartwheel fashion. This indicates the dependence of the sticking probability on both parameters; bond length and rotational motion. Both effects compete to specify the behavior of the rotational state upon the dissociation. For low rotational quantum numbers rotational hindering suppresses adsorption and desorption probabilities. For higher rotational quantum numbers the change in bond length along the reaction path leads to a decrease in the adiabatic rotational quantum energy which causes an effective energy transfer from rotation to translation. This effect increases the reaction probabilities and decreases the difference between the reaction probabilities of helicopter and cartwheel molecules leading to a smaller rotational alignment.

In the second part of this work, the dissociative adsorption and associative desorption of H_2 on Pd(110) have been studied. Our results are in good agreement with the available experimental data. At low kinetic energies, the dissociative adsorption dynamics is dominated by the steering effects due to the presence of non-activated and activated paths towards. The open (110) surface is characterized by troughs running along the $[1\bar{1}0]$ direction. The strong corrugation and anisotropy of the potential energy surface leads to pronounced orientational effects in the adsorption and desorption dynamics. We found a strong enhancement of the sticking probability for molecules rotating with azimuthal quantum numbers $m > 0$. This enhancement causes an unusual rotational heating in desorption and a rather small rotational alignment. Due to the strong corrugation, we found a significant deviation from normal-energy scaling in the adsorption at non-normal incidence. For an angle of incidence along the close-packed rows of the Pd(110) surface, we find an initial increase of the sticking probability as a function of the angle of incidence which is indicative of a strong corrugation effect. For an azimuthal incidence perpendicular to the troughs of the Pd(110) surface, there is no significant maximum in the sticking probability for non-normal angles of incidence. Based on the surface geometry, along and perpendicular to the troughs running in $[1\bar{1}0]$ direction correspond to the energetic and geometric corrugation, respectively. In spite of the fact that in the case of geometric corrugation the sticking probability is increased by additional parallel momentum, we have found the larger sticking probability for the molecule incident along the $[1\bar{1}0]$ direction. This behavior has been attributed to the fact, that there is no real distinction between energetic and geometric corrugation for a system with both activated and non-activated pathways. We have also followed the scattering process of H_2 from the surface. The strong corrugation and anisotropy of the H_2/Pd(110) PES leads to high intensities in the off-specular as well as rotationally inelastic diffraction peaks. Based on our calculations some off-specular diffraction peaks are larger than the specular peak at low incident angle and also the intensity of some rotationally inelastic diffraction peaks is higher than the rotationally elastic ones. According to the principle of detailed balance, in scattering the cartwheel rotations should be preferentially excited, since in desorption the helicopter rotations are occupied.

Finally, we have investigated the dissociative adsorption of H_2 on Rh(111) in the last part of our work. Interestingly, the experimental measurement shows a step in the sticking probability as a function of beam energy at around 450 meV. This has been attributed to the opening up of additional dissociation channel. Our theoretical calculation is in semi-quantitative agreement with the experiment. The bump is reproduced for $m = 0$ in our theoretical calculations without the opening up of an additional dissociation channel. The quantum sticking probability is much larger than the classical sudden sticking probability based on the hole-model. Due to the low number of non-activated pathways towards dissociative adsorption, the steering effect is less operative at low energies. At higher energies the steering effect is operative up to 500 meV and for larger values it becomes suppressed. In contrast to the open structure of Pd(110), the usual rotational cooling is found in desorption, and the rotational alignment is larger compared to the strongly corrugated Pd(110) surface.

Bibliography

[1] J.E. Lennard-Jones. *Trans. Faraday Soc.*, 28:333, 1932.

[2] J.K. Nørskov and N.D. Lang. Effective-medium theory of chemical binding: Application to chemisorption. *Phys. Rev. B*, 21:2131, 1980.

[3] U. Nielsen, D. Halstead, S. Holloway, and J. K. Nørskov. The dissociative adsortion of hydrogen: two-, three-, and four-dimensional quantum simulations. *J. Chem. Phys.*, 93:2879, 1990.

[4] C. Engdahl and U. Nielsen. Hydrogen dissociation on copper: Importance of dimensionality in calculations of the sticking coefficient. *J. Chem. Phys.*, 98:4223, 1993.

[5] A. Grüneich, A. J. Cruz, and B. Jackson. The dynamics of H_2 dissociation on Cu and Ni surfaces. mixed quantum-classical studies with all degrees of freedom. *J. Chem. Phys.*, 98:5800, 1993.

[6] Axel Groß, Steffen Wilke, and Matthias Scheffler. Six-dimensional quantum dynamics of adsorption and desorption of H_2 at Pd(100): steering and steric effects. *Phys. Rev. Lett.*, 75:2718, 1995.

[7] Axel Groß and Matthias Scherffler. Groß and scheffler reply. *Phys. Rev. Lett.*, 77: 405, 1996.

[8] Axel Groß, Steffen Wilke, and Matthias Scheffler. Six-dimensional quantum dynamics of adsorption and desorption of H_2 at Pd(100): no need for a molecular precursor adsorption state. *Surf. Sci.*, 357/358:614, 1996.

[9] Axel Groß and Matthias Scheffler. Ab initio quantum and molecular dynamics of the dissociative adsorption of hydrogen on Pd(100). *Phys. Rev. B*, 57:2493, 1998.

[10] Axel Groß and Matthias Scheffler. Influence of molecular vibrations on dissociative adsorption. *Chem. Phys. Lett.*, 256:417, 1996.

[11] Axel Groß and Matthias Scheffler. Steering and ro-vibrational effects in the dissociative adsorption and associative desorption of H_2/Pd(100). *Prog. Surf. Sci.*, 53:187, 1996.

[12] A. Groß and M. Scheffler. Role of zero-point effects in catalytic reactions involving hydrogen. *J. Vac. Sci. Technol. A*, 15:1624, 1997.

[13] M. Beutl, J. Lensnik, and K. D. Rendulic. Adsorption dynamics for CO, CO-clusters and H_2 (D_2) on rhodium (111). *Surf. Sci.*, 429:71, 1999.

[14] P. Hohenberg and W. Kohn. Inhomogeneous electron gas. *Phys. Rev.*, 136:B864, 1964.

[15] S. Sato. *J. Chem. Phys.*, 23:592, 1972.

[16] H. F. Busnengo, W. Dong, and A. Salin. Six-dimensional classical dynamics of H_2 dissociative adsorption on Pd(111). *Chem. Phys. Lett.*, 320:328, 2000.

[17] C. Crespos, M. A. Collins, E. Pijper, and G.-J. Kroes. Multi-dimensional potential energy surface determination by modified shepard interpolation for a molecule-surface reaction: H_2 + Pd(111). *Chem. Phys. Lett.*, 376:566, 2003.

[18] T. Takata, T. Taketsugu, and K. Hirao. Ab initio potential energy surface by modified shepard interpolation: Application to the $ch_3 + h_2 \rightarrow ch_4 + h$ reaction.

[19] W. Brenig and M. F. Hilf. cncn. *J. Phys. Condens. Mat.*, 13:R61, 2001.

[20] W. Brenig, T. Brunner, A. Groß, and R. Russ. Numerically stable solution of coupled channel equations: The local reflection matrix. *Z. Phys. B*, 93:91, 1993.

[21] W. Brenig and R. Russ. Numerically stable solution of coupled channel equations: The local transmission matrix. *Surf. Sci.*, 315:195, 1994.

[22] W. Brenig, , A. Groß, and R. Russ. Numerically stable solution of coupled channel equations: The wave-function. *Z. Phys. B*, 97:311, 1995.

[23] Axel Groß. Reactions at surfaces studied by ab initio dynamics calculations. *Surf. Sci. Rep.*, 32:291, 1998.

[24] K. D. Rendulic, G. Anger, and A. Winkler. Wide range nozzle beam adsorption data for the systems H_2/nickel and H_2/Pd(100). *Surf. Sci.*, 208:404, 1989.

[25] L. Schröter, H. Zacharias, and R. David. *Phys. Rev. Lett.*, 62:571, 1989.

[26] D. Wetzig, M. Rutkowski, H. Zacharias, and A. Groß. Vibrational and rotational population distribution of D_2 associatively desorbing from Pd(100). *Phys. Rev. B*, 63:205412, 2001.

[27] S. Wilke and M. Scheffler. Potential-energy surface for H_2 dissociation over Pd(100). *Phys. Rev. B*, 53:4926, 1996.

[28] Geert-Jan Kroes. Six-dimensional quantum dynamics of dissociative chemisorption of H_2 on metal surfaces. *Prog. Surf. Sci.*, 60:1, 1999.

[29] E. Watts and G. O. Sitz. Surface temperature dependence of rotational excitation of H_2 scattered from Pd(111). *J. Chem. Phys.*, 111:9791, 1999.

[30] H. F. Busnengo, W. Dong, P. Sautet, and A. Salin. Surface temperature dependence of rotational excitation of H_2 scattered from Pd(111). *Phys. Rev. Lett.*, 87: 127601, 2001.

[31] Z. S. Wang, G. R. Darling, and S. Holloway. Surface temperature dependence of the inelastic scattering of hydrogen molecules from metal surfaces. *Phys. Rev. Lett.*, 87:226102, 2001.

[32] B. Gergen, H. Nienhaus, W. H. Weinberg, and E. W. McFarland. Chemically induced electronic excitations at metal surfaces. *Science*, 294:2521, 2001.

[33] J. T. Kindt, J. C. Tully, M. Head-Gordon, and M. A. Gomez. Electron-hole pair contribution to scattering, sticking and surface diffusion: CO on Cu(100). *J. Chem. Phys.*, 109:3629, 1998.

[34] K. D. Rendulic and A. Winkler. Adsorption and desorption dynamics as seen through molecular beam techniques. *Surf. Sci.*, 299/300:261, 1994.

[35] M. Gostein and G. O. Sitz. Rotational state-resolved sticking coefficients for H_2 on Pd(111): testing dynamical steering in dissociative adsorption. *J. Chem. Phys.*, 106:7378, 1997.

[36] D. Wetzig, M. Rutkowski, R. Etterich, W. David, and H. Zacharias. Rotational alignment in associative desorption of H_2 from Pd(100). *Surf. Sci.*, 402:232, 1998.

[37] D. Wetzig, R. Dopheide, M. Rutkowski, R. David, and H. Zacharias. Rotational alignment in associative desorption of D_2 (v=0 and 1) from Pd(100). *Phys. Rev. Lett.*, 76:463, 1996.

[38] Andreas Eichler, Jürgen Hafner, Axel Groß, and Matthias Scheffler. Rotational effects in the dissociation of H_2 on metal surfaces studied by ab initio quantum dynamics calculations. *Chem. Phys. Lett.*, 311:1, 1999.

[39] A. Groß. *Theoretical surface science – A microscopic perspective.* Springer, Berlin, 2002.

[40] M. Beutl, M. Riedler, and K. D. Rendulic. Strong rotational effects in the adsorption dynamics of H_2/Pd(111): evidence for dynamical steering. *Chem. Phys. Lett.*, 247:249, 1995.

[41] Axel Groß and Matthias Scheffler. Scattering of hydrogen molecules from a reactive surface: strong off-specular and rotationally inelastic diffraction. *Chem. Phys. Lett.*, 263:567, 1996.

[42] A. D. Kinnersley, G. R. Darling, S. Holloway, and B. Hammer. A comparison of quantum and classical dynamics of H_2 dissociation on Cu(111). *Surf. Sci.*, 364: 219, 1996.

[43] Axel Groß. Quantum effects in the dissociative adsorption of hydrogen. *J. Chem. Phys.*, 110:8696, 1999.

[44] George R. Darling and S. Holloway. Rotational motion and the dissociation of H_2 on Cu(111). *J. Chem. Phys.*, 101:3268, 1994.

[45] H. A. Michelsen, C. T. Rettner, D. J. Auerbach, and R. N. Zare. Effect of rotation on the translational and vibrational-energy dependence of the dissociative adsorption of D_2 on Cu(111). *J. Chem. Phys.*, 98:8294, 1993.

[46] H. Hou, S. J. Gulding, C. T. Rettner, A. M. Wodtke, and D. J. Auerbach. The stereodynamics of a gas-surface reaction. *Science*, 277:80, 1997.

[47] M. Rutkowski and H. Zacharias. Simulation of the surface reaction of D_2 on a sulfur covered Pd(100) surface. *Phys. Chem. Chem. Phys.*, 3:3645, 2001.

[48] H. J. Kreuzer and Z. W. Gortel. *Physisorption Kinetics*, volume 1 of *Springer Series in Surface Sciences.* Springer, Berlin, 1986.

[49] W. Brenig. *Nonequilibrium Thermodynamics.* Springer, Berlin, 1990.

[50] M. Kay, G. R. Darling, S. Holloway, J. A. White, and D. M. Bird. Steering effects

in non-activated adsorption. *Chem. Phys. Lett.*, 245:311, 1995.

[51] G. R. Darling and S. Holloway. The dissociation of diatomic molecules at surfaces. *Rep. Prog. Phys.*, 58:1595, 1995.

[52] Axel Groß. The role of lateral surface corrugation for the quantum dynamics of dissociative adsorption and associative desorption. *J. Chem. Phys.*, 102:5045, 1995.

[53] H. A. Michelsen and D. J. Auerbach. A critical-examination of data on the dissociative adsorption and associative desorption of hydrogen at copper surfaces. *J. Chem. Phys.*, 94:7502, 1991.

[54] C. T. Rettner, D. J. Auerbach, and H. A. Michelsen. Role of vibrational and translational energy in the activated dissociative adsorption of d_2 on cu(111). *Phys. Rev. Lett.*, 68:1164, 1992.

[55] A. Hodgson, J. Moryl, P. Traversaro, and H. Zhao. Energy transfer and vibrational effects in the dissociation and scattering of D_2 from Cu(111). *Nature*, 356:501, 1992.

[56] M. Beutl, M. Riedler, and K. D. Rendulic. Adsorption dynamics for para and *n*-hydrogen on Pt(110): rotational state resolved sticking coefficients. *Chem. Phys. Lett.*, 256:33, 1996.

[57] T. Mitsui, M. K. Rose, E. Fomin, D. F. Ogletree, and M. Salmeron. Dissociative hydrogen adsorption on palladium requires aggregates of three or more vacancies. *Nature*, 422:705, 2003.

[58] A. Groß, B. Hammer, M. Scheffler, and W. Brenig. High-dimensional quantum dynamics of adsorption and desorption of H_2 at Cu(111). *Phys. Rev. Lett.*, 73: 3121, 1994.

[59] Axel Groß and Matthias Scheffler. Dynamics of hydrogen dissociation at the sulfur-covered Pd(100) surface. *Phys. Rev. B*, 61:8425, 2000.

[60] A. Dianat and A. Groß. Rotational quantum dynamics in a non-activated adsorption system. *Phys. Chem. Chem. Phys.*, 4:4126, 2002.

[61] G.-J. Kroes, E. J. Baerends, and R. C. Mowrey. Six-dimensional quantum dynamics of dissociative chemisorption of ($v = 0$,$j = 0$) H_2 on Cu(100). *Phys. Rev. Lett.*, 78:3583, 1997.

[62] G.-J. Kroes, A. Groß, E. J. Baerends, M. Scheffler, and D. A. McCormack. Quantum theory of dissociative chemisorption on metal surfaces. *Acc. Chem. Res.*, 35: 193, 2002.

[63] Andreas Eichler, Jürgen Hafner, Axel Groß, and Matthias Scheffler. Trends in the chemical reactivity of surfaces studied by ab initio quantum-dynamics calculations. *Phys. Rev. B*, 59:13297, 1999.

[64] W.A. Diño, H. Kasai, and A. Okiji. Orientational effects in dissociative adsorption/associative desorption dynamics of $H_2(D_2)$ on Cu and Pd. *Prog. Surf. Sci.*, 63:63, 2000.

[65] Y. Miura, H. Kasai, and W.A. Diño. Dynamical quantum filtering in the scattering of H_2 on Cu(001). *J. Phys.: Condens. Matter*, 14:L479, 2002.

[66] C. Crespos, H. F. Busnengo, W. Dong, and A. Salin. Analysis of H_2 dissociation dynamics on the Pd(111) surface. *J. Chem. Phys.*, 114:10954, 2001.

[67] H. F. Busnengo, E. Pijper, M. F. Somers, G. J. Kroes, A. Salin, R. A. Olsen, D. Lemoine, and W. Dong. Six-dimensional quantum and classical dynamics study of h_2 $(v = 0, j = 0)$ scattering from Pd(111). *Chem. Phys. Lett.*, 356:515, 2002.

[68] H. F. Di Cesare, M. A. Busnengo, W. Dong, and A. Salin. Role of dynamic trapping in H_2 dissociation and reflection on Pd surfaces. *J. Chem. Phys.*, 118: 11226, 2003.

[69] J. N. Murrell, A. T. Yinnon, and R. B. Gerber. Applications of symmetry in coupled channel atom-surface scattering calculations. *Chem. Phys.*, 33:131, 1978.

[70] G.-J. Kroes, J. G. Snijders, and R. C. Mowrey. Performance of close-coupled wave-packet methods for molecule-corrugated surface scattering. *J. Chem. Phys.*, 103:5121, 1995.

[71] C. Resch, H. F. Berger, K. D. Rendulic, and E. Bertel. Adsorption dynamics for the system hydrogen/palladium and its relation to the surface electronic-structure. *Surf. Sci.*, 316:L1105, 1994.

[72] V. Ledentu, W. Dong, and P. Sautet. Ab initio study of the dissociative adsorption of H_2 on the Pd(110) surface. *Surf. Sci.*, 412:518, 1998.

[73] H. F. Busnengo, A. Salin, and W. Dong. Representation of the 6D potential energy surface for a diatomic molecule near a solid surface. *J. Chem. Phys.*, 112:7641, 2000.

[74] G. Boato, P. Cantini, and L. Mettera. Elastic and rotationally inelastic diffraction of hydrogen molecular beams from the (001) face of LiF at 80° K. *J. Phys. Chem.*, 65:544, 1976.

[75] G. Brusdeylins and J. P. Toennies. Simultaneous excitation of rotations and surface phonons in the scattering of D_2 from a NaF crystal. *Surf. Sci.*, 126:647, 1983.

[76] R. G. Rowe and G. Ehrlich. Rotationally inelastic diffraction of molecular beams: H_2, D_2, HD from (001) MgO. *J. Chem. Phys.*, page 4648, 1975.

[77] K. B. Whaley, C.-F. Yu, C. S. Hogg, J. C. Light, and S.J. Sibener. Investigation of the spatially anisotropic component of the laterally averaged molecular hydrogen/Ag(111) physisorption potential. *J. Chem. Phys.*, 83:4235, 1985.

[78] M. F. Bertino, F. Hofmann, and J. P. Toennies. The effect of dissociative chemisorption on the diffraction of D_2 from Ni(110). *J. Chem. Phys.*, 106:4327, 1997.

[79] D. Cvetko, A. Morgante, A. Santaniello, and F. Tommasini. Deuterium scattering from Rh(110) surface. *J. Chem. Phys.*, 104:7778, 1996.

[80] E. Hulpke, editor. *Helium Atom Scattering from Surfaces*, volume 27 of *Springer Series in Surface Sciences*. Springer, Berlin, 1992.

[81] J.E. Lennard-Jones and A.F. Devonshire. *Nature*, 137:1069, 1936.

[82] J. P. Cowin, C. F. Yu, S. J. Sibener, and J. E. Hurst. Bound level resonances in rotationally inelastic HD/Pt(111) surface scattering. *J. Chem. Phys.*, 75:1033,

1981.

[83] A. Dianat, S. Sakung, and A. Groß. Quntum dynamics of H_2 on Rh(111) based on the ab initio calculation. *to be published*.

[84] M. Karikorpi, S. Holloway, N. Henriksen, and J. K. Nørskov. Dynamics of molecule surface interactions. *Surf. Sci.*, 179:L41, 1987.

List of Publications

1. Arezoo Dianat and Axel Groß. Rotational quantum dynamics in a non-activated adsorption system. *Phys. Chem. Chem. Phys.*, 4:4126-4132, 2002.
2. Arezoo Dianat and Axel Groß. High-dimensional quantum dynamical study of the dissociation of H_2 on Pd(110). *J. Chem. Phys.*, 120:5339-5346, 2004.